Inaugural Dissertation zur Erlangung des
Doktorgrades der Naturwissenschaften
der Justus-Liebig-Universität Gießen
(Fachbereich Physik)

Investigation of stored neutron-rich nuclides in the element range of Pt – U with the FRS-ESR facility at 360 – 400 MeV/u

Lixin Chen

August 24, 2008, Gießen

Dedicate to my family ...

Zusammenfassung

Masse und Lebensdauer eines Kernes sind Schlüsselgrößen zum Verständnis der Kernstruktur, der möglichen Reaktionen und der Elemententstehung und Häufigkeit im Universum.

In dieser Arbeit wurden Experimente zur Bestimmung der Masse und Lebensdauer von gespeicherten, exotischen Kernen bei GSI durchgeführt. Die exotischen Kerne wurden mit einem 670 MeV/u ^{238}U Projektilstrahl in einem 4 g/cm^2 Beryllium Target am Eingang des Fragmentseparators FRS erzeugt. Neutronenreiche Kerne im Elementbereich zwischen Thallium und Uranium wurden im Fluge mit dem FRS separiert und in den Experimentierspeicherring ESR injiziert. Durch genaue Messung der Umlaufzeiten der gespeicherten und mit Elektronen gekühlten Kerne konnten sowohl ihre Massen als auch Lebensdauern erstmals gemessen werden.

In diesem Experiment konnten 5 neue Isotope und 6 Isomere im Zuge der Massenmessung entdeckt werden. Die hochpräzise Massenmessung ermöglichte gleichzeitig eine eindeutige Isotopenzuordnung. Solch einen Schritt in das Neuland der noch unbekannten exotischen Kerne konnte bei diesem Experiment zum ersten Mal gemacht werden. Die erstmals beobachteten Kerne waren ^{236}Ac, ^{224}At, ^{222}Po, ^{221}Po und ^{213}Tl. Weiterhin wurden die folgenden Isomere erstmals beobachtet: ^{234m}Ac, ^{234n}Ac, ^{228m}Ac, ^{228m}Fr, ^{214m}Bi, und ^{213m}Bi. Die Massenbestimmung erfolgte mit Hilfe der zeitkorrelierten Schottky Analyse, so dass auch Lebensdauern innerhalb der experimentellen Randbedingungen, den Speicher- und Kühlzeiten sowie den 5 minütigen Messzyklen, bestimmt wurden. Die globale Genauigkeit der Massenmessung war etwa 30 keV (Standardabweichung). Für 30 vorher bekannte Isotope konnte die Masse erstmals experimentell bestimmt werden. Zu dieser Billanz gehört, dass die Genauigkeit der Massenwerte für 16 weitere Nuklide erheblich verbessert wurde.

Die Lebensdauermessung basiert auf der Proportionalität der gespeicherten Ionen zur Fläche unter den Schottky Frequenzpeaks oder der Ausmessung einer 'Teilchenspur' eines einzelnen Ions im zweidimensionalen Frequenzspektrum. Eine Abnahme der gespeicherten Ionen innerhalb eines Messzyklus von 5 Minuten beruht vorwiegend auf dem Kernzerfall, da atomare Wechselwirkungen im Ultrahochvakuum und mit den Elektronen im Kühler mindestens eine Größenordnung geringer sind.

Summary

Nuclear masses and lifetimes are the basic properties to understand nuclear existence and structure resulting from the strong interaction. Both informations are also important for the understanding of nuclear astrophysics and fundamental interaction. Most experimental information was in the past obtained for nuclides close to the valley of stability, i.e., experimental data for exotic nuclei are still rare and important. In the present experiment masses and lifetimes of stored exotic nuclei in Tl – U region were measured with the FRS-ESR facility.

The exotic nuclei were produced by fragmentation of 670 MeV/u ^{238}U projectiles in a 4g/cm^2 Be target placed at the entrance of the fragment separator FRS. The produced exotic nuclei were separated in flight with the FRS and injected into the storage-cooler ring ESR for high precision mass and half-life measurement. The injected hot ions were cooled by electron cooling. The relative velocity spread of the stored ions was reduced down to the level of $5 \cdot 10^{-7}$ for low intensity beams. The cooled beam was stored in ESR for about 5 minutes for each injection cycle and the revolution frequency of the stored ions was precisely measured. The unknown masses were directly determined from the revolution frequency using known masses in the same spectrum for calibration. In addition to the atomic mass, the half-life of stored ions has been determined with the time-resolved Schottky frequency analysis.

The neutron-rich region from Tl to U was investigated in this work. The ultimate sensitivity, down to single particles, and the high resolving power of the time-resolved Schottky mass analysis (SMS) were the basis for the discovery of the five isotopes: ^{236}Ac, ^{224}At, ^{222}Po, ^{221}Po and ^{213}Tl and the six new isomers: ^{234m}Ac, ^{234n}Ac, ^{228m}Ac, ^{228m}Fr, ^{214m}Bi and ^{213m}Bi. The isotope identification was unambiguous going along simultaneously with the first mass determination for the new isotopes and isomers. Experimental masses of 30 known isotopes in this heavy neutron-rich region were measured for the first time. Furthermore, the half-lives of 12 nuclides including ^{235}Ac were determined experimentally for the first time. The total accuracy of the mass measurement in the present experiment was 30 keV mainly determined by the systematical errors.

Our experimental results have been compared to theoretical models. In this comparison microscopic and macroscopic theories have been applied. The new experimental mass data contribute to a better knowledge of the most neutron-rich nuclides in the Pt – U region.

Contents

Chapter 1

Introduction

1.1 Motivation for mass and lifetime measurements

The mass and the lifetime are both basic characteristics of atomic nuclei. The mass values are directly connected to the nuclear binding energy which represents the sum of all the interactions within such a complex many-body system. The mass $M(Z,N)$ of a neutral atom with Z protons and N neutrons is:

$$M(Z,N) = Z \cdot (m_p + m_e) + N \cdot m_n - BE_{electron} - BE_{nuclear}, \tag{1.1}$$

where m_p, m_n and m_e are the rest mass of the proton, the neutron and the electron, respectively. $BE_{electron}$ is the total electron binding energy which can be accurately calculated with quantum electrodynamics[1] and can be approximated by[2]:

$$BE_{electron}(Z) = 14.4381\,Z^{2.39} + 1.55468 \cdot 10^{-6}\,Z^{5.35} \quad (eV). \tag{1.2}$$

$BE_{nuclear}$ is the nuclear binding energy. The pioneer work in the field of mass measurement has played an important role for the development of the nuclear shell model[3]. At the magic numbers of protons and neutrons the nuclides are most strongly bound and the shell closure can be clearly seen from the mass surface.

The atomic mass and lifetime values play also a key role in other fields[4] like nuclear astrophysics. The required mass accuracy depends on the applications:

Nuclear physics Nuclear shell effects can be observed by mass mapping with a typical accuracy around 10^{-6}. Subtle effects like deformations, pairing and subshell effects can be detected with a higher accuracy ($10^{-7} \sim 10^{-8}$). The proton and neutron drip-lines are determined by the single and double nucleon separation energies. The lifetime of nuclides reflects the stability of the system especially at and near the shell closures.

Astrophysics The nucleosynthesis in stars is governed by the Q values in nuclear reactions and decays. The Q value is determined by the binding energy of the nuclei involved. Presently, the model calculations of the r-process and the rp-process rely on the predictions of masses and lifetimes which have a large uncertainty for nuclei far from stability. Accurate mass and lifetime measurements of nuclei at the nucleosynthesis paths have a great impact for the basic questions in nuclear astrophysics.

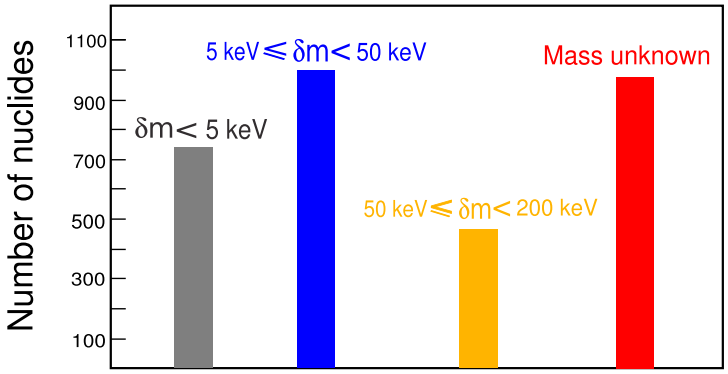

Figure 1.1: Mass uncertainties of known isotopes in AME2003[10].

Fundamental physics and applied physics Theory such as the variation of fundamental constants, the conservation of the vector current (CVC) hypothesis in weak interaction and the unitarity of CKM quark-mixing matrix can be tested by very high accurate mass($\sim 10^{-9}$) and half-life measurements[5].

The astrophysical sites where the r-process can happen are at high density and high temperature stellar matter[6]. In this environment the ions are highly charged. Presently most of the nuclear lifetime values are measured for neutral atoms. Highly-ionized atoms can have a significant change in lifetimes. Nuclear decay channels can be blocked, or new decay modes can be opened up[7]. For example, the bound β decay[8, 9] channels become an important branch for highly-charged ions and also the electron capture rates can be significantly changed due to the change of bound orbital electrons. Therefore, important input data for nuclear astrophysics can be provided by lifetime measurements with highly-charged ions.

1.2 Knowledge of atomic masses

The knowledge of atomic masses steadily grows thanks to the efforts of many experimental and theoretical groups around the world. Due to the progress of the accelerator facilities and experimental techniques, more exotic nuclei with very small production cross sections and short half-lives become available for experimental studies.
Though much progress has been achieved, there are still 951 known nuclei without measured masses in the table of Atomic Mass Evaluation 2003 (AME2003)[10] which in total 3179 nuclei are listed. There are also measured masses for exotic nuclei with large uncertainties in that table. Fig.1.1 shows the statistics of the mass uncertainty according to AME2003 mass table. The chart of nuclides in Fig.1.2 illustrate the status of knowledge of nuclear mass.

The interest on the mass measurements is the motivation for new facilities worldwide.

1.3 The predictive power of mass models

To explain the element abundance in the universe, we have to understand the process of nucleosynthesis in stars. Because of the lack of experimental data, the astrophysical

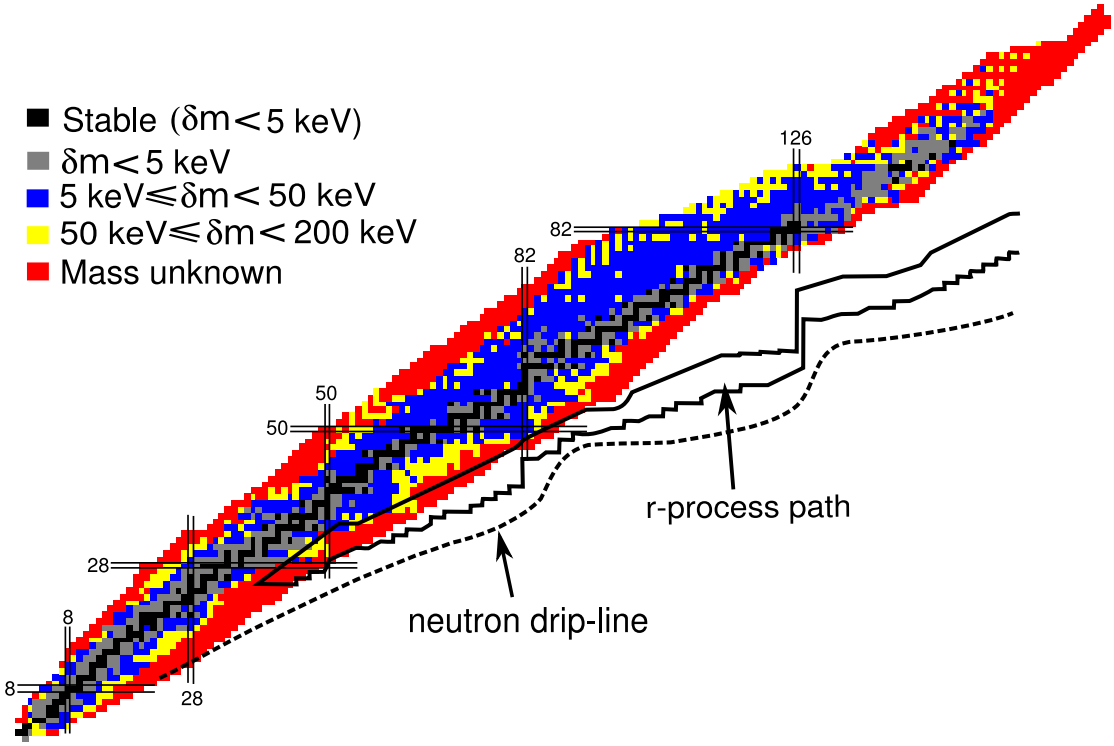

Figure 1.2: The status of atomic mass knowledge from AME2003[10]. The neutron drip-line was predicted by the Finite-Range-Droplet Model (FRDM95)[11].

network calculation of the r-process and rp-process have to use the predicted values from mass models.

Many mass models including microscopic approaches, macroscopic-microscopic approaches and some global/local mass formulas have been developed to predict unknown masses. In general, the mass models agree in the region of known masses but have large deviations in the region of unknown masses. Fig.1.3 shows the mass prediction for different mass models compared with experimental data of uranium isotopes. The deviations of the different mass models can amount up to a few MeV depending on the distance to the area of known masses.

As illustrated in Fig.1.3 present mass models can not provide accurate data for astrophysical network calculations. For example, the r-process isotopes are far from the experimentally known mass region. Therefore, new mass measurements are urgently needed.

1.4 Methods of direct mass measurement for stored ions

Atomic mass spectrometry has a long history and consists of two types experimental methods – indirect and direct measurement. Both made great contributions in the past. Indirect mass measurement rely on the energy conservation in reactions or decays. See reference[24] for a recent review of indirect mass measurements.
In the direct method the unknown masses are determined by measuring the motion in the electromagnetic fields with respect to reference masses. Modern mass spectrometry

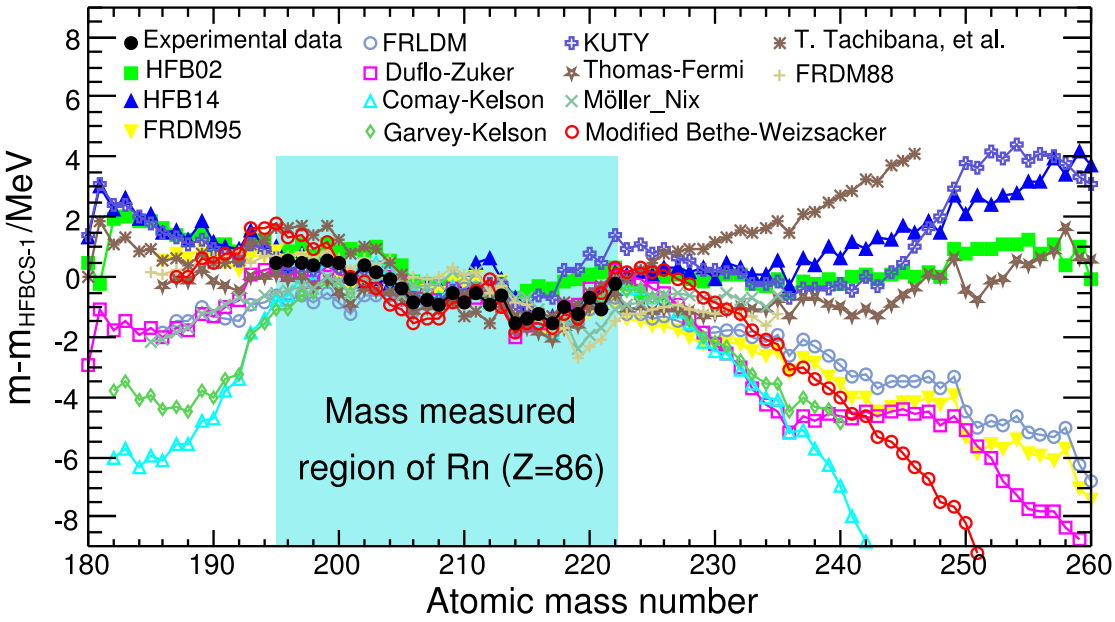

Figure 1.3: Comparison of different mass models and experimental data for Rn isotopes. The experimental data are taken from AME2003[10]. The reference model in this comparison is the HFBCS-1 mass formula. HFBCS-1: Hartree-Fock mass formula with pairing energy treated in the BCS approximation [12]; HFB02: Hartree-Fock-Bogoliubov mass model[13]; HFB14: Further explorations of Skyrme-Hartree-Fock-Bogoliubov mass formulas. VII. Simultaneous fits to masses and fission barriers[14]; FRDM95: Finite-Range-Droplet Model[11]; FRLDM: Finite-Range Liquid-Drop Model[11]; Duflo-Zuker: Microscopic mass formulas[15]; Comay-Kelson: Mass Predictions by Modified Ensemble Averaging[16]; Garvey-Kelson: Mass Predictions from the Garvey-Kelson Mass Relations[17]; KUTY: H. Koura, et al., [18]; Thomas-Fermi: W. D. Myers and W. J. Swiatecki[19]; Möller-Nix: Nuclear Masses from a Unified Macroscopic-Microscopic Model[20]; Modified Bethe-Weizsäcker: A Modified Bethe-Weizsäcker Mass Formula with Deformation and Shell Corrections and Few Free Parameters[21]; T. Tachibana: Empirical Mass Formula with Proton-Neutron Interaction[22]; FRDM88: Nuclear Mass Formula with a Finite-Range Droplet Model and a Folded-Yukawa Single-Particle Potential [23];

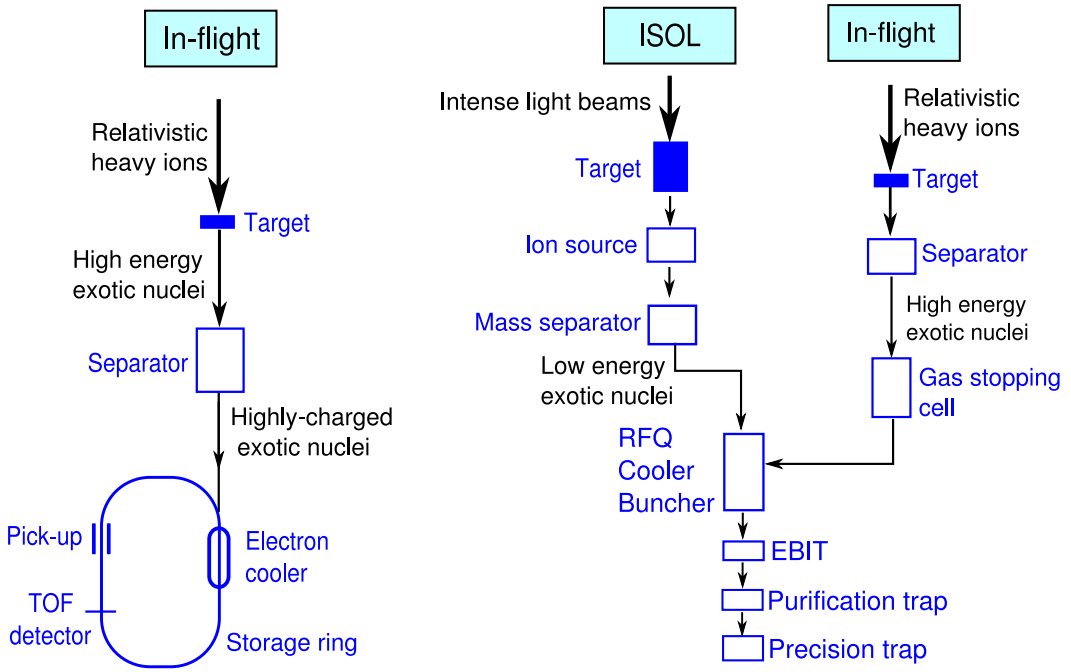

Figure 1.4: Experimental scenario for the production, separation and mass measurement of stored ions. Left: In-flight method coupled to a storage cooler ring. The highly-charged ions are produced by ion penetration through matter at relativistic energies. Mass measurements in the storage ring can be performed with cooled exotic nuclei (Schottky Mass Spectrometry) and hot stored fragments (Isochronous Mass Spectrometry). The SMS can be applied for nuclei with lifetime longer than a few seconds. For very short-lived fragments no cooling can be provided and the ring is operated in the isochronous mode and a TOF detector is used. Right: Both ISOL and in-flight separation methods provide exotic nuclei for ion trap systems. In the case of in-flight method a gas stopping cell is required to slow down the ions. Usually the trap system consists of a preparation trap for purification and a precision trap for the actual mass measurement. The mass precision can be improved by highly charged ions which can be produced by the electron beam ionization system EBIT[27, 28].

is based on the measurement of time-of-flight or cyclotron frequency which can be very precisely measured[25]. At present, much progress has been achieved with measurements in storage rings and Penning traps[26]. Fig.1.4 shows the principle of the storage ring and the ion trap facilities for direct mass measurement.

1.4.1 Mass measurements with Penning traps

Penning traps are a powerful tool for measuring the mass of radioactive ions with very high precision[29, 30]. Penning traps use a strong homogeneous axial magnetic field to confine charged particles radially and an electric quadrupole field to confine them axially. The mass of the trapped ions is determined by the measurement of their cyclotron frequency in the strong magnetic field B_z:

$$\nu_c = \frac{1}{2\pi}\frac{q}{m}\cdot B_z. \tag{1.3}$$

There are two techniques to determine the cyclotron frequency – The time-of-flight ion-cyclotron resonance method and the Fourier transformation ion-cyclotron resonance method[26].

The time-of-flight technique is based on the measurement of the flight time of trapped ions from the trap to an external detector. The stored ion in Penning trap will be excited with a radio frequency (v_{rf}) field traditionally by quadrupolar excitation ($v_{rf} \sim v_c$) or the new technique applying octupolar excitation[31, 32] ($v_{rf} \sim 2v_c$) which leads to a higher resolution. The ion motion will be in a resonance when properly excited ($v_{rf} = v_c \, or \, 2v_c$) and this leads to a minimum time-of-flight. In the measurement, v_{rf} is tuned around v_c and the minimum value of time-of-flight can be determined thus the v_c be determined from v_{rf}.
The Fourier transform ion-cyclotron resonance technique[33] is a non-destructive detection method for trapped ions. This technique is based on the detection of the image current on the Penning trap ring electrodes which is induced by the circulating motion of trapped charged ions. The Fourier transformation of the periodic image current yields a precise determination of the cyclotron frequency of the trapped ions.
The cyclotron frequencies of the reference and unknown masses are both measured under the same experimental conditions thus the unknown mass can be determined directly by the difference of the cyclotron frequencies. By using very well known reference masses and long excitation cycles (possible for long-lived nuclei), the unknown mass can be determined very precisely (up to $\sim 10^{-10}$).

1.4.2 Mass measurements with storage rings

The storage ring mass measurement program in GSI by combining the fragment separator FRS[34] and the experimental storage ring ESR[35] has provided about three hundreds new masses and in addition about three hundred masses with improved accuracy. The charged ions can be stored in the ring for a relatively long time, therefore, precise measurement of the revolution frequency or time-of-flight can be performed. The operation of ESR in two different optical modes yields two different mass measurement methods – Schottky Mass Spectrometry (SMS)[36] and Isochronous Mass Spectrometry (IMS)[37]. The same methods will be applied in the new cooler storage ring installed at the Institute of Modern Physics (IMP) in Lanzhou, China[38].

SMS ESR operates in the conventional storage mode. The stored charged ions in the ESR are cooled by electron cooling and the velocity spread could be reduced down to $\sim 5 \cdot 10^{-7}$ in the case of the number of ions at the level of thousands and below. The circulating frequency of all stored ions will be measured simultaneously. The unknown masses can be deduced from known masses by the difference of their revolution frequencies. *The results presented in this paper are all from one SMS experiment. Details of SMS will be explained in later chapters.*

IMS ESR operates in the isochronous mode thus the circulating frequency of the stored ions is independent of their velocity spread. The revolution time of hot fragments can be measured directly by a time-of-flight detector which is installed inside the ESR. Similar to SMS measurement, the unknown masses are deduced from the time-of-flight spectrum which is calibrated with known masses.

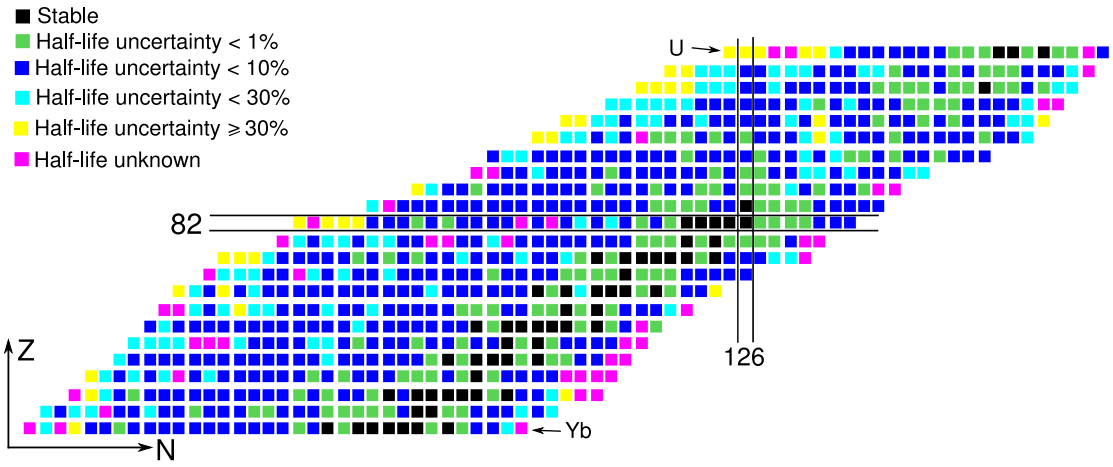

Figure 1.5: Experimental half-lives in the element range of Yb – U. Data are taken from NUBASE2003[39]

This method can access nuclei with much shorter half-lives (down to the sub-millisecond range) but has a presently larger uncertainty compared to the SMS method.

1.5 Knowledge of nuclear lifetimes

The most recent collection of nuclear lifetime data is the NUBASE2003[39] evaluation. In Fig.1.5 the present status of nuclear half-lives are displayed in the element range $70 \leq Z \leq 92$. Besides the isotopes with unknown half-lives in the very exotic region, many isotopes are only measured with a large uncertainty. In the heavy neuron-rich region (Fig.1.5) the knowledge of experimental half-life is limited by the difficulties in production and separation of those neutron-rich nuclei.

The modern storage ring and ion traps are powerful facilities for ion storage, cooling and decay studies. Especially for the short-lived exotic nuclei with small production rates the storage ring and ion traps extend the conventional experimental tools in nuclear spectrometry.

1.6 Methods for lifetime measurement of stored ions

Storage and cooling of exotic nuclei present a unique opportunity to study nuclear decay properties. Decay studies of bare and few-electron ions have opened a new area in nuclear spectroscopy. The highly charged ions can be produced in two ways depending on the subsequent storage scenario. For ion traps, the storage facilities at low energy, the high ionization degree can be achieved with electron-impact ionization in so called Electron Beam Ion Traps (EBIT)[27, 28]. At storage rings the high ionization degree is provided by relativistic heavy ions penetrating though the matter.

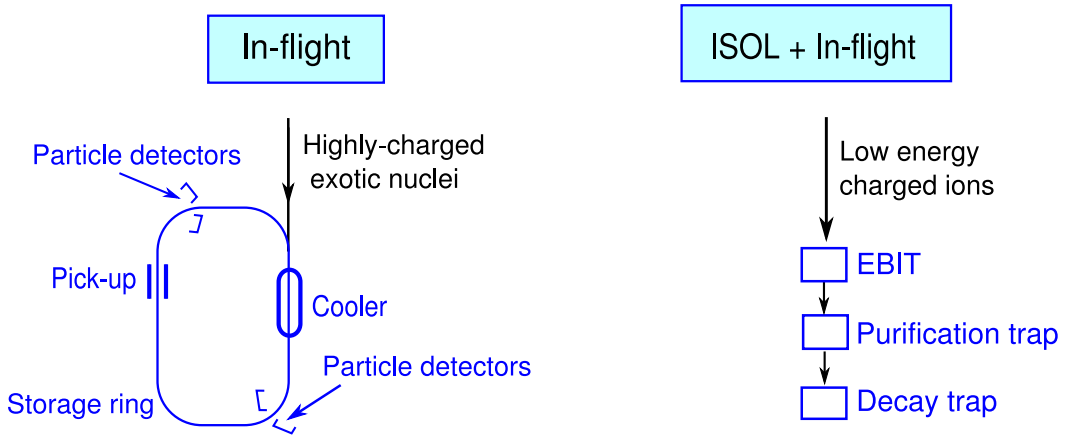

Figure 1.6: Experimental scenario for nuclear lifetime measurement of stored ions with a storage ring (left) and an ion-trap system (right). Note, the setup in front of the storage ring (left) and of the EBIT (right) are the same as discussed with the setup for mass measurement, see Fig.1.4.

1.6.1 Lifetime measurements with ion traps

The exotic nuclei can be produced with ISOL or in-flight method. In case of the in-flight method a gas stopping cell is required to slow the ions down. The interested nuclei from the purification trap will be extracted and stored in the decay trap to observe the decay events.

The decay rate of stored nuclei can be determined by the observation of the emitted γ-rays and particles or by counting the mother and daughter atoms. To detect the γ-rays and emitted particles additional detectors are needed. If the daughter escapes from the decay trap then it will be detected by an additional detector outside the trap.

1.6.2 Lifetime measurements with storage rings

Presently, there is only one ion storage cooler ring, the ESR at GSI, in routine operation with exotic heavy nuclei. Lifetime measurements with the storage ring ESR can be performed with different experimental methods depending on the magnetic rigidity difference $\Delta(B\rho)$ of the mother and daughter nuclei. For small $\Delta(B\rho)$, below 2.5%, both species stay on closed storage orbits and thus can be detected with the pickup as described in the mass measurements section. In this case, the high-resolution Schottky noise power analysis can be applied to measure the intensities of the stored mother and daughter. Furthermore, the decay Q value can be directly obtained by the determination of the mass difference for the mother and daughter. When the daughter exceeds the acceptance of the storage ring due to a large Q value then the daughter nuclei can be detected and identified with additional external particle detectors. In case of only mother nuclei are injected the particle identification in the particle detectors is rather easy.

Both methods have been employed already in pioneering experiments [40, 41] with the ESR. The most precise determination of the decay time can be done with single-particle decay measurements of stored and cooled ions via simultaneous observation of the single mother disappearance and a corresponding daughter appearance [42].

Chapter 2

Experiment

2.1 Production of heavy neutron-rich isotopes

In the present experiment very exotic nuclei were provided for experimental studies using projectile fragmentation and in-flight separation technique. With projectile fragmentation of uranium (^{238}U) almost the full chart of nuclides with Z up to 92 can be covered. In previous experiments U fission in-flight was successfully applied to produce very neutron-rich nuclei in the medium mass region[43, 44]. However, in this work the main goal is to study neutron-rich isotopes in the range Pb – Pa.

2.1.1 Projectile fragmentation

The projectile fragmentation process is well described by the abrasion-ablation model in a participant-spectator picture[45]. This is a two-step process as schematically shown in Fig.2.1. The first step, the abrasion, is a direct collision process between the fast-moving projectile and the target nuclei in the overlap zone. The nucleons in the overlap zone are participants and the others are called spectators. The prefragment which is formed by spectators of the projectile flies forward with nearly the same velocity of the projectiles. The prefragments are normally highly excited due to the direct collision process. The second step is a statistic evaporation process (ablation) which takes a longer time compared to the direct collision processes in the first step. The excited prefragments will de-excite by evaporating γ-rays, nucleons, or even small clusters. Due to the Coulomb barrier, the excited prefragments are more likely to emit neutrons than protons and this generally leads to the production of more nuclei in the neutron-deficient region. Very neutron-rich isotopes can be produced by reaction channels where the prefragments are not highly excited.

2.1.2 Cold fragmentation

Very heavy neutron-rich nuclei can be produced when only protons are removed from the projectiles. This requires that the excitation energy of prefragments has to be low enough to avoid the emission of neutrons. This process is called cold fragmentation. The cold fragmentation mechanism has been experimentally studied at GSI[46]. Details of the model calculations can be found in references[47, 48].

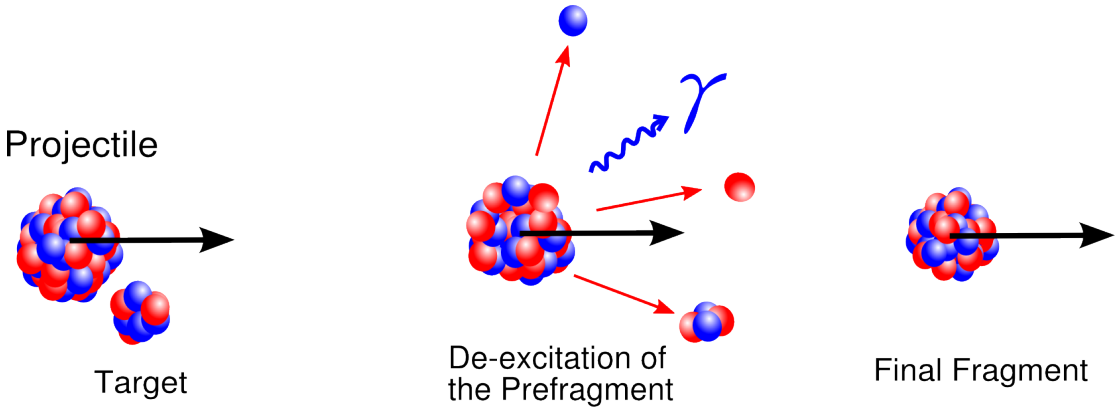

Figure 2.1: Projectile fragmentation: A two-step peripheral heavy-ion collision process.

The excitation energy of the prefragments is proportional to the number of nucleons removed from the projectile. Fig.2.2 shows how the excitation energy is distributed as a function of the removed nucleons. The calculated excitation energy with the Abrasion-Ablation model[47] underestimates the values as concluded in reference[49]. An average excitation energy of 27 MeV per removed nucleon was deduced.
The low-energy tail of the excitation distribution (see Fig.2.2) is responsible for cold projectile fragmentation. The cross sections of cold fragmentation decrease dramatically with the number of removed protons.

2.1.3 Nuclear charge-exchange

The nuclear charge-exchange reaction based on simple nucleon transfer can only happen at low energy. At relativistic energies there are two processes responsible for the charge-exchange reaction – charged π meson exchange or excitation of a projectile/target nucleon into Δ resonance. Charge-exchange reactions at relativistic energy with uranium have been studied experimentally [50, 51].

A charged π meson can be created in relativistic nucleon-nucleon collisions. Relativistic nucleon-nucleon collisions can also populate excited states of nucleon – the Δ particles. For example, the resonance state $\Delta(1232)$ can be populated in the energy region of this experiment. The Δ particle will then decay to a proton or a neutron by emission a π^- or π^+, respectively. The charge-exchange reaction can happen with the following reaction channels:

$$n + p \rightarrow p + \Delta^0 \rightarrow p + p + \pi^- \quad (2.1)$$
$$p + n \rightarrow n + \Delta^+ \rightarrow n + n + \pi^+ \quad (2.2)$$
$$n + n \rightarrow p + \Delta^- \rightarrow p + n + \pi^- \quad (2.3)$$
$$p + p \rightarrow n + \Delta^{++} \rightarrow n + p + \pi^+ \quad (2.4)$$

In the case of converting a neutron to a proton the Z of the isobar is increased by one. For charge-exchange reactions where a proton is converted to a neutron the isobar has $Z-1$.

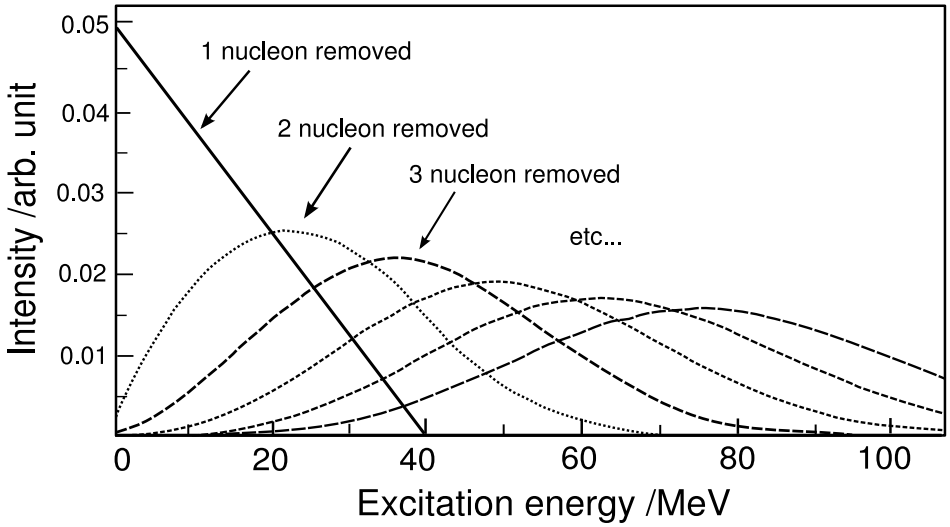

Figure 2.2: Distribution of excitation energy as a function of removed nucleons calculated with the Abrasion-Ablation model[47].

2.2 Population of isomeric states

The study of excited metastable states, or isomers of nuclei, has a long research history and made many contributions to nuclear structure theory. The isomers provide an ideal case for probing the nuclear level structure and thus testing nuclear models. To study the formation of isomers helps to understand the nuclear shell structure, nuclear collective motion and single-particle excitation, nucleon spin and pairing effects. Recently, long lived isomers are even considered as an energy source because in principle, isomers can store much energy (energy trap).

Fig.2.3 presents all long-lived isomers (>1 s) with excitation energies larger than 100 keV[39]. It is obvious that most isomers are observed close to magic numbers, see Fig.2.3. The lack of experimental data in the Po – Pa region is obvious. Using projectile fragmentation of ^{238}U projectiles, isomeric states in this region can be populated. They can be investigated applying SMS if their half-lives are longer than a few seconds.

Nuclear isomers exist in different configurations: Shape isomers, spin isomers and K-isomers[52].

Shape isomer: There is a secondary energy minimum at large elongations. They exist because it is difficult for nuclei to change their special shapes. For some shape isomers, two decay modes are open: the decay to ground state via γ emission and the disintegration by fission.

Spin isomer: The decay to the ground state requires a large change in nuclear spin and therefore, the emitted particle has to carry a large angular momentum.

K-isomer: K is a quantum number which represents the projection of the total nuclear spin along the symmetry axis of the nuclei. The difficulty of changing from high-K states to low-K states is the reason for long half-lives. The K-isomers only exist in axially symmetric, deformed nuclei.

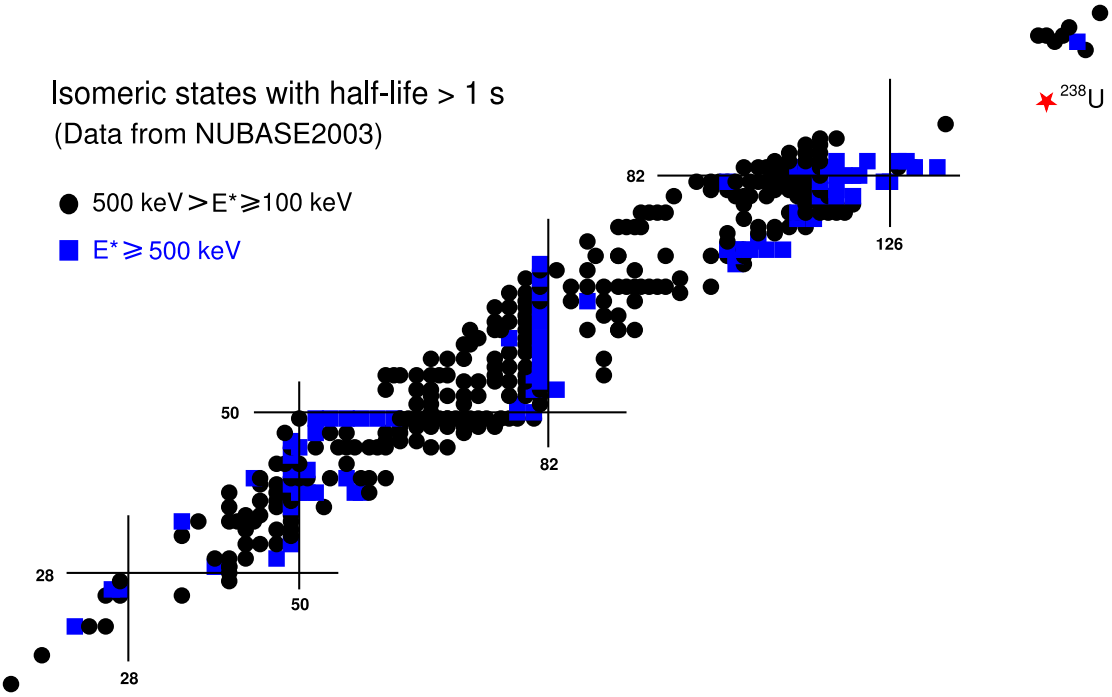

Figure 2.3: Isomeric states in NUBASE2003[39] with half-lives longer than 1 s and excitation energies larger than 100 keV. One can see the lack of experimental data around ^{238}U.

The conventional methods like partial fusion and inelastic scattering are limited to the population of isomers close to the valley of stability, while projectile fragmentation is a more versatile tool to produce isomers[53, 54]. The conventional isomer identification is based on coincidence measurement between the identified fragments and the emitted γ-rays. This method is often limited to short-lived isomers ($<$1 s). The Schottky Mass Spectrometry is ideally suited for long-lived ($>$1 s) isomers circulating in the storage ring.

2.3 In-flight separation with the FRS and injection into the ESR

A 670 MeV/u $^{238}U^{73+}$ primary beam provided by the GSI heavy-ion synchrotron SIS with intensities up to $2{\cdot}10^9$/spill was focused on a $4g/cm^2$ ^{9}Be production target to produce neutron-rich fragments. The hot fragments were separated in flight[55, 56] by the FRS and transferred to the ESR.

The magnetic rigidity of FRS and ESR was kept constant to 7.9 Tm during the whole experiment. The produced relativistic heavy fragments are highly charged which means fully stripped or carrying only a few electrons. The fragments injected in the ESR were stored and cooled by electron cooling. A Schottky pick-up was installed to measure the revolution frequency of the circulating ions. The complex experimental setup of this experiment is shown in Fig.2.4.

The large storage acceptance of the ESR ($\pm$1.25%) allows a simultaneous measurement of a large range of mass-to-charge ratios. Stored single ions with charge states

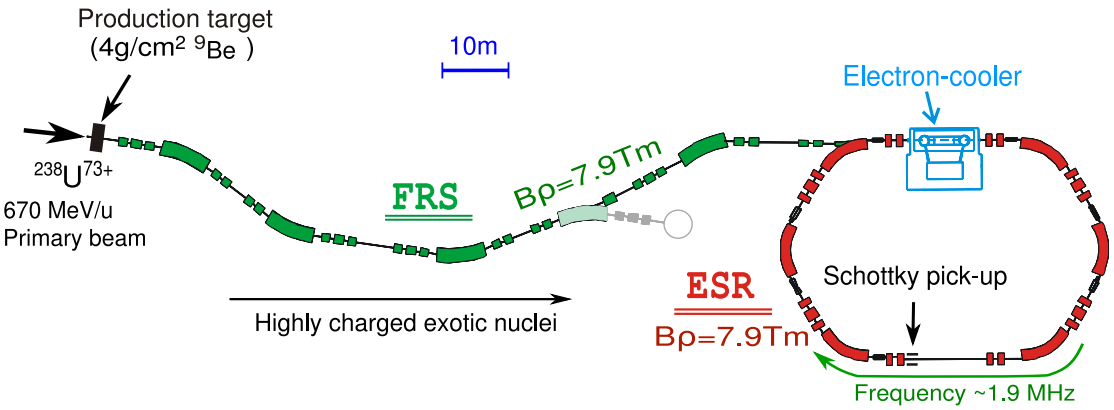

Figure 2.4: Scheme of the experimental setup of this experiment.

down to about $q = 40$ can be measured by the Schottky pick-up.

2.4 Cooling process of hot fragments

The hot fragments, typically characterized by a momentum spread of $\sim 1\%$ before injection, were cooled by electron cooling[57, 58] after injection. A cooling time of a few seconds was achieved in the present experiment. The cooling process is most efficient and fast for fragments with velocities close to the selected velocity of the cooler electrons. The cooling time t_{cool} is directly proportional to the corresponding velocity difference of the cooler electrons and the hot fragments to the power of three ($t_{cool} \propto (\Delta \mathrm{v})^3$).

The $B\rho$ acceptance of the ESR determines the m/q window where ions can be simultaneously stored:

$$B\rho = \frac{m\mathrm{v}}{q}, \tag{2.5}$$

where v is the mean ion velocity in the ESR which is determined by the electron cooler:

$$\mathrm{v} = c \cdot \sqrt{1 - \frac{1}{(\frac{eU_{eff}}{m_e C^2} + 1)^2}}, \tag{2.6}$$

where m_e and c are the rest mass of the electron and the speed of light in vacuum, respectively. e is the elementary charge and U_{eff} is the effective cooler voltage. U_{eff} is a correction of the cooler voltage U for the space charge effects in the electron beam:

$$U_{eff} = U - \frac{113 \cdot I}{\sqrt{1 - (\frac{eU}{m_e C^2} + 1)^{-2}}}, \tag{2.7}$$

where I is the cooler current in Ampere, U and U_{eff} are given in units of volt. The cooling process is demonstrated in Fig.2.5. Only a small part of the ESR storage acceptance is filled at the beginning of the injection because the injection acceptance is much smaller. All ions are cooled to an identical mean velocity. The velocity spread of the circulating fragments can be reduced down to $5 \cdot 10^{-7}$ for low intensity. Finally the

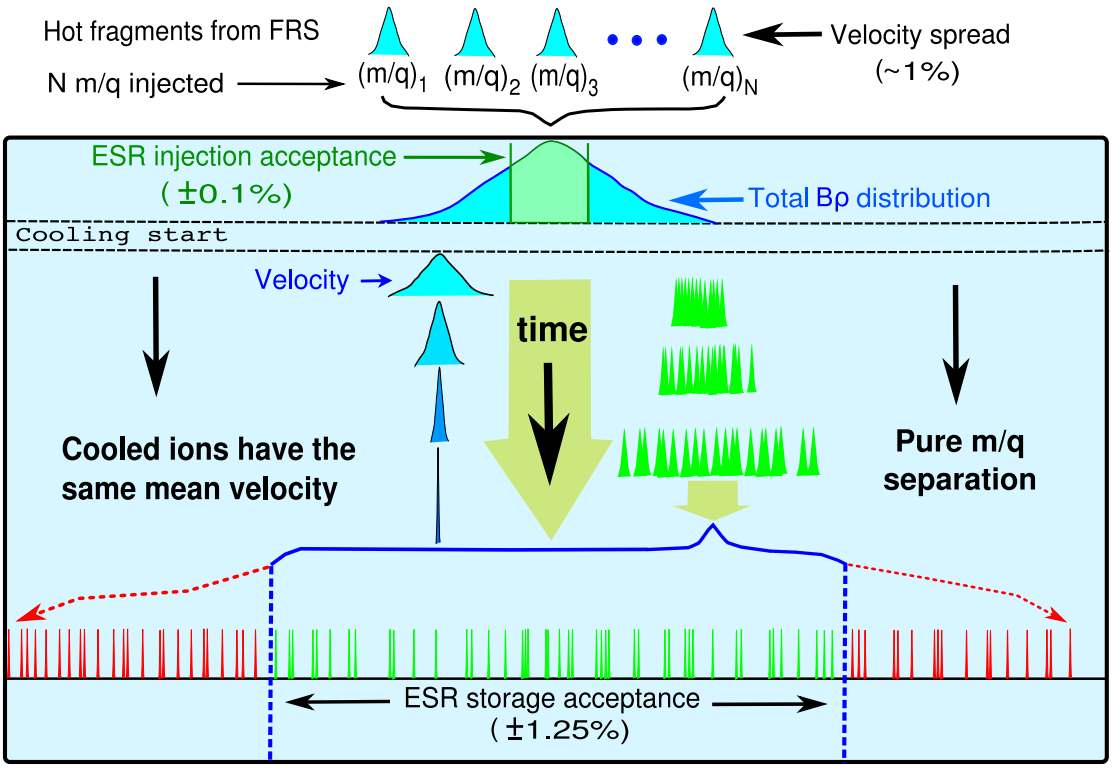

Figure 2.5: Ion cooling and mass-to-charge separation in the storage ring. A new cooler voltage can be applied to access a different mass-to-charge ratio region.

ESR storage acceptance will be full filled with cooled ions and some ions will be lost due to the acceptance.

2.5 Schottky noise signals

The signals induced by the circulating charged ions on the metallic pick-up provide a powerful tool for monitoring the beam in accelerators and storage rings[59]. This so-called Schottky noise signal results from a large number of randomly distributed fast moving ions in the ring. The time dependent current signal of a single stored ion with revolution frequency f_0 and charge q is:

$$I(t) = qf_0 + 2qf_0 \sum_{h=1}^{\infty} cos(2\pi h f_0 t). \tag{2.8}$$

The Fourier transformation of $I(t)$ leads to a frequency spectrum which shows a sharp peak at each harmonic. For a coasting beam with N randomly distributed ions (of the same species) which all have the same revolution frequency f_0 in the storage ring, the total signal is a sum of (2.8) over the N ions. Due to the random phase (θ_n) of ion motion in the ring, this will only lead to a DC component. For a given harmonic band of the frequency spectrum, the root-mean-square current is:

$$I_{rms} = 2qf_0\sqrt{(cos^2\theta_1 + cos^2\theta_2 + \cdots + cos^2\theta_N)^2} = 2qf_0\sqrt{N/2}. \tag{2.9}$$

This means there is a non-zero power in each frequency band which is independent of the harmonic number and proportional to the square root of the number of ions. The

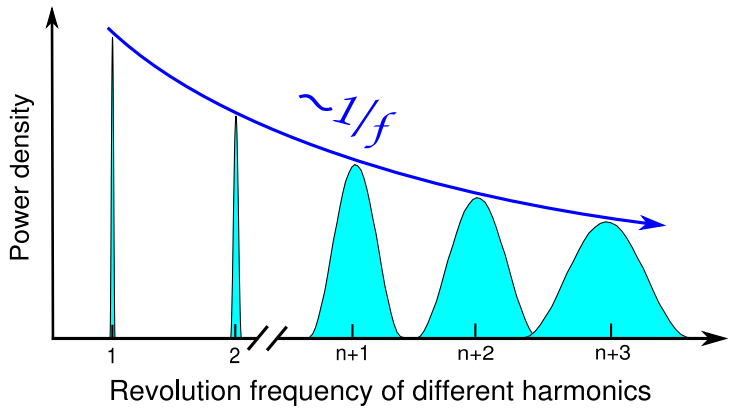

Figure 2.6: Power density spectrum of Schottky noise signals of stored ions. The power density is inverse proportional to the harmonic number while the total power is constant in all harmonic brands. The width of the bands are proportional to the number of harmonics.

power spectrum density $P(f)$ which can be measured with the pick-up and following spectrum analyzer is given by:

$$P(f) = Z_t \frac{I_{rms}^2}{\Delta f} = \frac{2Z_t f_0^2}{\Delta f} N q^2, \tag{2.10}$$

where Z_t is the transfer impedance from current to voltage and Δf is the width of the frequency band which is proportional to the harmonic number. The noise power density is proportional to Nq^2 and inverse proportional to the harmonic number. The total noise power is constant at each harmonics.

The peaks in the power density spectrum will be normally well separated and overlap only at very high harmonics, see Fig.2.6. When K different species (with mass $m_1, m_2, \cdots, m_K$) are stored in the ring there will be K corresponding peaks (with frequencies $nf_1, nf_2, \cdots, nf_K$) in each harmonics n. In our experiment we use the 31^{st} harmonics for technical reasons. Note, the resolving power is independent of the selected harmonics.

2.6 Schottky Mass Spectrometry (SMS)

Schottky Mass Spectrometry (SMS)[36] was developed at GSI to perform high precision mass and half-life measurements of heavy ions using the unique combination of the fragment separator FRS and the experimental storage ring ESR. Mass and half-life measurements of exotic nuclei with SMS have been very successful as demonstrated by previous experiments[60, 61, 62]. Figure 2.7 shows the schematic picture of the ESR and the principle of Schottky Mass Spectrometry.

The mass and half-life were determined by analyzing the Schottky noise signals of the stored charged ions in the ESR. The task in this work is to perform the measurement of power-density spectra of cooled stored ions, to analyze Fourier transformed spectra and to evaluate the masses and the half-lives. The velocity v and corresponding orbital

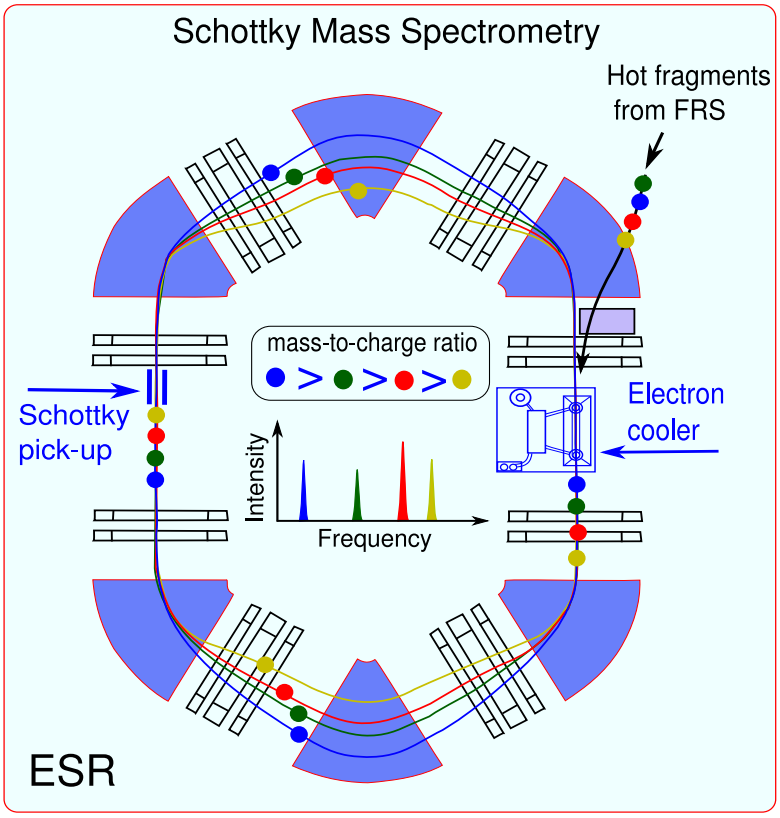

Figure 2.7: Principle of Schottky Mass Spectrometry.

length C of stored ions in the ESR determines the revolution frequency $f = \mathrm{v}/C$. The orbital length is related to the magnetic rigidity $B\rho$ by:

$$\frac{dC}{C_0} = \gamma_t^{-2} \frac{d(B\rho)}{(B\rho)_0}, \tag{2.11}$$

where C_0 and $(B\rho)_0$ are the orbital length and magnetic rigidity of the reference ions, respectively. γ_t is an ion-optical parameter of the ESR and $B\rho = \gamma \mathrm{v} m/q$, where m/q is the rest mass-to-charge ratio of the ion. The dependence of f on v and m/q can be expressed by:

$$\frac{df}{f} = -\gamma_t^{-2} \frac{d(m/q)}{m/q} + (1 - \frac{\gamma^2}{\gamma_t^2}) \frac{d\mathrm{v}}{\mathrm{v}}. \tag{2.12}$$

For high-precision mass measurement the last term of equation (2.12) has to be reduced to a negligible level ($< 10^{-6}$). This is done by using electron cooling to compress the velocity spread to a value about $d\mathrm{v}/\mathrm{v} < 10^{-6}\ d\mathrm{v}/\mathrm{v}$. When all the stored ions are well cooled, the frequency relation between two different ions with masses i and j is:

$$\frac{f_i - f_j}{f_i} = -\alpha_p \frac{(m/q)_i - (m/q)_j}{(m/q)_i}, \tag{2.13}$$

where α_p is the *momentum compaction factor* which is an ion optical parameter and is defined by:

$$\alpha_p = \frac{1}{\gamma_t^2} = \frac{dC/C}{d(B\rho)/(B\rho)}. \tag{2.14}$$

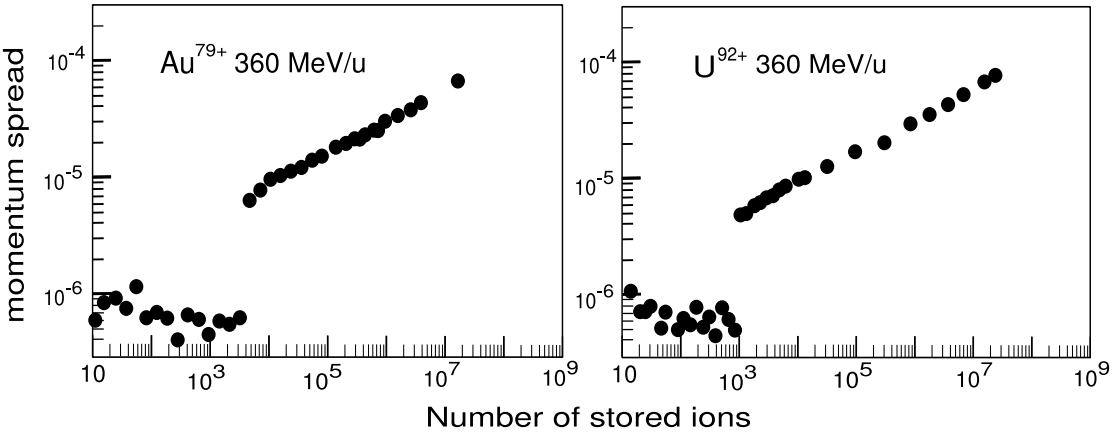

Figure 2.8: Measured momentum spread as a function of the number of stored charged ions. The ions were cooled with electron cooling applying a current of 250 mA. Pictures are taken from reference [64]

.

Equation (2.13) connects the revolution frequency measurement and mass determination directly and explains the basic principle of SMS measurements.

The measured frequency spread (δf) of stored ions determines the sensitivity and the resolving power of SMS. The frequency spread of mass i is determined by its velocity spread (δv):

$$\frac{\delta f_i}{f_i} = (\frac{1}{\gamma_i^2} - \alpha_p)\,\gamma_i^2\,\frac{\delta \mathrm{v}_i}{\mathrm{v}_i}, \tag{2.15}$$

With the electron cooling applied, γ_i is determined by the velocity of the electrons from cooler and $\delta \mathrm{v}_i$ depends on the balance between the cooling force and heating effects from intra-beam scattering. The in-beam heating effects are proportional to the number of stored charged ions. Fig.2.8 shows how the measured momentum spread changes with decreasing number of stored ions in the ESR. The momentum spread ($\delta p/p$) smoothly drops with decreasing numbers of stored ions if the stored ions are much more than thousand. A dependence of $\delta p/p \propto N^x$ was observed in ESR, where N is the number of stored ions and $0.3 \leq x \leq 0.7$ depending on cooling conditions[63]. A sudden drop of momentum spread was observed when the number of ions decreased to a few thousands. This sudden drop is due to the change of the ion motion to a one-dimensional ordering state[64]. All the ions are then moving like a chain and can not pass each other. The momentum spread can not decrease further with a decreasing number of ions. Presently the limitations are given by the short-term instabilities of the ESR magnet fields.

As proved by our previous measurements, SMS is a powerful tool for direct mass and half-life measurements of stored ions. The characteristics of SMS are summarized in the following:

Mapping power Ions within a large mass-to-charge ratio range can be simultaneously stored and measured. This makes it easier to perform large-scale measurements on the chart of nuclei.

Sensitivity Sensitivity down to stored single ions in the ESR. This is very important

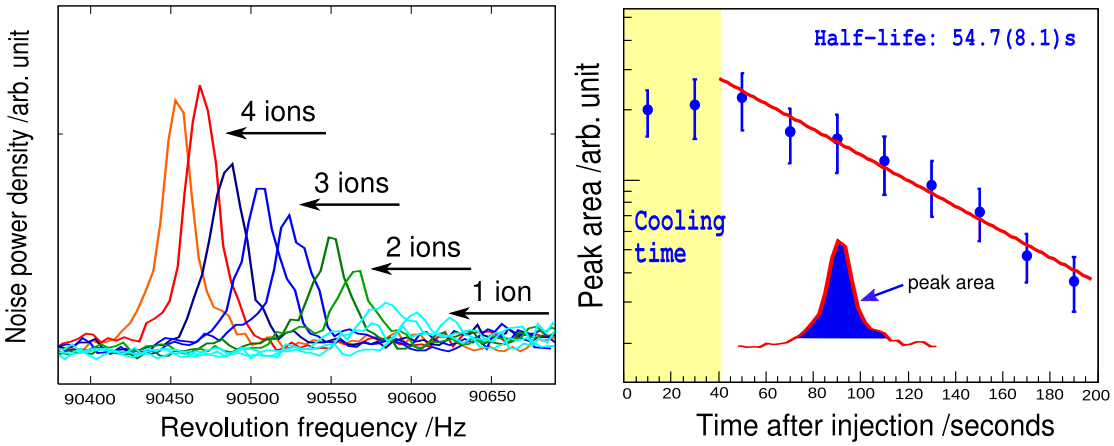

Figure 2.9: The principle of nuclear half-life measurement with SMS. The Schottky noise signals of $^{235}Ac^{88+}$ is plotted in the left panel and the corresponding number of stored ions are marked. The fitting of peak areas and the half-life results is shown in the right panel.

for measuring isotopes with very small production cross sections.

Resolving power The measured resolving power can reach up to $2 \cdot 10^6$ and thus makes it possible to separate nuclear isomeric states with small excitation energies (about few hundreds keV).

Simultaneous measurement of mass and half-life With SMS both the masses and half-lives of the stored ions can be simultaneously measured. Presently, ions with half-lives longer than a few seconds can be studied.

2.7 Mass and half-life measurements with SMS

Applying equation (2.13) the unknown mass can be in principle determined via measurements of the revolution frequencies. To determine an unknown mass at least two reference masses are needed because the α_p parameter is not constant and has to be calibrated for different m/q ranges. Since SMS covers a large range of m/q in one experiment, the masses can be evaluated with the matrix method, see details in section 3.5.1. A big advantage of SMS is that known and unknown masses are simultaneously measured under identical experimental conditions.

As mentioned in section 2.6, one of the advantages of SMS is that the half-life information of stored ions can also be extracted from the raw data. The Schottky noise power of peaks in the frequency spectrum is proportional to the number of ions. Therefore, the decay rate of interested isotope in the ring can be obtained via the measurement of the Schottky noise power as a function of time. Since the signals of stored ions are continuously measured until the ions are lost in the ring, the half-life of stored ions can be extracted from the time-resolved Schottky noise power density spectrum.

The principle of half-life evaluation is demonstrated in Fig.2.9. In the left panel the Schottky noise power signal of ^{235}Ac in one injection is plotted. The right panel shows the half-life results for ^{235}Ac using the data in this injection. The first 40 seconds of injection is excluded from the half-life fit because the ions are still in the cooling

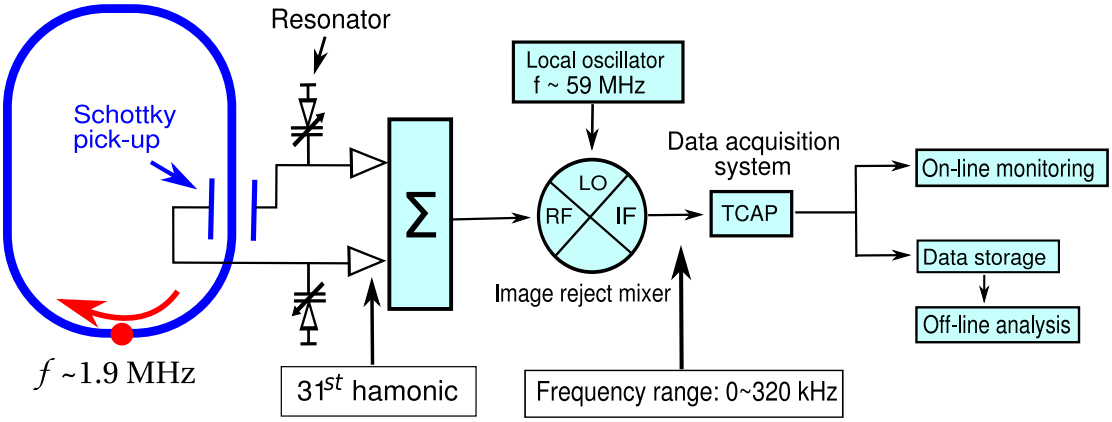

Figure 2.10: Data acquisition of SMS.

Cooler voltage (kV)	Centered m/q	Centered ions
190	2.682	$^{236}Th^{88+}$, $^{234}Ac^{87+}$, $^{231}Ra^{86+}$
192	2.668	$^{235}Ac^{88+}$, $^{230}Ra^{86+}$, $^{227}Fr^{85+}$
194	2.654	$^{231}Ra^{88+}$, $^{228}Fr^{86+}$, $^{223}Rn^{84+}$
196	2.639	$^{227}Ra^{86+}$, $^{230}Fr^{87+}$, $^{222}Rn^{84+}$
198	2.627	$^{226}Rn^{86+}$, $^{223}At^{85+}$, $^{221}At^{84+}$
200	2.609	$^{227}Fr^{87+}$, $^{224}Rn^{86+}$, $^{219}Po^{84+}$

Table 2.1: The cooler voltage settings and corresponding centered ions.

process. The mean value from the half-lives obtained from the individual injections was calculated taking into account the losses due to atomic interaction in the ring.

2.8 Experimental conditions and data acquisition

The 31^{th} harmonic signals from the pick-ups were summed and down converted to a frequency range of 0∼320 kHz by an image-reject mixer. The converted signals were treated by a Time CAPture system TCAP (See Fig.2.10). The signals from TCAP were split into two parts, one for on-line monitoring and one for the data storage. Once triggered, the data acquisition system TCAP will start to continuously record the raw data including the time correlation. The digitized data from the ADC were stored and formatted in blocks each corresponding to 0.1 s. Each block includes a header information where the time of measurement and cooler settings are stored as well.

Since fast cooling is critical for the access of isotopes with short half-lives, the cooler voltage has to be optimized to match with the electron velocity the mean velocity of the fragments of interest. As discussed in section 2.4 only part of the fragments from the injection can be finally stored after cooling. To map the whole injection acceptance, the cooler voltage was scanned from 190 kV to 200 kV with 2 kV steps. Table 2.1 lists the cooler voltage settings in this experiment and the corresponding isotopes which are expected to be at the center of the frequency spectrum.

Chapter 3

Data analysis

3.1 Schottky frequency spectrum of stored ions

3.1.1 Generation of the frequency spectrum

The first task of the off-line data analysis is to convert the raw data into frequency spectra using a Fast Fourier Transformation (FFT) algorithm. As mentioned in section 2.8 the raw data were stored in blocks of about 0.1 s. The full span of the frequency spectrum is 312.5 kHz which is determined by the sampling rate of the data acquisition system. To optimize the quality of the frequency spectrum two aspects have to be carefully considered – the channel width in the frequency spectrum and the number of blocks to be averaged.

Channel width By summing and combining different numbers of data blocks, a frequency spectrum with different channel (bin) widths can be produced. This determines the frequency resolution. Because the noise power of the peaks is proportional to the number of stored ions, changing of the channel width does not change the peak areas. For the best analysis condition a channel width of 4.768 Hz was used in this work. This means always 2 raw blocks were combined into one block. The final block length for FFT corresponds to about 0.2 s recording time and the produced frequency spectrum contains 65536 channels.

Average number To get an optimal signal-to-noise ratio a certain number of frequency spectra have to be averaged. In Fig.3.1 the frequency spectra of the same data sampled with different average numbers are displayed. The single ion signal is totally invisible with an average number 2. The width of the background decreases with increasing average number which makes an single-ion signals possible to be observed. On the other side, the more spectra are averaged the more time information in the spectra is lost. In this work an optimization for the detection of single ions was made using an average number of 100 which corresponds to 20 s per produced spectrum.

Around 10000 frequency spectra were generated and analyzed in this work. Frequency spectra with less average numbers are also generated in case the time determination has the priority. For example, for the determination of the half-lives, more data points were required with less average numbers. A typical Schottky noise power spectrum is shown in Fig.3.2.

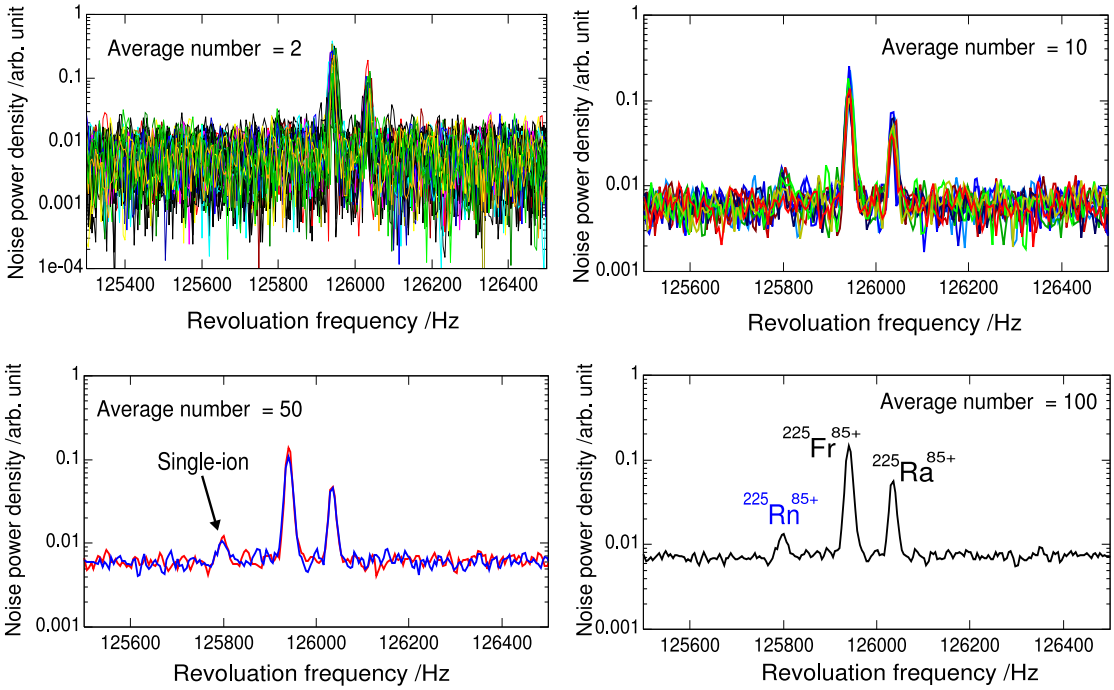

Figure 3.1: Comparison of Schottky noise spectra produced with different average numbers using the same raw data. Less averages show a much wider background. Each spectrum corresponds to about 0.2 s before the averaging has been applied. With an average number of 100, the signal-to-noise ratio has improved by a factor of 10 compared to the raw spectrum.

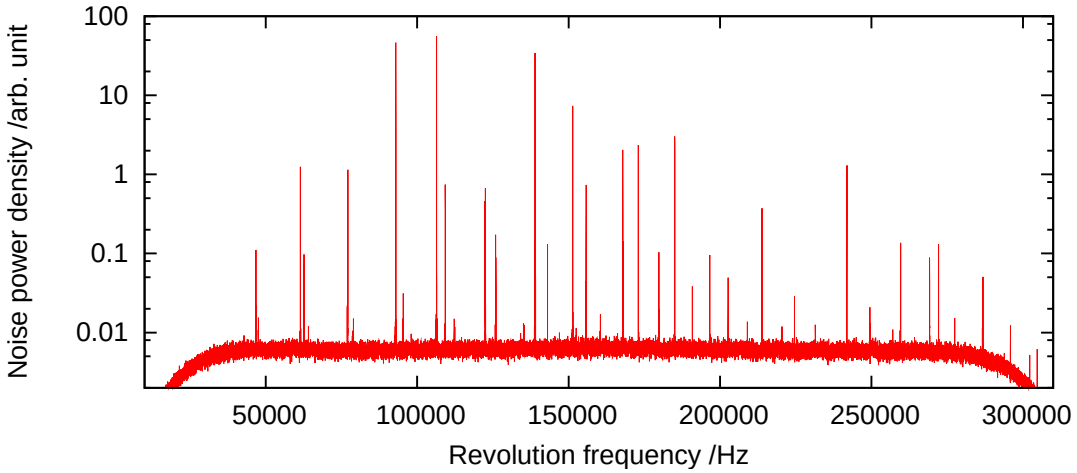

Figure 3.2: A typical Schottky noise power spectrum recorded in this experiment. The frequency span is 312500 Hz and the channel width is 4.768 Hz.

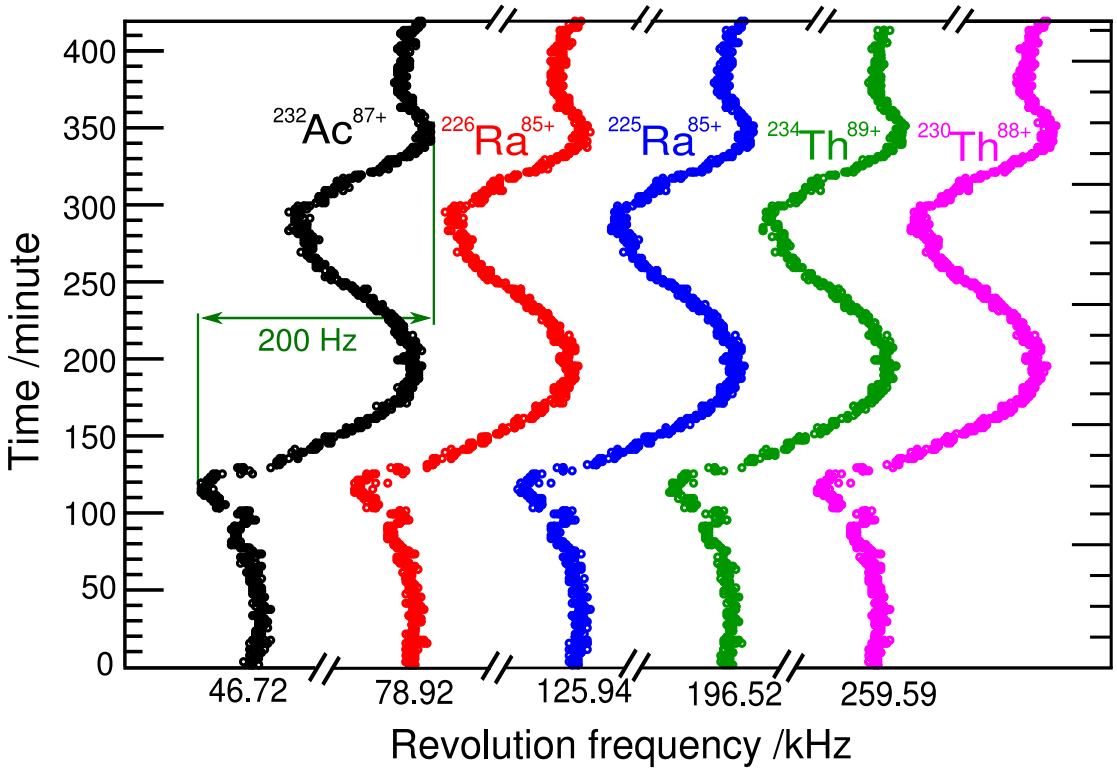

Figure 3.3: The time trace of the revolution frequency for one setting of the electron cooler. The time of the measurement was about 420 minutes.

3.1.2 Frequency drifts

The frequency drifts caused by short-term instabilities can be one limitation for the precision of our mass determination in SMS experiments. The revolution frequencies of the stored ions were slowly drifting due to instabilities of the magnetic fields and the cooler voltage. Large frequency drifts up to a few hundreds Hz (at 31^{st} harmonic) were observed. Fig.3.3 shows an example of the observed drift of the revolution frequency in one experimental setting. The data in Fig.3.3 were measured with a cooler voltage of 198 kV and a current of 400 mA. As shown in Fig.3.3, the frequency peaks of the different ions in a large m/q range drifts in the same way. In principle, this systematic frequency drift can be determined and corrected and was done in this work.

The overall uniform frequency drifts of all peaks in the same spectrum can be verified by the determination of the relative frequency drifts between different peaks. In fact, the relative frequency drifts in the same spectrum is crucial for the obtained mass resolution. The change of the relative frequency drifts could be caused by imperfections of the magnetic fields or space-charge effects in the ring. Fig.3.4 shows the distribution of the measured frequency difference for different couples of ions in the same spectrum. A range of different frequency differences is selected and plotted in Fig.3.4. The result is that the observed drift is constant over the full span of the spectrum. This confirms that the revolution frequency of all stored ions drift homogeneously as a function of time.

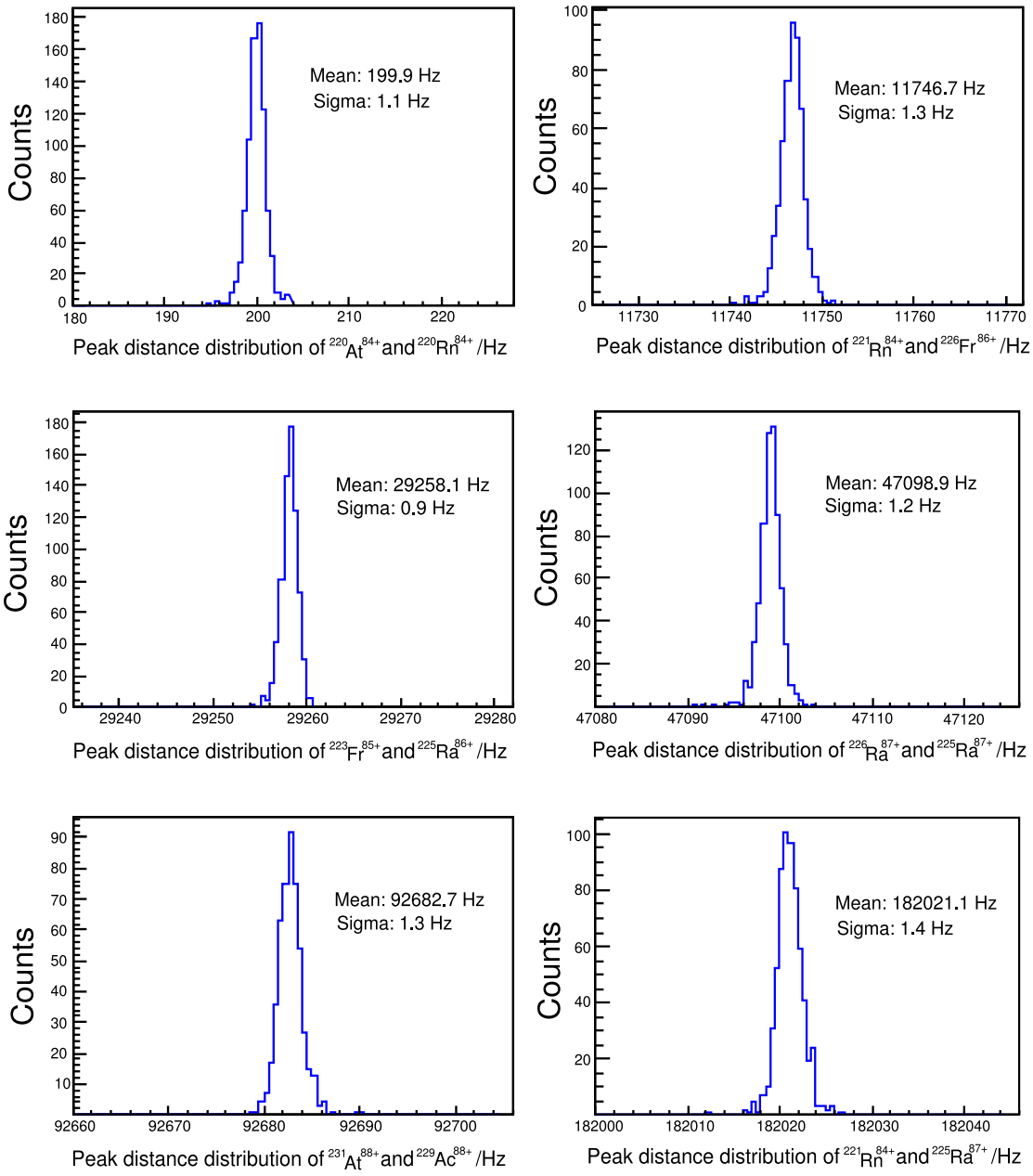

Figure 3.4: Distribution of the measured peak distance between two different ions in the same spectrum. Different couples of ions with a peak distance in the frequency range from 200 Hz to about 182 kHz were displayed. The width (standard deviation σ) of the distribution of the frequency difference is almost constant over the full frequency range. The time of the measurement was about 420 minutes.

3.1.3 Mixtures in the Schottky frequency spectrum

A frequency mixture of two ions with a close mass-to-charge ratio was often observed in this experiment. The reason can be schematically explained by Fig.3.5. All cooled stored ions in the ring have an identical mean velocity. The ions with smaller m/q have a shorter orbital length and thus a higher revolution frequency compared to the ions with a larger m/q. Therefore the ions with a smaller m/q have to overtake the ions with a larger m/q in the ring. In case the m/q difference is large enough thus a large radial distance exists between the ions it means they can move independently in the ring as shown in Fig.3.5 A and the measured revolution frequency of both ions represents the true value for m/q. When the m/q difference between two ions is getting smaller the Coulomb interaction between them becomes stronger due to the smaller radial distance. In case the radial distance is small ($\lesssim 50\,\mu m$ [65]) then the Coulomb interaction will prevent the lighter ions to overtake the heavier ion. Thus the two ions will move together like a cluster (Fig.3.5 B). This kind of coupled motion of stored charged ions happens very frequently due to the multiple charged heavy ions with their close m/q values were stored.

The blocked ion cluster generates in the Schottky pick-up a signal corresponding to the sum of the charge state of those two ions. Because the Schottky noise power is proportional to the square of the charge state, a sudden increase of noise power can be seen when such a mixture happens. The coupling of the stored ions can be disentangled by some random disturbance which cause that the frequency peaks of the two ions are separated again.

Fig.3.6 shows examples of different mixtures which were observed in this experiment. A: $^{237}Pa^{89+}$ and $^{237}U^{89+}$ were moving independently at the beginning of injection and the mixtures started at about 80 s after the injection. B: $^{237}Pa^{89+}$ and $^{237}U^{89+}$ were mixed for about 80 s in the middle of injection and then separated again. C: $^{232}Ra^{87+}$ and $^{232}Ac^{87+}$ were mixed right after the injection and after 160 s the mixture disappeared and consequently two lines were observed. D: $^{226}Rn^{84+}$ and $^{226}Fr^{84+}$ were mixed at the beginning of injection and after about 100 s the $^{226}Fr^{84+}$ ion was lost thus the true line of $^{226}Rn^{84+}$ can be observed.

It is obvious that such mixtures have to be found and to be excluded from the mass analysis. However, it is easy to identify such mixtures due to the random jitter of the mean frequency and the corresponding larger width compared to 'normal' peaks.

3.2 Analysis of frequency peaks

A fast program was used to search all peaks in the frequency spectra. Very exotic nuclei were presented by very weak/small peaks in the frequency spectra, therefore, it was very important to detect such peaks. This required that the threshold for peak searching has to be a very low value.

Selecting a low peak searching threshold it was unavoidable to have some background contribution. There were also some spurious peaks which came from electronic noise. To get a clean spectrum for peak identification the background, spurious peaks

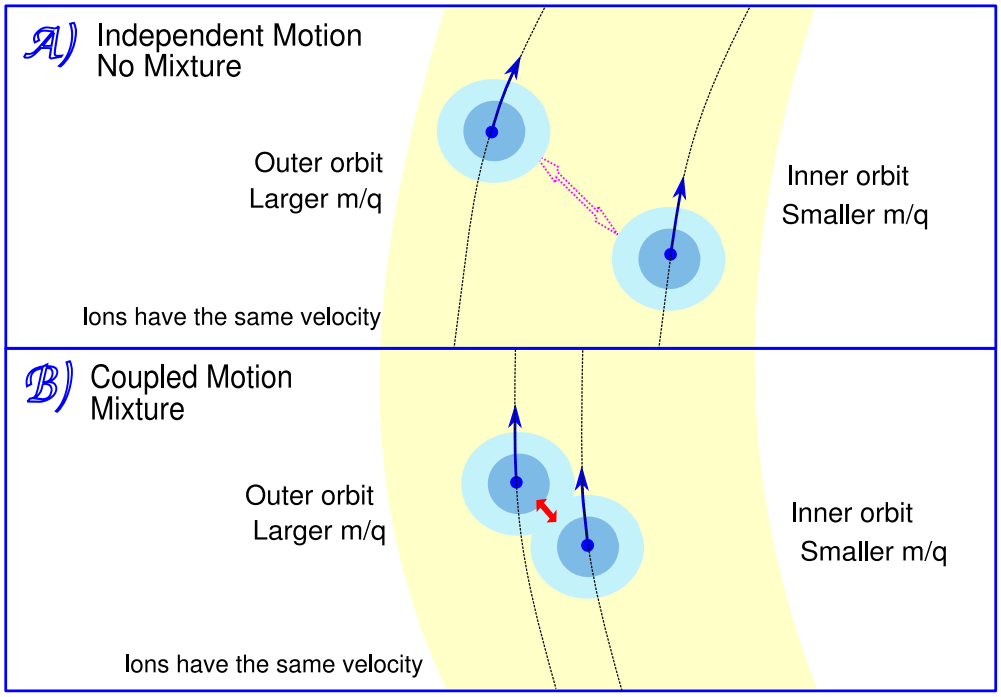

Figure 3.5: Frequency mixture happens when two ions have a very close mass-to-charge ratio corresponding to a mass difference $\lesssim 2$ MeV (corresponding to a frequency difference about 100 Hz). A model calculation of this phenomenon can be found in reference [65]

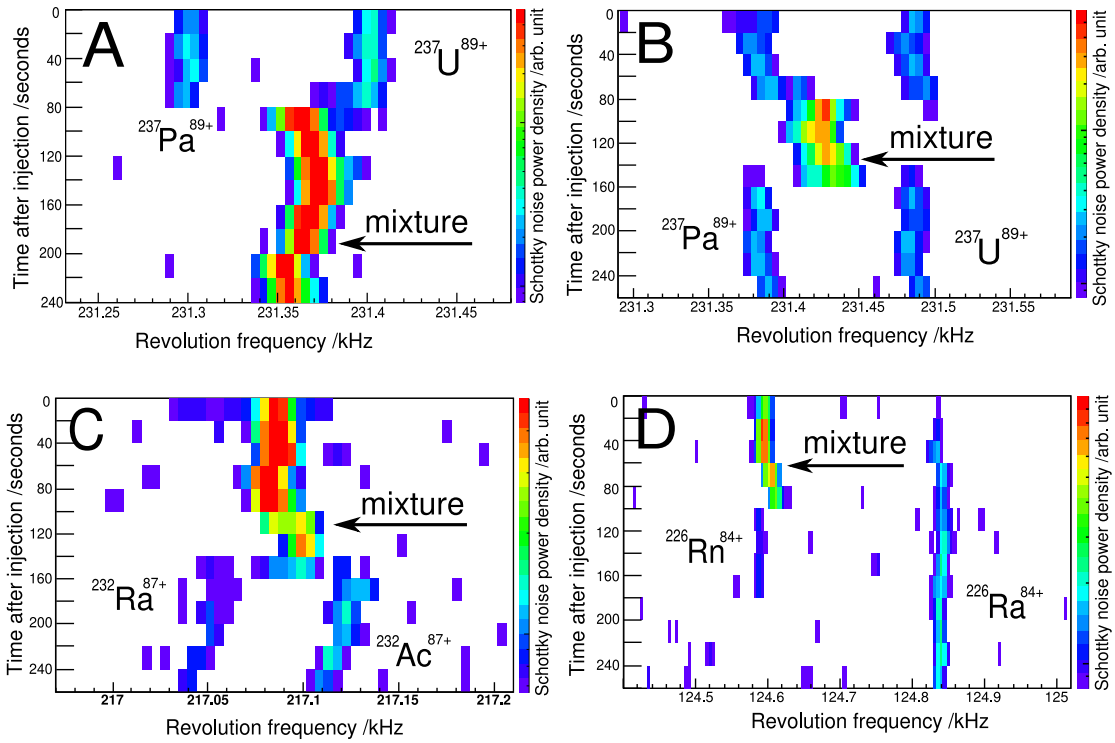

Figure 3.6: Mixture of ions with close mass-to-charge ratios. The mass difference between ^{237}Pa and ^{237}U, ^{232}Ra and ^{232}Ac, ^{226}Rn and ^{226}Fr are about 2.15 MeV, 1.36 MeV and 1.21 MeV, respectively.

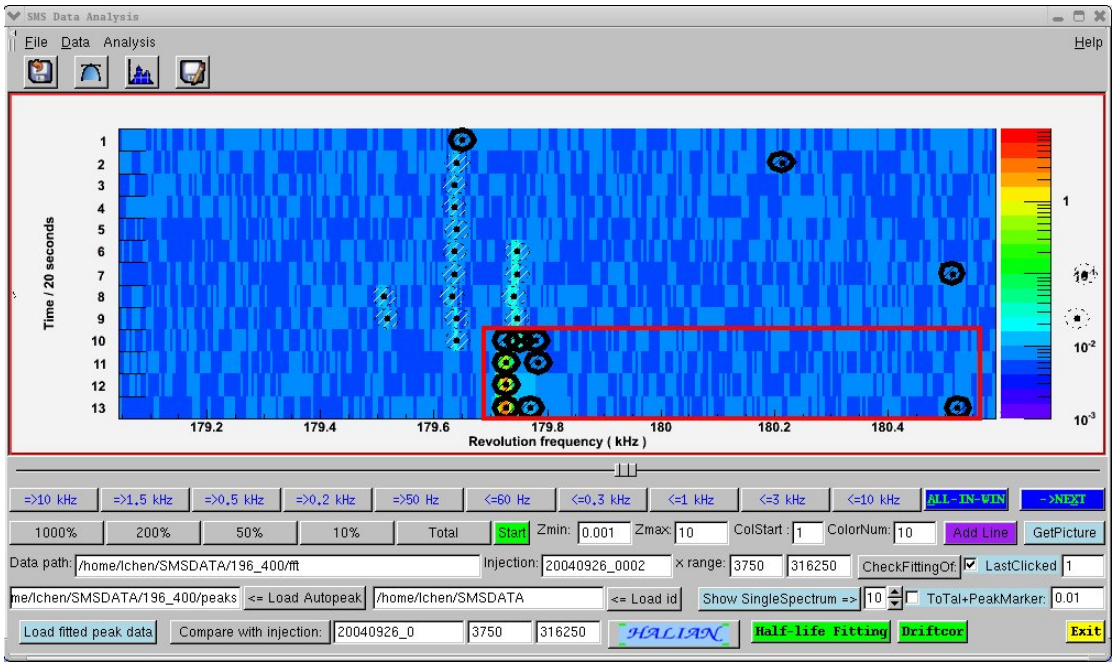

Figure 3.7: A screen shot of the new analysis software developed in this work. Part of the Schottky noise spectrum from one injection is displayed. Each black point corresponds to a peak candidate in principle. The points marked with a black open circle indicates mixtures, background noise and incompletely cooled ions which are all excluded from further analysis.

and the mixtures were excluded from the final analysis. For this a special software was developed within the present work. Fig.3.7 shows a screen shot of this program package. All the peaks which 'survived' from the peak selection were fitted with a Gaussian function to find the mean values and the corresponding uncertainties.

3.3 Projection of frequency spectra

The idea is to project all spectra recorded under the same experimental conditions into one spectrum and to perform the identification. The advantage is that the time for identification can be shortened in this way.

The frequency drifts have to be calculated and a correction of the systematic drifts must be applied to project all individual spectra of one setting into one spectrum. A spectrum which contains most of the peaks in each setting was selected as the reference spectrum and the relative frequency drifts of all other spectra were calculated accordingly. The calculation was done by shifting each spectrum relative to the reference spectrum to look for the best matching between them. The drift value of each spectrum related to the reference spectrum can be found when the best overlap was reached. Given the calculated drift values, the projection of all spectra can be done.

Fig.3.8 shows a part of such a projected spectrum measured with a cooler voltage of 196 kV and a cooler current of 400 mA. The FWHM of the peaks in the projected

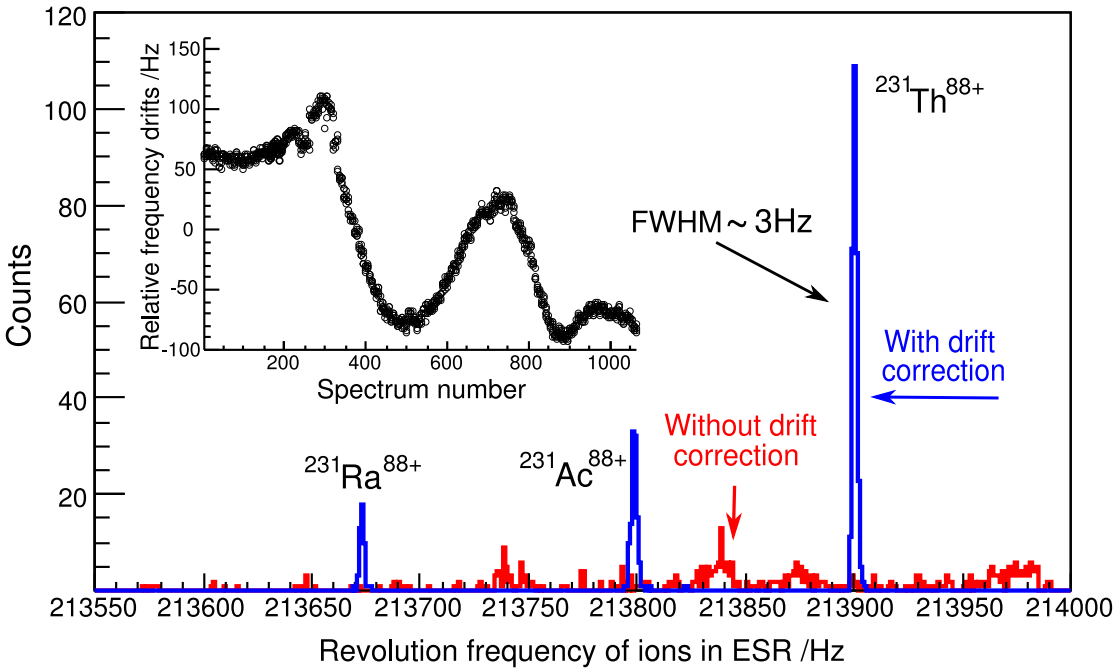

Figure 3.8: Spectrum generated by the projection of 1067 spectra recorded under the same experimental conditions. Only a small part of the spectrum is displayed.

spectrum is about 3 Hz. In Fig.3.8 the projected spectra with and without drifts correction are plotted. The quality of the peaks in the drift-corrected projected spectrum demonstrates that the systematic frequency drifts were well corrected. The calculated correction values are displayed in the inner panel of Fig.3.8 .

3.4 Peak identification

The peak identification was done in the following way. First of all a full list contains all possible candidates was prepared from which the corresponding identifications for different settings were found. All the isotopes which could be produced by fragmentation or fission of relativistic U were considered. Not only known isotopes from AME2003[10] but also predictions from a theoretical model (FRDM[11]) were included for identification. The number of candidates for a specific experimental setting was dramatically reduced by considering the following experimental conditions:

Charge state Considering the high energy and heavy fragments in this experiment, charge states from 0 up to 5 electrons were taken into account. Most of the ions have one, two or three electrons. Heavy ions with 5 electrons in this experiment are very rare and actually ions with 5 electrons are observed in 3 injections with one stored single ion.

Half-life Isotopes with half-lives shorter than milliseconds were not taken into account because of the relatively long time needed for electron cooling.

m/q window This is determined by the FRS-ESR magnetic field setting. The magnetic rigidity selection defines the measured central m/q value whereas the ESR accep-

tance determines the width of the m/q window. All candidates outside this m/q window were not considered for identification.

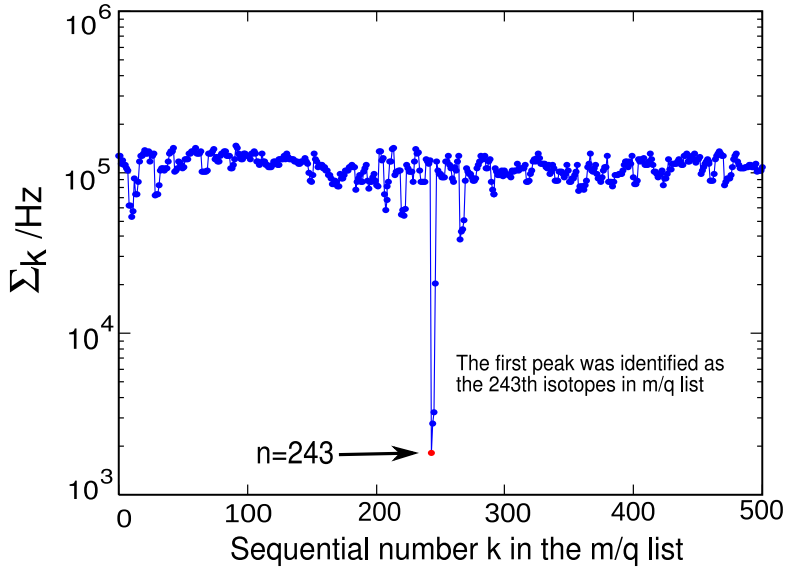

Figure 3.9: The identification was done by searching the best matching between the measured spectrum and a theoretical frequency spectrum. In this case when the 243^{rd} isotope in the m/q list assigned to the first peak of experimental spectrum the whole experimental spectrum yields the best overlap with the theoretical frequency spectrum.

If we denote each peak in the experimental spectrum by f_i with $0 \leq i < N$ and each m/q values in the candidates list by $(m/q)_j$ with $0 \leq j < M$, a theoretical frequency spectrum can thus be simulated using the m/q list by given the $(m/q)_k$ candidate the frequency f_0. Now we can find the peak in the simulated spectrum which have the smallest frequency difference to experimental peak f_i and denote this peak as f_i^j. The sum of the frequency difference $\sum_{i=0}^{N-1}(f_i - f_i^j)$ represents how well the simulated spectrum can be matched with the experimental spectrum and we denote this sum by $\sum_k$. This was done for the complete list of candidates and in this way we found the minimum values for $\sum_k$. Fig.3.9 shows an example of $\sum_k$ as a function of the sequential number k. In Fig.3.9 the best matching (minimum of frequency difference) was found when the first peak in experimental spectrum was assigned to the 243^{rd} isotope in the m/q candidates list.

As mentioned in section 3.1.2 the identification in this experiment was done with the projected spectrum. When the peaks in the projected spectrum were identified the corresponding identification can be assigned back to the individual spectrum for mass evaluation. In this work about 8000 experimental individual spectra were identified in this way. The final identification of all spectra was cross checked and had to be self consistent. This process identifies all peaks unambiguously and quickly. A typical Schottky noise spectrum with the final identification is shown in Fig.3.10.

The identification was carefully checked by taking into account known physical properties since new isotopes and new isomeric states were observed (see details in section 4.2). To make an unambiguous identification the new isotopes were cross checked with all neighboring peaks.

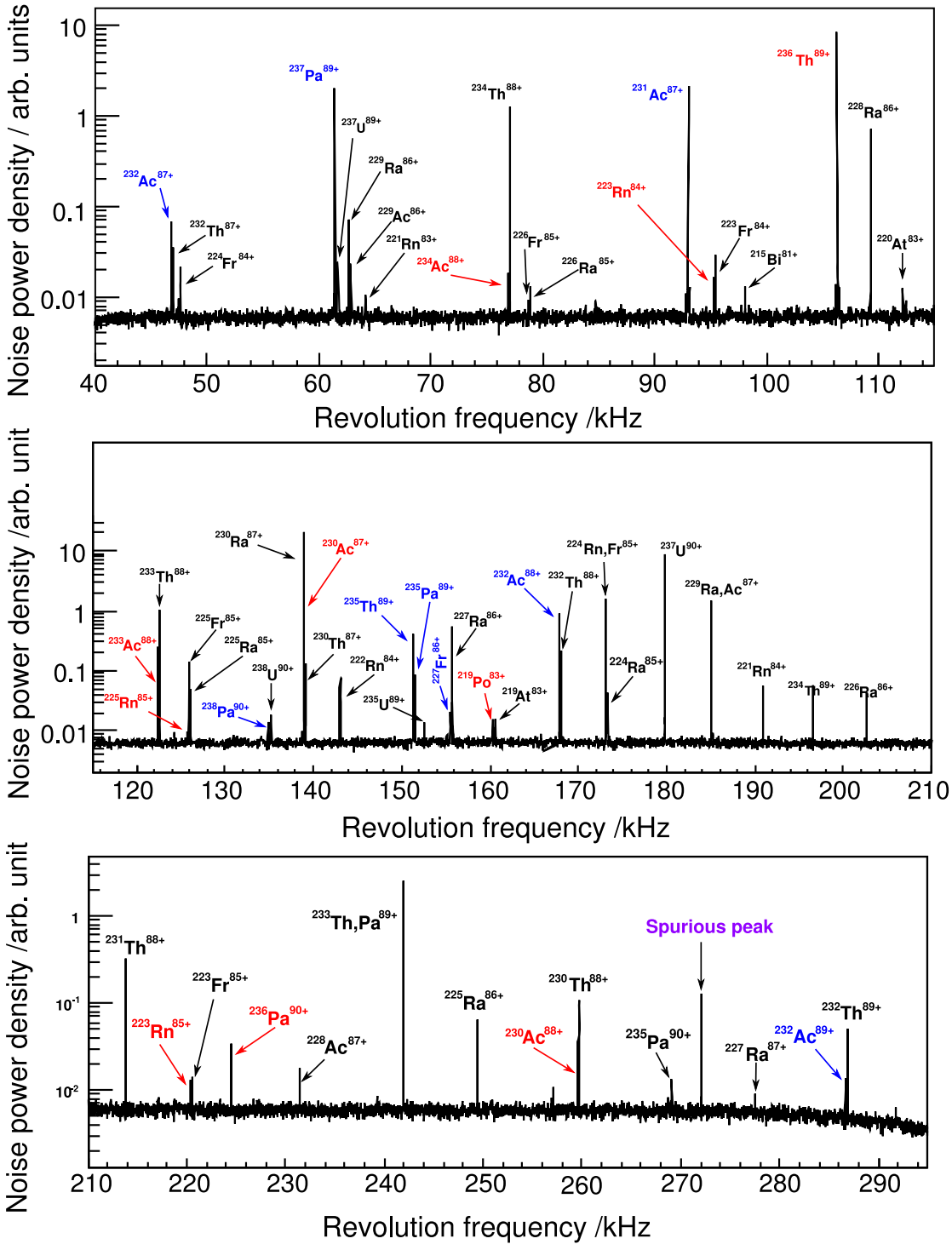

Figure 3.10: A typical frequency spectrum measured under the condition of a cooler voltage of 196 kV and a cooler current of 400 mA. The whole spectrum was divided into three parts. The corresponding identifications of all peaks are marked. The isotopes with known, known with a large uncertainty or unknown mass values are marked with black, blue and red, respectively.

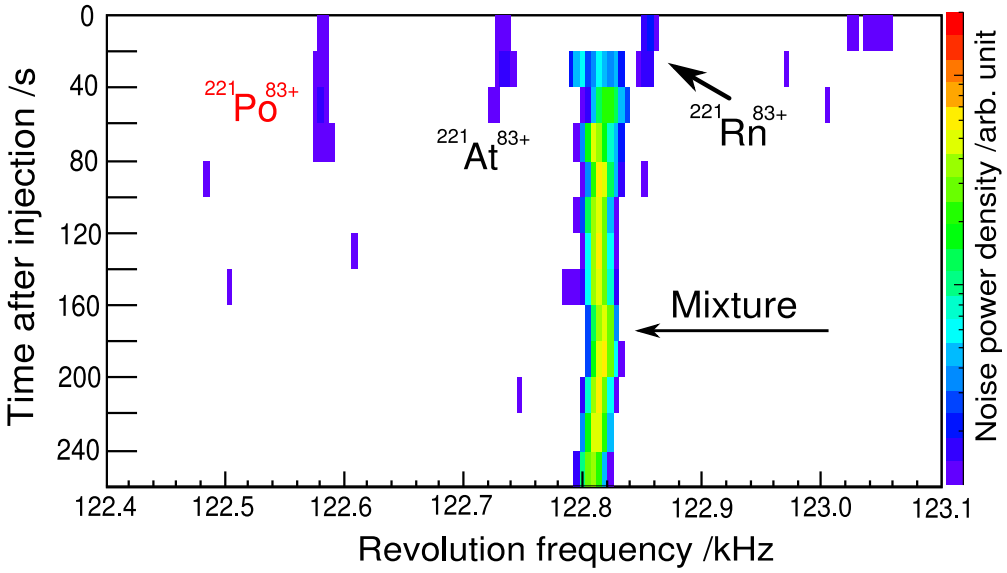

Figure 3.11: Schottky noise spectrum with the new isotope ^{221}Po. The new isotope ^{221}Po was unambiguously identified with the strong support by the identification of the abundant ^{221}At and ^{221}Rn ions.

Fig.3.11 shows the Schottky noise spectrum of the discovered ^{221}Po as an example. The production cross sections of ^{221}At and ^{221}Rn exceed by a factor of 10 to 100 the one for ^{221}Po ions. Therefore, the abundant ^{221}At and ^{221}Rn were analyzed in different spectra and the identification was cross checked several times to support the assignment for ^{221}Po.

New isomers can only be identified after their neighboring peaks were unambiguously identified. Fig.3.12 shows an example of the observed new isomer ^{214m}Bi. The isotopes ^{214}Pb and ^{214}Bi were observed in many other spectra and have been unambiguously identified. The peak between ^{214}Pb and ^{214}Bi was clearly assigned to the new isomeric state of ^{214}Bi.

3.5 Mass evaluation

3.5.1 Momentum compaction factor

Due to the complex variation of the momentum compaction factor α_p as a function of the orbital length of the stored ions in the ESR, each experimental spectrum was divided into several parts which were separately calibrated with a linear function for α_p. The experimental α_p values as a function of the orbital length are shown in Fig.3.13. The experimental α_p value was calculated using formula 2.13 using two peaks which have a frequency difference in the range of 2 kHz – 40 kHz.

3.5.2 Correlation matrix method

The unknown masses and their uncertainties were analyzed with a correlation matrix method[60] which combines all measured spectra into one network calculation. Each

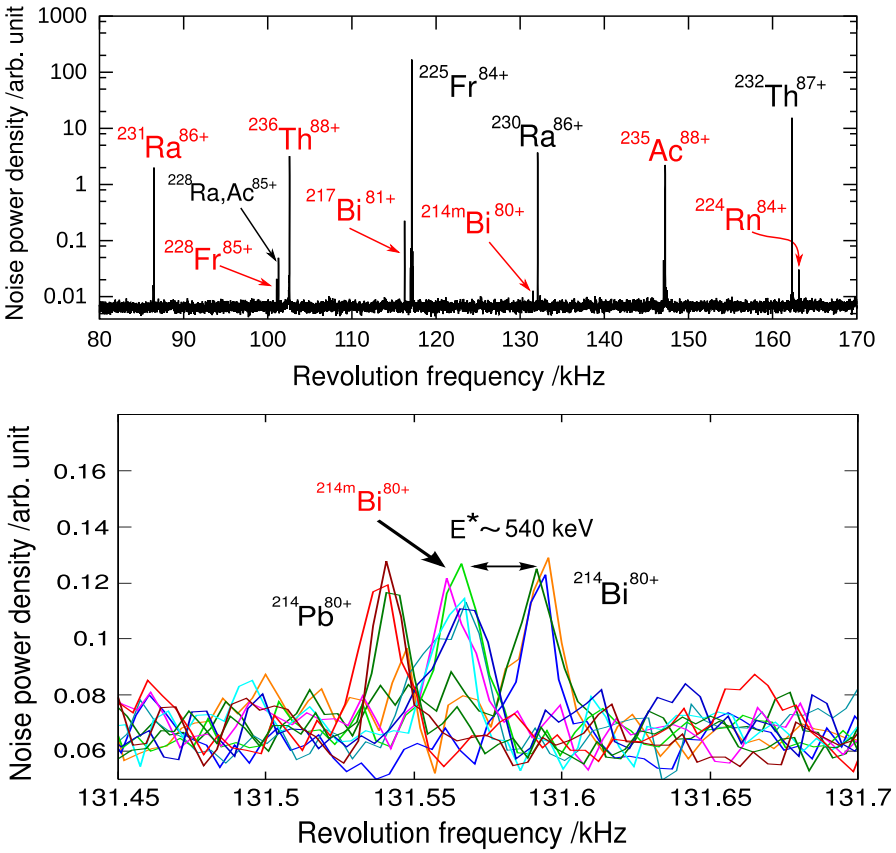

Figure 3.12: Schottky noise spectrum with the new isomer ^{214m}Bi.

spectrum subdivision was indicated by an index j, the frequency of each peak in spectrum j was represented by f_j^μ and μ denoted an ion with a specific mass m_j^μ and a charge q_j^μ. The spectrum j was fitted with a polynomial function with a degree N_p and the coefficients are represented by $a_j^0, \cdots, a_j^{N_p}$. If the ions are measured in different spectra the mass values will be averaged. The deviation of the mass-to-charge ratio from the calibration curve can be written as:

$$\frac{m_j^\mu}{q_j^\mu} - \sum_{k=0}^{N_p} a_j^k (f_j^\mu)^k = l_j^\mu \pm \Delta_j^\mu. \tag{3.1}$$

Deviations l_j^μ should be statistically distributed as a Gaussian function with a mean value equal to zero. The standard deviation Δ_j^μ is a function of the frequency uncertainty $\sigma_{f_j^\mu}$ of the corresponding peak f_j^μ and is defined as:

$$\Delta_j^\mu = \frac{d(\sum_k a_j^k (f_j^\mu)^k)}{d f_j^\mu} \sigma_{f_j^\mu} = \sum_{k=0}^{N_p} k a_j^k (f_j^\mu)^{k-1} \sigma_{f_j^\mu}. \tag{3.2}$$

All subdivisions of the measured spectra are combined via equation (3.1) due to the fact that an isotope can be presented in many different spectra. The reference masses which are used for the spectrum calibration are introduced by the following equation:

$$m_\eta - m_\eta^c = l_\eta \pm \Delta m_\eta, \tag{3.3}$$

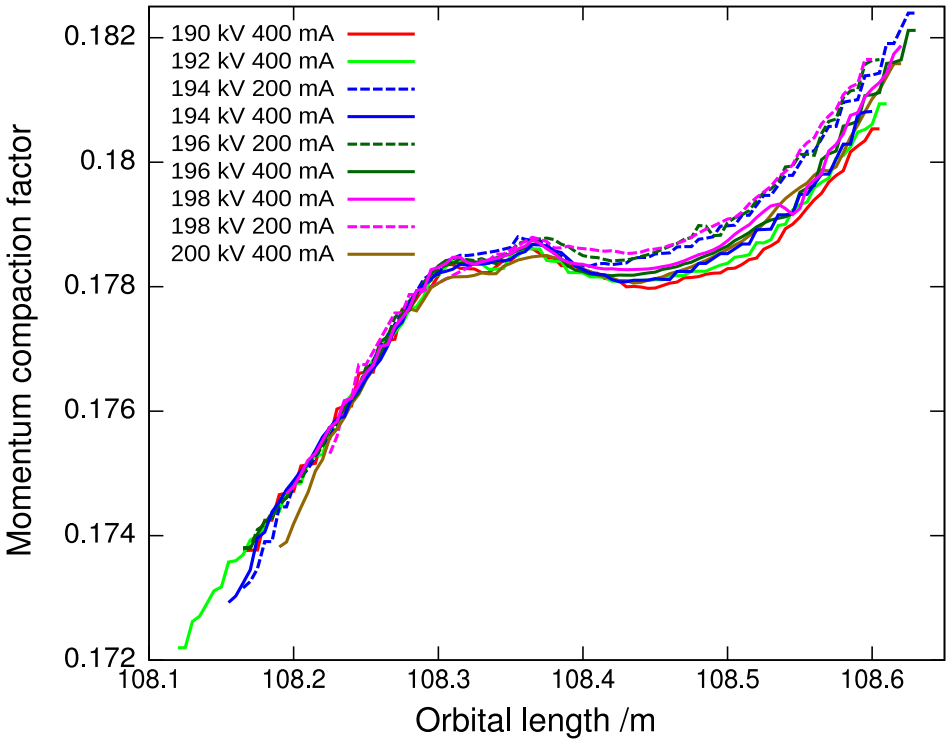

Figure 3.13: The experimental α_p values as a function of the orbital length. The results are plotted for different cooler voltages from 190 kV to 200 kV. The α_p values have slightly changed between the settings. Note, there is a systematical slight increase of the α_p value for the cooler current of 200mA in the region of orbital length greater than 108.4 m.

where l_η is the deviation of the reference mass value (m_η^c) from the mass values (m_η) which is determined in this evaluation. l_η should be statistically a Gaussian distribution with mean value approximately equal to zero and the standard deviation Δm_η is given by the uncertainty of reference masses m_η^c.
The assumed Gaussian distribution allows to estimate the unknown masses and the coefficients of the calibration curves based on the maximum likelihood method. The experimental spectra and reference masses are all independent from each other. The likelihood function can be written as:

$$L = L_c \cdot L_{exp} = \prod_\eta \frac{1}{\sqrt{2\pi}\Delta m_\eta} exp\left(-\frac{l_\eta^2}{2(\Delta m_\eta)^2}\right) \cdot \prod_{j,\mu} \frac{1}{\sqrt{2\pi}\Delta_j^\mu} exp\left(-\frac{(l_j^\mu)^2}{2(\Delta_j^\mu)^2}\right), \quad (3.4)$$

where L_c and L_{exp} denote the calibration part and the experimental part, respectively. The masses and coefficients of the calibration can be found by the partial derivative of the likelihood function:

$$\frac{\partial L}{\partial a_j^k} = 0 \qquad k = 0, \cdots, N_p;\ j = 1, 2, \cdots, N_S, \quad (3.5)$$

$$\frac{\partial L}{\partial m_\mu} = 0 \qquad \mu = 1, 2, \cdots, N_M, \quad (3.6)$$

Where N_p, N_S and N_M are the degrees of the polynomial function, number of spectra and number of measured masses, respectively.

The coefficients of the spectrum j can be found by solving the equation (3.5).

Equation (3.5) can be written as:

$$\sum_\mu \left((1 - \frac{(l_j^\mu)^2}{(\Delta_j^\mu)^2}) k (f_j^\mu)^{k-1} \sigma_{f_j^\mu} + \frac{l_j^\mu}{\Delta_j^\mu} (f_j^\mu)^k \right) = 0. \quad (3.7)$$

The index μ runs through all peaks in spectrum j. Combining (3.7) with equations (3.1) and (3.2) we have:

$$\mathbf{A}_j \begin{pmatrix} a_j^0 \\ a_j^1 \\ \vdots \\ a_j^k \end{pmatrix} = \sum_\mu w_j^\mu \frac{m_j^\mu}{q_j^\mu} \begin{pmatrix} 1 \\ f_j^\mu \\ \vdots \\ (f_j^\mu)^k \end{pmatrix}, \quad (3.8)$$

where

$$w_j^\mu = \frac{1}{(\Delta_j^\mu)^2} = \frac{1}{(\sum_k k a_j^\mu (f_j^\mu)^{k-1} \sigma_{f_j^\mu})^2} \quad (3.9)$$

and

$$\mathbf{A}_j = \begin{pmatrix} \sum_\mu w_j^\mu & \sum_\mu w_j^\mu f_j^\mu & \cdots & \sum_\mu w_j^\mu (f_j^\mu)^k \\ \sum_\mu w_j^\mu f_j^\mu & \sum_\mu w_j^\mu (f_j^\mu)^2 & \cdots & \sum_\mu w_j^\mu (f_j^\mu)^{k+1} \\ \cdots & \cdots & \ddots & \cdots \\ \sum_\mu w_j^\mu (f_j^\mu)^k & \sum_\mu w_j^\mu (f_j^\mu)^{k+1} & \cdots & \sum_\mu w_j^\mu (f_j^\mu)^{2k} \end{pmatrix}. \quad (3.10)$$

The coefficients can be calculated by

$$\begin{pmatrix} a_j^0 \\ a_j^1 \\ \vdots \\ a_j^k \end{pmatrix} = \mathbf{A}_j^{-1} \sum_\mu w_j^\mu \frac{m_j^\mu}{q_j^\mu} \begin{pmatrix} 1 \\ f_j^\mu \\ \vdots \\ (f_j^\mu)^k \end{pmatrix}. \tag{3.11}$$

The matrix $\mathbf{A}_j^{-1}$ is a square matrix with a range equal to the degree of the polynomial fit for the spectrum j.
The masses are obtained by solving equation (3.6):

$$\sum_j w_j^\mu \frac{m_j^\mu}{(q_j^\mu)^2} - \sum_j w_j^\mu \frac{F_j(f_j^\mu)}{q_j^\mu} - \frac{\partial \ln L_c}{\partial m_\mu} = 0, \tag{3.12}$$

index j runs through all spectra in which the mass μ is present and

$$F_j(f_j^\mu) = \sum a_j^k (f_j^\mu)^k = (1, f_j^\mu, \cdots, (f_j^\mu)^k) \begin{pmatrix} a_j^0 \\ a_j^1 \\ \vdots \\ a_j^k \end{pmatrix}. \tag{3.13}$$

The combination of (3.13), (3.11) and (3.12) can produce the final equations for the mass values:

$$\sum_j \frac{m_j^\mu w_j^\mu}{(q_j^\mu)^2} - \sum_{j,\beta} \frac{w_j^\mu}{q_j^\mu} \left[(1, f_j^\beta \cdots, (f_j^\mu)^k \mathbf{A}_j^{-1} \begin{pmatrix} 1 \\ f_j^\beta \\ \vdots \\ (f_j^\beta)^k \end{pmatrix} \frac{w_j^\beta m_j^\beta}{q_j^\beta} \right] - \frac{\partial \ln L_c}{\partial m_\mu} = 0. \tag{3.14}$$

Equation (3.14) can be written in the matrix form:

$$\mathbf{W}\vec{M} = \vec{w}, \tag{3.15}$$

where $\mathbf{W}$ is a $N_{masses} \times N_{masses}$ matrix and its elements have the form

$$W_{\mu\mu} = \sum_j \frac{w_j^\mu}{(q_j^\mu)^2} \left[1 - w_j^\mu (1, f_j^\mu, \cdots, (f_j^\mu)^k) \mathbf{A}_j^{-1} \begin{pmatrix} 1 \\ f_j^\mu \\ \vdots \\ (f_j^\mu)^k \end{pmatrix} \right] + \frac{1}{(\Delta m_\mu)^2}, \tag{3.16}$$

$$W_{\mu\upsilon} = -\sum_j \left[\frac{w_j^\mu w_j^\upsilon}{q_j \mu q_j^\upsilon} (1, f_j^\mu, \cdots, (f_j^\mu)^k) \mathbf{A}_j^{-1} \begin{pmatrix} 1 \\ f_j^\upsilon \\ \vdots \\ (f_j^\upsilon)^k. \end{pmatrix} \right] \qquad \mu \neq \upsilon \tag{3.17}$$

The elements of vector $\vec{w}$ is

$$w_\mu = \frac{m_\mu}{(\Delta m_\mu)^2} + B_\mu. \tag{3.18}$$

The first term is only used if m_μ is a reference mass. The second term is:

$$B_\mu = \sum_{j,\beta} \frac{w_j^\mu w_j^\beta}{q_j^\mu q_j^\beta} (1, f_j^\mu, \cdots, (f_j^\mu)^k) \mathbf{A}_j^{-1} \begin{pmatrix} 1 \\ f_j^\beta \\ \vdots \\ (f_j^\beta)^k \end{pmatrix} E_j^\beta - \sum_j \frac{w_j^\mu E_j^\mu}{(q_j^\mu)^2}, \tag{3.19}$$

where E_j^μ represents the masses of the bound electrons. The equation (3.15) was solved with an iterative procedure. The statistical error of each measured masses was determined by the diagonal elements of the inverse matrix $\mathbf{W}^{-1}$:

$$(\sigma_{m_\mu}^{stat}) = \mathbf{W}_{\mu\mu}^{-1}. \tag{3.20}$$

The systematic error was determined by evaluating the deviation of reference masses to corresponding mass values in the literature. The deviation was determine one by one in such a way that each time the mass of one reference mass was calculated assuming it is unknown. It is obvious that the reference masses used for calibration were carefully selected. In this work only isotopes with a mass uncertainty smaller than 20 keV were used as reference masses.

The systematic error $\sigma_{m_\eta}^{syst}$ was determined with the formula:

$$\sum_\eta \frac{(m_\eta - m_\eta^c)^2}{(\sigma_{m_\eta}^c)^2 + (\sigma_m^{syst})^2 + (\sigma_{m_\eta}^{stat})^2} = N_{references}, \tag{3.21}$$

where $N_{references}$ is the number of reference masses and m_η and m_η^c are the determined reference mass values and the corresponding literature values, respectively. $\sigma_{m_\eta}^c$ and $\sigma_{m_\eta}^{stat}$ are the mass uncertainties of the reference masses from the literature and the corresponding statistical error in this analysis, respectively.

3.5.3 Local mass evaluation

The projected spectrum contains all peaks of one setting and all the known and unknown masses. The unknown mass can be fitted in a rather small frequency range if reference masses are available near the unknown mass. The α_p values in such a small range changed only very weakly and therefore, the polynomial fit with a degree up to two was precise enough. Mostly a linear fit was sufficient. With the local fitting method very high mass resolution can be achieved if well-known references are available close to the unknown masses.

The mass determination using the local evaluation method was performed in addition to the matrix method. Both results are in good agreement. Fig.3.14 demonstrates an ideal case of unknown mass determination from reference masses. Only a small band of the frequency spectrum is plotted in Fig.3.14 (the total band width of the frequency spectrum is 312500 Hz). The frequency spectrum was measured with a cooler voltage of 194 keV and a cooler current of 400 mA. Note, the upper right panel is an histogram of the measured revolution frequency. The results were plotted in the bottom panel to show the mass difference between this work and AME2003 data. The well known mass

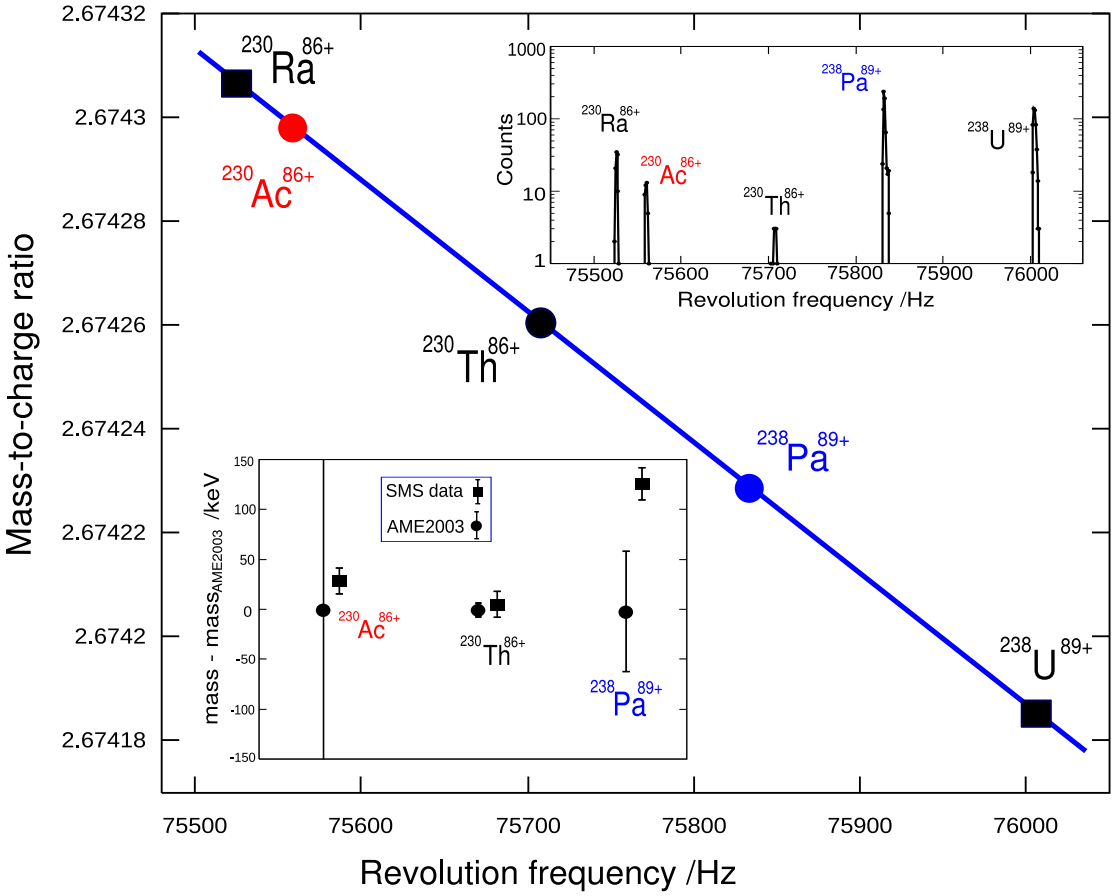

Figure 3.14: Example of a mass determination with the local-mass evaluation method. The mass of ^{230}Ac was unknown before this work. The calibration with a first order polynomial is sufficient for this small range of revolution frequencies. The masses of ^{230}Ra and ^{238}U are used as reference masses for spectrum calibration.

^{230}Th (mass uncertainty 1.8 keV) demonstrates the agreement between this work and the AME2003 data.

The systematic error in this method was determined by the deviation of the analyzed known masses values from the AME2003 data. Fig.3.15 shows the distribution of the deviations for 35 known masses. A systematic error of 30 keV was achieved.

3.6 Lifetime evaluation

The lifetime analysis can be done with two different methods. The first one is to analysis the Schottky peak area in the frequency spectrum as discussed in section 2.7. This method can only be applied to isotopes which have a large abundance in the spectrum. The half-life of ^{234}Ac was evaluated in this way. The Schottky peak area of ^{234}Ac from different injections was summed and fitted for the determination of the half-life. Fig.3.16 shows the results.

The ring losses due to atomic interactions were carefully considered in the final result. The ring losses can be estimated by fitting the decay curve of those nuclei with half-lives much longer than the measuring time. In this experiment the isotope ^{223}Rn

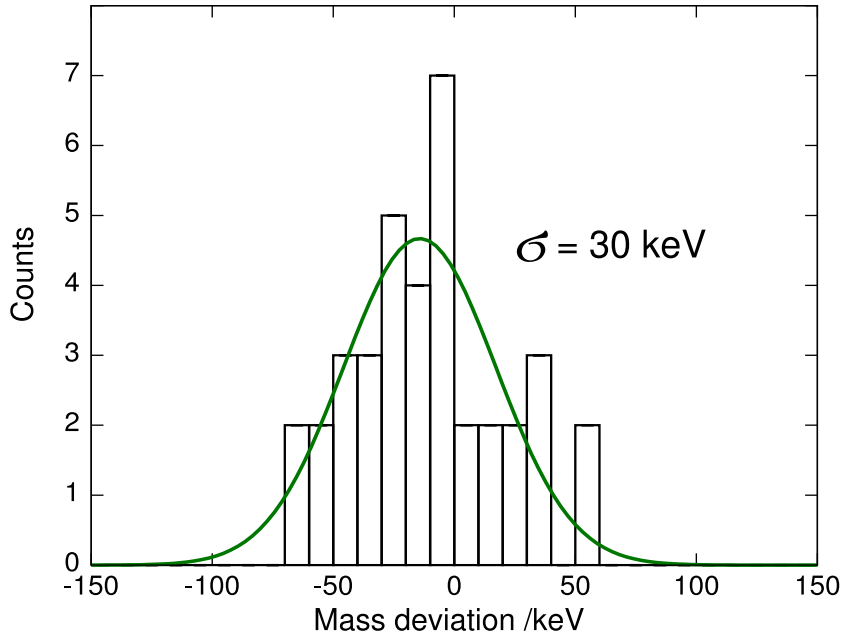

Figure 3.15: Mass evaluation for known masses. The present experimental values are compared to the known values from the literature. The fitted mean value is 14 keV with a standard deviation 30 keV.

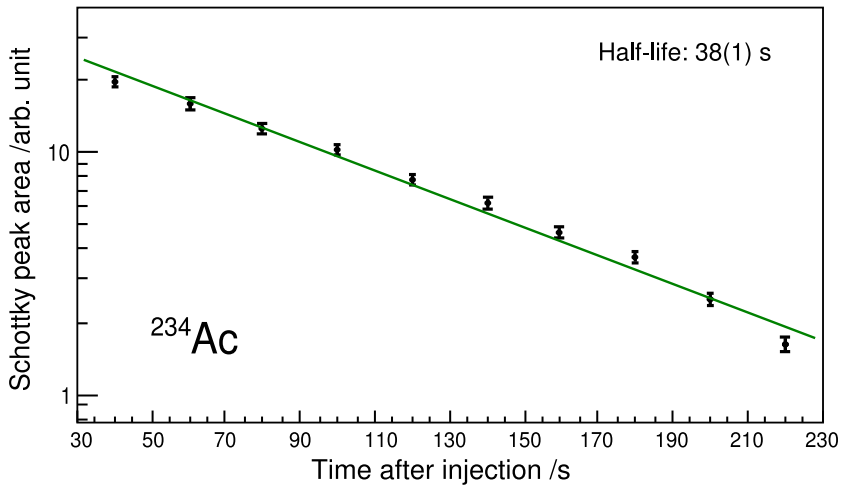

Figure 3.16: Half-life determination of ^{234}Ac from the evolution of the Schottky peak areas.

was selected for the determination of ring losses. The half-life of ^{223}Rn is 24.3(0.4) minutes according to NUBASE2003[39].

In case of very exotic nuclei which were injected as single ions only the single-ion tracing method was applied. In this method the decay time of the stored ion is determined by the trace in the waterfall diagram. The results for single ions are summed after. A special case is the estimation of the half-life for those exotic nuclei which are observed only a few times or even once in the experiment. An estimation of the half-life for those exotic nuclei was performed using the method in reference [66].

Chapter 4

Results

4.1 The covered region of nuclides in this experiment

Exotic nuclei were studied in the neutron-rich region of the element range from iridium to uranium in this experiment. The identified nuclides are shown in Fig.4.1. Besides projectile fragmentation, charge-exchange of relativistic uranium also contribute to the produced nuclei. The isotope ^{238}Pa was produced by pure charge-exchange reaction of relativistic ^{238}U ions in the ^{9}Be target. In addition to charge-exchange reactions, also proton removal happened in the production of isotopes ^{237}Th and ^{236}Ac.

Remarkable improvements for nuclear masses and lifetimes have been achieved by this experiment. For example, the masses of the last six known neutron-rich Rn isotopes were measured for the first time. In total there are 30 known isotopes in the Ir – U range for which masses are measured for the first time. Five new isotopes in the neutron-rich region (^{236}Ac, ^{224}At, ^{222}Po, ^{221}Po, ^{213}Tl) were discovered in addition. Besides the ground state masses, 16 isomeric states were observed including six new isomeric states (^{234m}Ac, ^{234n}Ac, ^{228m}Ac, ^{228m}Fr, ^{214m}Bi, ^{213m}Bi). The half-lives and excitation energies of the discovered isomeric states were analyzed with the time-resolved Schottky Mass Spectrometry. In total 195 nuclides were identified in this work including 5 discovered isotopes and 6 discovered isomers.

4.2 The discovery of 5 new isotopes

Exploring the limits of nuclear existence is one of the driving forces in nuclear science[67]. The production and identification of new isotopes is always interesting and challenging because it may lead to the discovery of new physics.

The sensitivity of SMS down to single ions has provided a large discovery potential for exotic nuclei with very small production cross sections. The exotic nuclei can be unambiguously identified even in case only single ion was stored in the ESR once in a experiment. The revolution frequency can be precisely measured if the ions were stored in the ring longer than about 20 s.

The discovered new isotopes in this work are listed in table 4.1. The one- and two-neutron separation energies are determined from our measured masses in this experi-

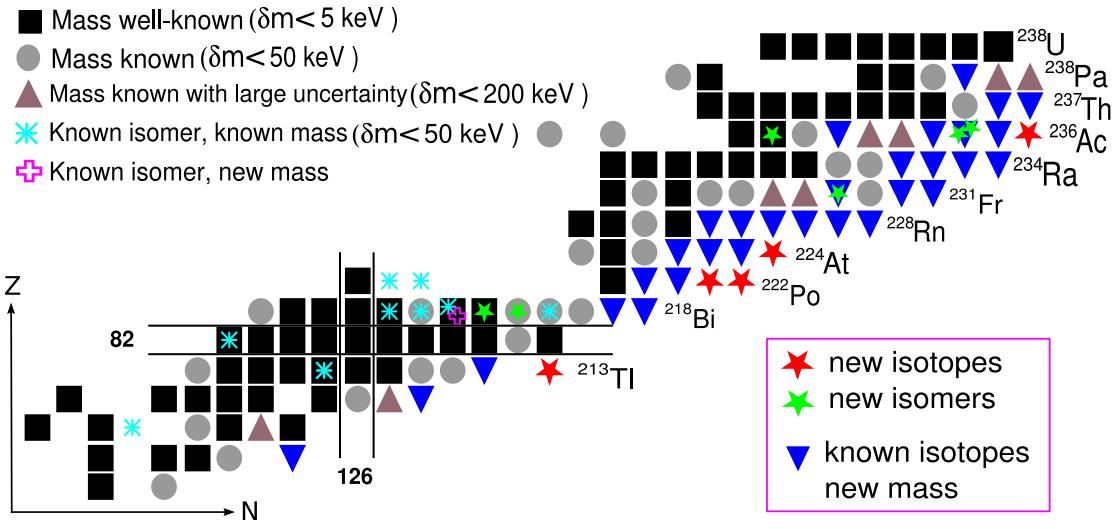

Figure 4.1: Nuclides measured in this experiment in the element range of Ir – U. The information for known masses are taken from the compilation AME2003.

ment.

The isotope ^{236}Ac was discovered as a single ion stored in the ESR for about 100 seconds. Fig.4.2 shows the 1-dimensional and 2-dimensional presentation of the Schottky noise spectrum with the identified ^{236}Ac. The isotope ^{236}Ac was produced by a rather complicated mechanism as discussed in section 2.1.3. Three protons were removed and one neutron was picked up via relativistic nucleon-nucleon collision. The one- and two-neutron separation energies, as determined from our measured masses, for ^{236}Ac are 4.21 MeV and 9.73 MeV, respectively. The half-life of ^{236}Ac was estimated from the measured storage time in the ESR.

The discovered isotope ^{224}At was observed as a single ion in 3 injections. Fig.4.3 shows the Schottky noise spectrum from one of the injections presenting the new isotope ^{224}At. The upper panel of Fig.4.3 shows the measured 1-dimensional Schottky noise spectrum demonstrating the unambiguous identification of ^{224}At. Note, that the frequency lines of ^{232}Ra, ^{232}Th, ^{224}At and ^{224}Rn ions represent single ions stored in the ESR. The half-life of ^{224}At was extracted from the 2-dimensional time-resolved Schottky noise spectrum which displayed in the low panel of Fig.4.3. The one- and two-neutron separation energies of ^{224}At are 3.82 MeV and 9.36 MeV, respectively.

Isotope	Mass excess (keV)	S_n (MeV)	S_{2n} (MeV)
^{236}Ac	51251 (30)	4.21	9.73
^{224}At	27699 (29)	3.82	9.36
^{222}Po	22483 (29)	5.40	8.95
^{221}Po	19815 (28)	3.55	8.99
^{213}Tl	1667 (32)	–	8.40

Table 4.1: Measured mass-excess values and the the corresponding one- and two-neutron separation energies of the discovered isotopes.

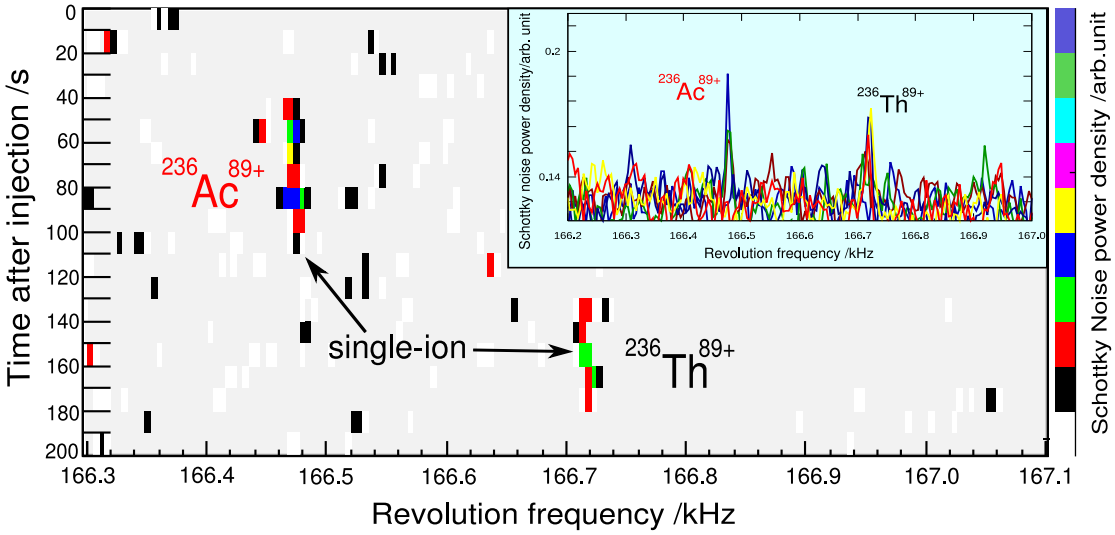

Figure 4.2: The 1-dimensional and 2-dimensional Schottky noise spectrum where the new isotope ^{236}Ac was identified. ^{236}Ac circulated for about 100 seconds in the ESR.

Two new polonium isotopes, ^{221}Po and ^{222}Po, were observed in this experiment. ^{221}Po was observed in several injections while ^{222}Po was observed in one injection only. Fig.4.4 shows the Schottky noise spectrum with the frequency line of ^{222}Po. The two-neutron separation energies of ^{221}Po and ^{222}Po are 8.99 MeV and 8.95 MeV, respectively. The mass values of ^{222}Rn^{84+} and ^{222}Fr^{84+} have a difference about 40 keV corresponding to 2 Hz frequency difference. Therefore only a mixtures can be observed as shown in Fig.4.4. In Fig.4.4 the new isotope ^{222}Po is recorded in injection A while in injection B ^{222}At was observed in a frequency position very close to ^{222}Po. The 1-dimensional frequency lines of injection A and B are shown in the lower panel of Fig.4.4. The excellent frequency resolution of ^{222}Po and ^{222}At can be clearly seen.

Fig.4.5 shows the measured frequency spectrum with the new isotope ^{213}Tl. The two-neutron separation energy of ^{213}Tl is 8.4 MeV which was deduced from our experimental masses. The isotopes ^{213}Tl, ^{213m}Bi and ^{213}Bi in Fig.4.5 are all observed as stored single ions.

4.3 The first observation of 6 isomers

The high resolving power up to $2 \cdot 10^6$ of Schottky Mass Spectrometry allows to separate the isomeric states from their ground states. The duration of the electron cooling time limits the observation to long-lived ($\geq$ a few s) isomeric states only. The nuclear isomeric states can be unambiguously identified by their frequency difference to the corresponding ground states.

In case the excitation energies of isomeric states are large enough ($\geq$ 1 MeV) the revolution frequencies of both ground state and isomeric state can be measured precisely at the same time. For isomers with low excitation energy ($\approx$ hundred keV) *Single-ion Spectroscopy* has to be applied. In this method the revolution frequencies of the isomeric states and the ground states are obtained from those spectra where only a single ion is recorded. In this case either the isomeric state or the ground state can be pop-

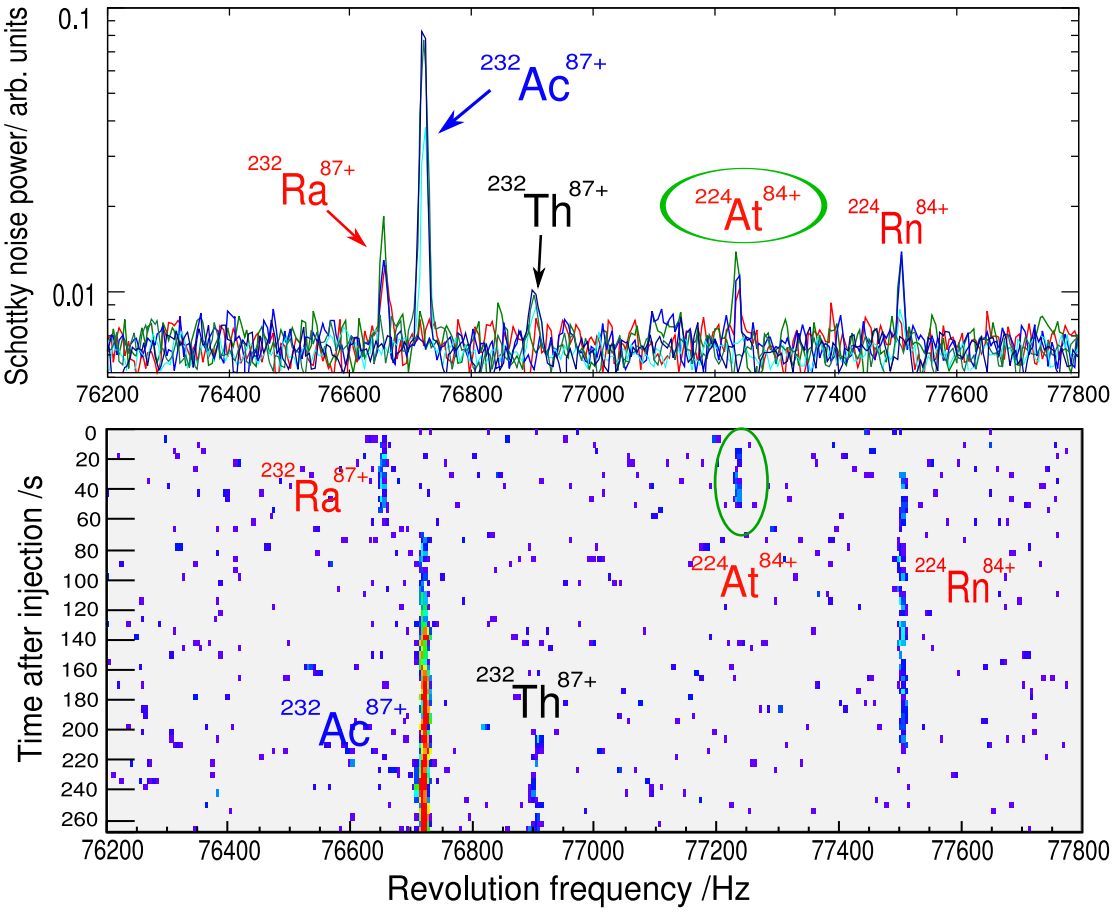

Figure 4.3: Schottky noise spectrum with the new isotope ^{224}At. ^{224}At was observed for about 50 s in the ESR in this injection.

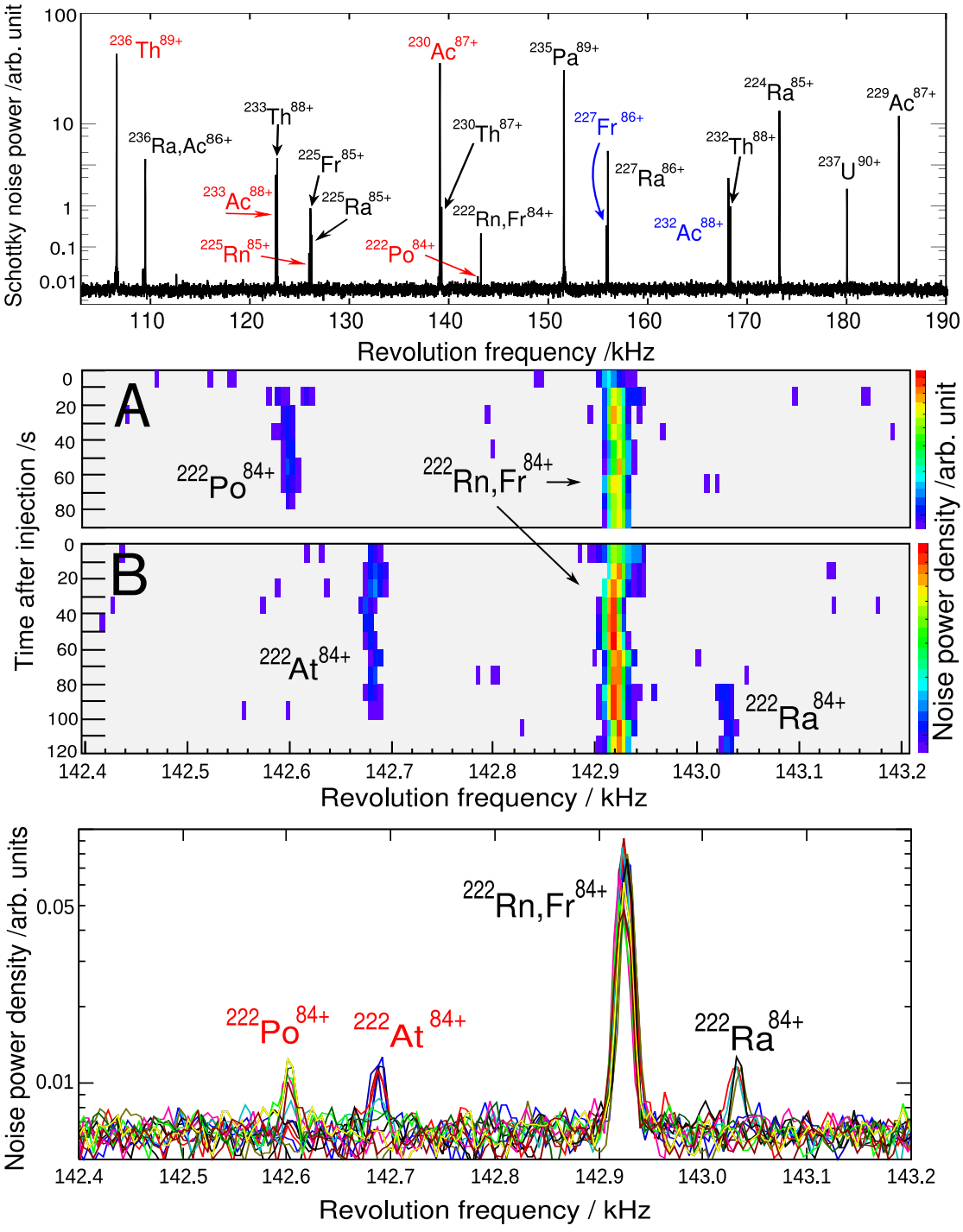

Figure 4.4: Schottky noise spectrum where the new isotope ^{222}Po is observed in the injection A (middle). Schottky noise signals from two injections A and B are displayed in the bottom panel to show the clear frequency difference between ^{222}Po and ^{222}At. Note, the ^{222}Po, ^{222}At and ^{222}Ra frequency lines result all from single ions stored in the ESR.

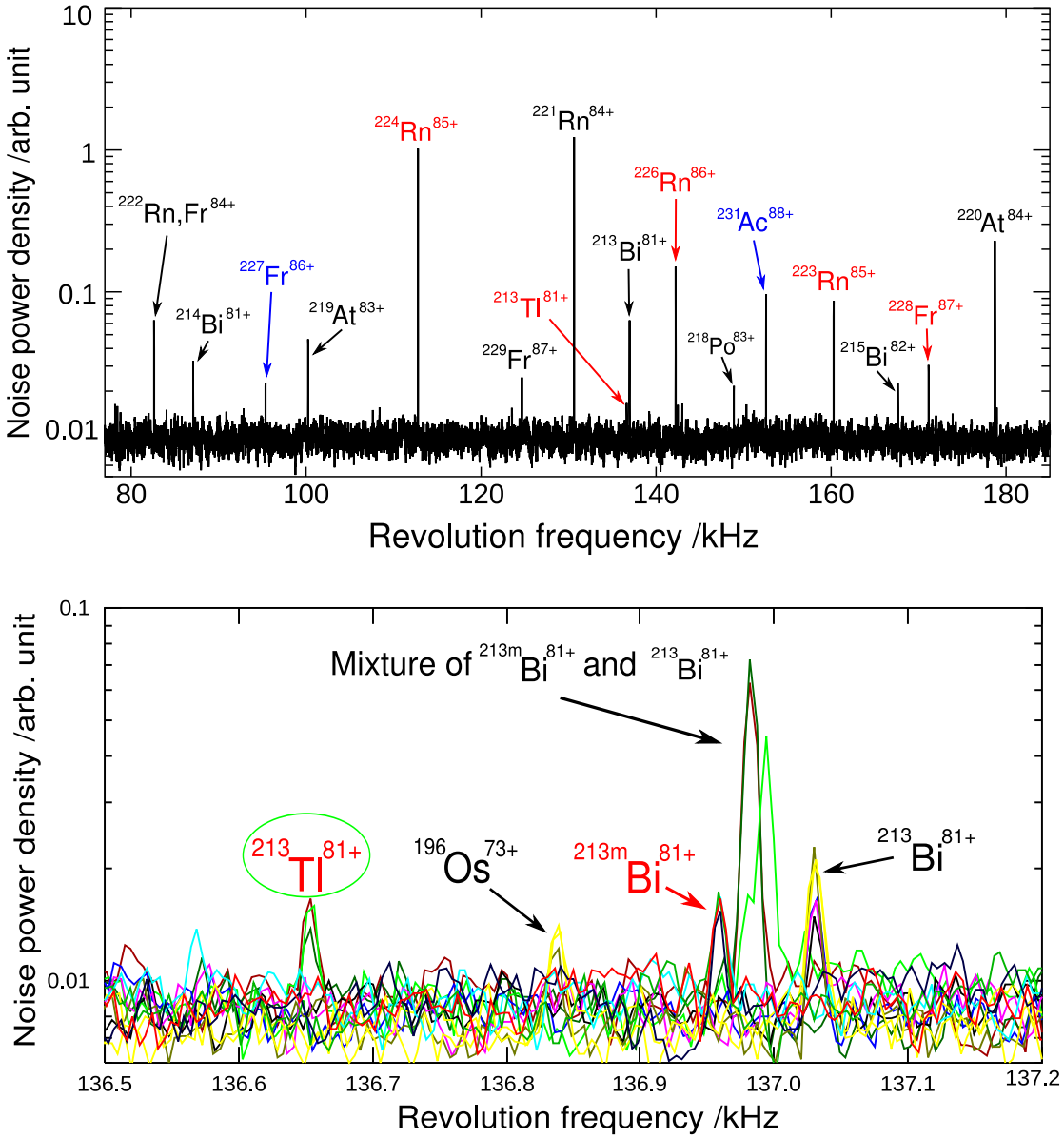

Figure 4.5: Schottky noise spectrum for the identification of the new isotope ^{213}Tl. The strong q^2 dependence of the signal power can be seen.

Isomer	Excitation energy (keV)
^{234m}Ac	140 (30)
^{234n}Ac	620 (30)
^{228m}Ac	356 (30)
^{228m}Fr	1004 (30)
^{214m}Bi	539 (30)
^{213m}Bi	1319 (30)

Table 4.2: Measured excitation energies of the discovered isomers.

ulated. So that the frequencies of both can be measured without any mixture. The *Single-ion Spectroscopy* allows the measurements of isomeric states with a low population rate and a low excitation energy using time-resolved SMS.

The discovered 6 isomeric states are listed in table 4.2. The excitation energies are deduced by the mass difference of the isomeric states and corresponding ground states.

Two long-lived isomeric states of ^{234}Ac have been discovered in this experiment. Fig.4.6 shows the Schottky noise signal of the first isomeric state ^{234m}Ac. The determined excitation energy of ^{234m}Ac is about 140 keV which corresponds to only 7 Hz difference in revolution frequency. In Fig.4.6 the ^{234m}Ac was observed in the injection A (middle panel). The lower panel shows the projected spectrum from the setting with ^{234m}Ac. The small peak close to the peak of ^{234g}Ac in the projected spectrum was assigned to ^{234m}Ac. Fig.4.7 shows the Schottky noise spectrum of the second isomeric state ^{234n}Ac. The isomeric state ^{234n}Ac has an excitation energy about 620 keV corresponding to about 30 Hz difference in the frequency spectrum. Both new isomeric states have such a small excitation energy that the isomeric states can not be separated from the ground state if both are stored in the ring. Two injections are shown in the upper part of Fig.4.7 where both the ion in the ground and isomeric state were recorded. Only the mixtures can be observed in the beginning of the injection and after some time if one of the ions was lost due to decay then the pure isomeric state (A) or ground state (B) can be observed. The small but clear frequency difference of ground state and isomeric state can be clearly seen in the lower panel of Fig.4.7 where frequency peaks from the injections A and B are displayed.

The calculated energy level of ^{234}Ac with the shell model[68, 69] was shown in Fig.4.8. The experimental excitation energy of the observed new isomers are compared in Fig.4.8.

Fig.4.9 shows the Schottky noise spectrum with the new isomeric state ^{213m}Bi unambiguously identified in the upper panel. The lower panel in Fig.4.9 shows a decay event from ^{213m}Bi to ^{213}Bi. The excitation energy of the new isomeric state ^{213m}Bi is 1319$\pm$30 keV.

The new isomeric state ^{228m}Ac can be unambiguously identified in Fig.4.10. The pure isomeric state was observed in one injection which is displayed in the upper panel of Fig.4.10. The 356 keV excitation energy (corresponding to about 18 Hz difference in the frequency domain) is not large enough to separate the isomeric state and ground

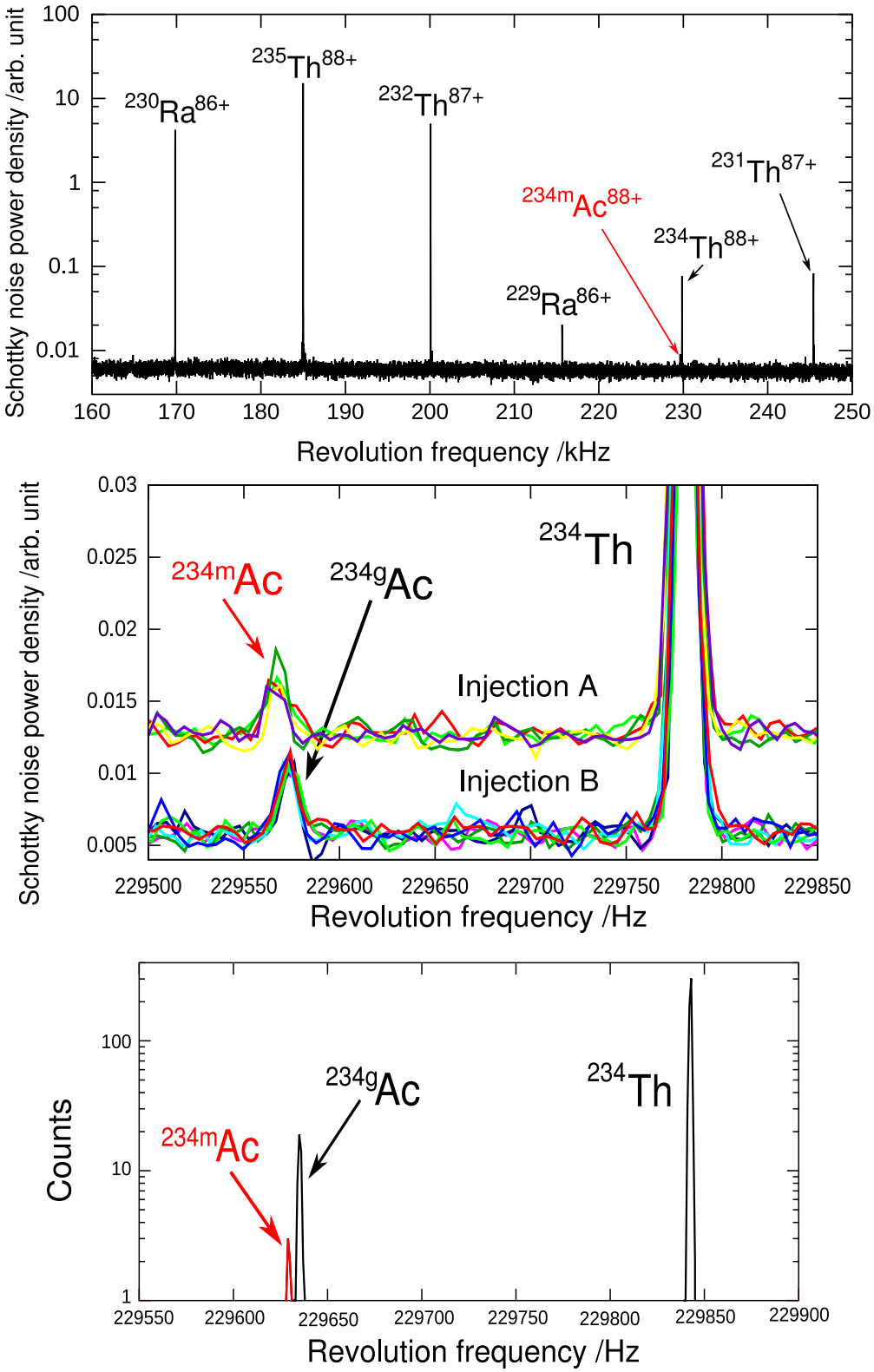

Figure 4.6: Schottky noise spectrum with the new isomer ^{234m}Ac. The Schottky noise signal from two injections, A and B, are displayed in the middle panel. The isomeric state ^{234m}Ac was observed in the injection A. The excitation energy is about 140 keV and corresponds to a frequency difference of about 7 Hz. The projected spectrum shown in the lower panel clearly displays the peak of the isomeric state.

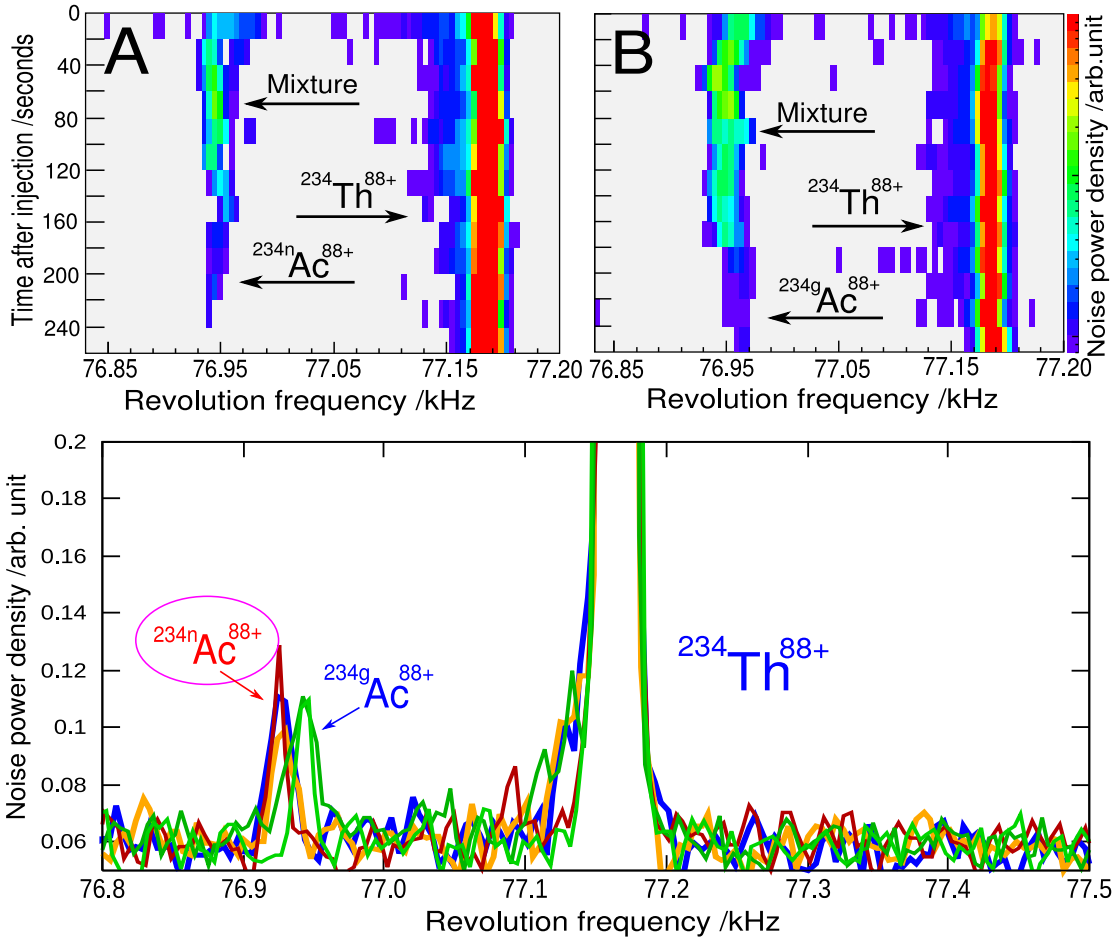

Figure 4.7: Schottky noise spectrum with the new isomer ^{234n}Ac. The ground and isomeric state are mixed at the beginning of both injections, A and B. The pure isomeric state was observed only after 160 s in the injection A after the ion in the ground state was lost in the ring. The separation of the ground and isomeric states in the frequency spectrum is clearly shown in the lower panel.

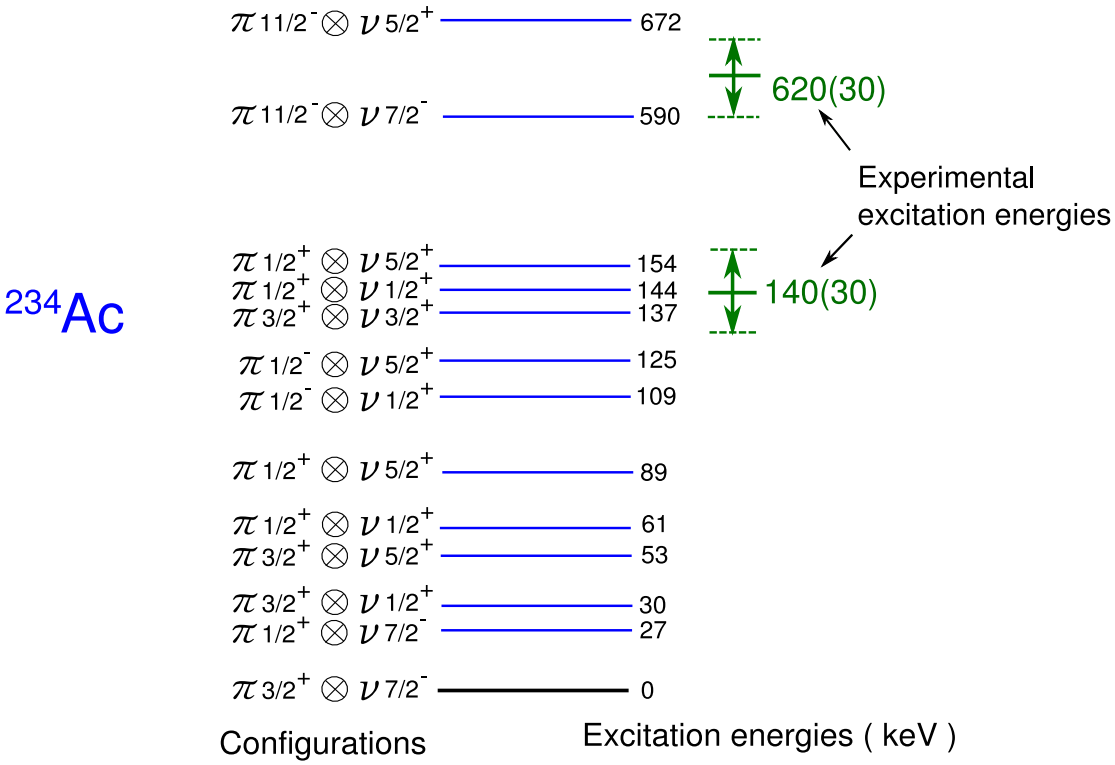

Figure 4.8: Calculated energy levels of ^{234}Ac nuclei. The possible excitation energies of the new isomers are also displayed.

state when both ions are present in the ring.

The Schottky noise spectrum where the new isomer ^{228m}Fr was identified is shown in Fig.4.11. The peak between the peak of ^{228}Rn and ^{228}Fr can only be identified as a new isomeric state of ^{228}Fr. The excitation energy of ^{228m}Fr is about 1 MeV.

Besides the six identified new isomers, there are other isotopes predicted with long-lived isomeric states probably included in the mixed signals,i.e., the isomeric states are not directly observed. Fig.4.12 and Fig.4.13 show two examples of those cases. In Fig.4.12 the pure ground state of ^{236}Pa was observed after the ion in the isomeric state was lost. The sudden decrease of the intensity and the slight frequency shift suggested that there could be a long-lived isomeric state existing during the first 120 seconds after injection. In Fig.4.13 the peak of ^{232}Ac is much wider than the peak of ^{232}Th which means that there was very likely an isomeric state mixed in. There are reasons which could explain the none direct observation of ^{236m}Pa and ^{232m}Ac. The excitation energy is very small such that the isomeric states can not be separated from their ground states in the ring. The production cross section of ^{232}Ac and ^{236}Pa are very large thus the single-ion spectrometry can not be applied. Nevertheless, the broad distribution of the mixture already shows that possible isomeric states lived longer than the electron cooling time.

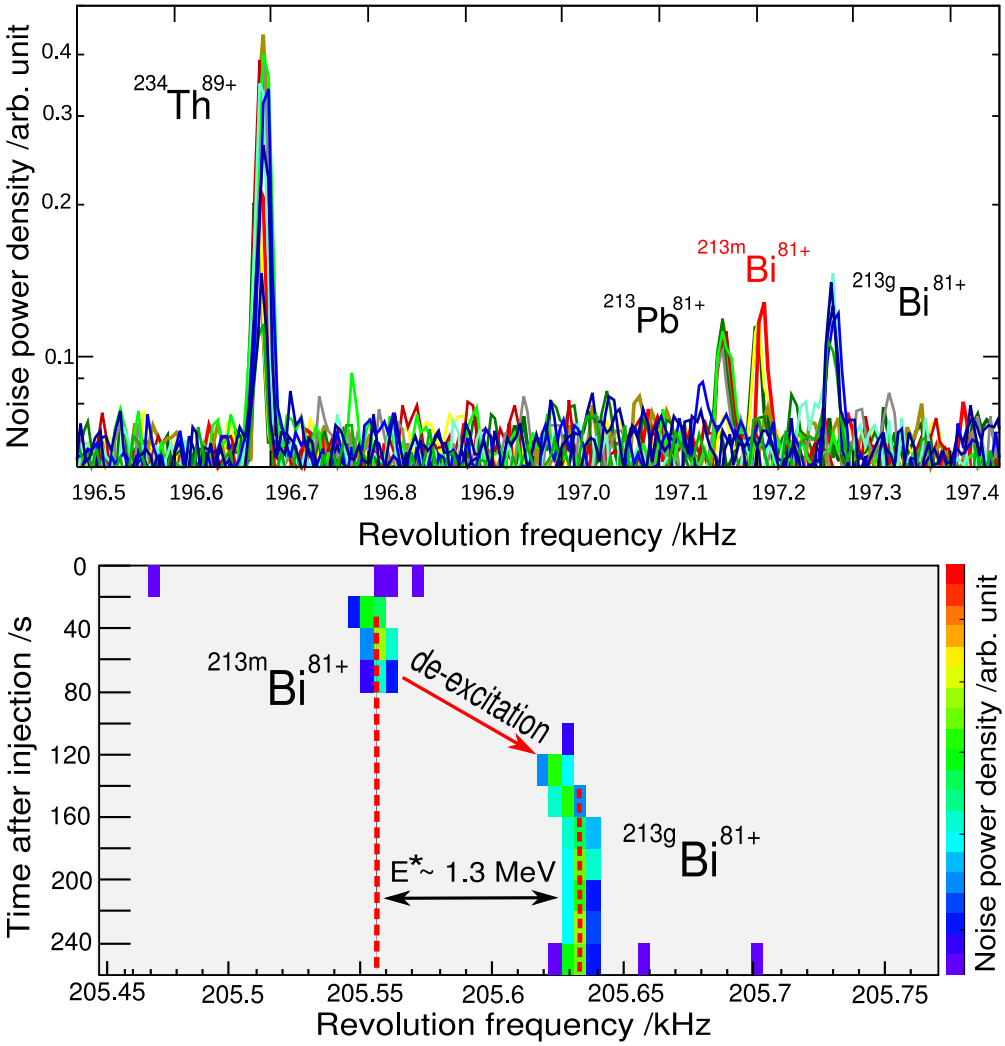

Figure 4.9: Schottky noise spectrum with the observed new isomeric state ^{213m}Bi. A decay event from ^{213m}Bi to ^{213}Bi was observed in the single-particle spectrum (lower panel).

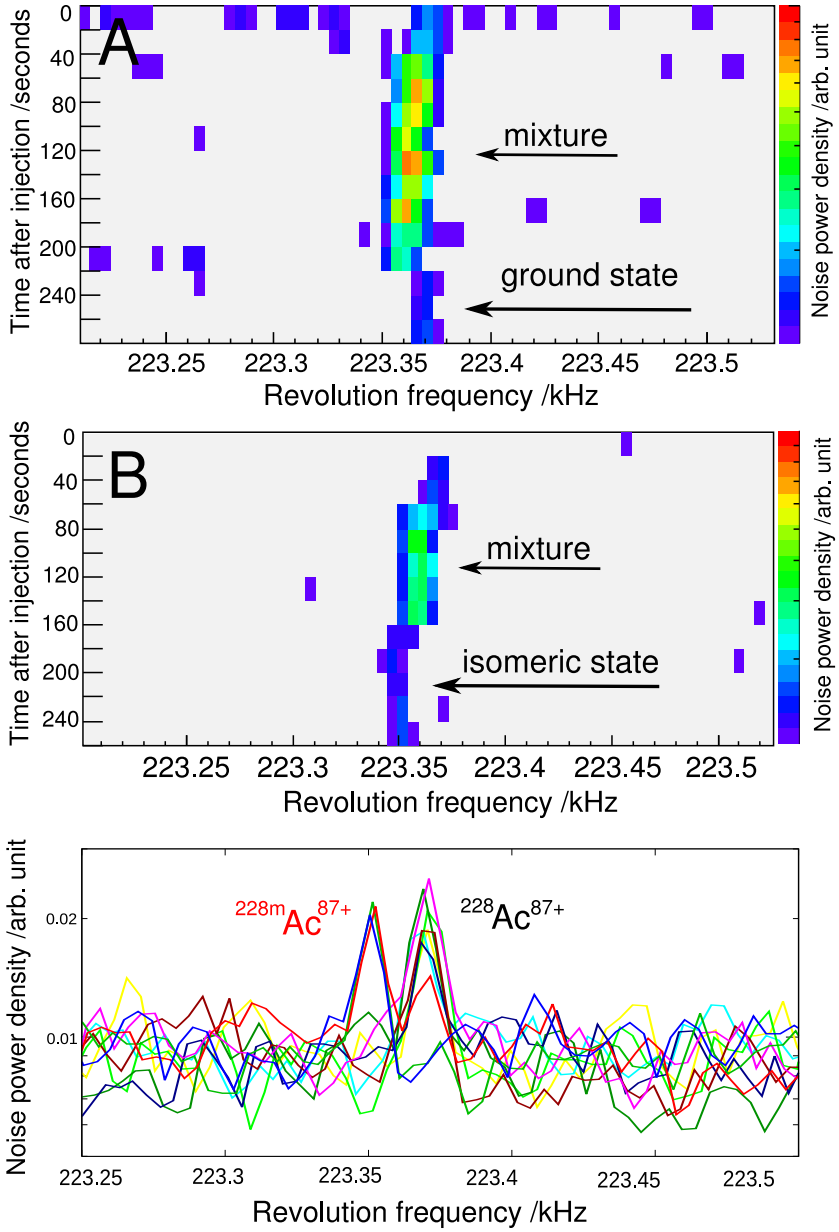

Figure 4.10: Schottky noise spectra documenting the observed new isomeric state ^{228m}Ac.

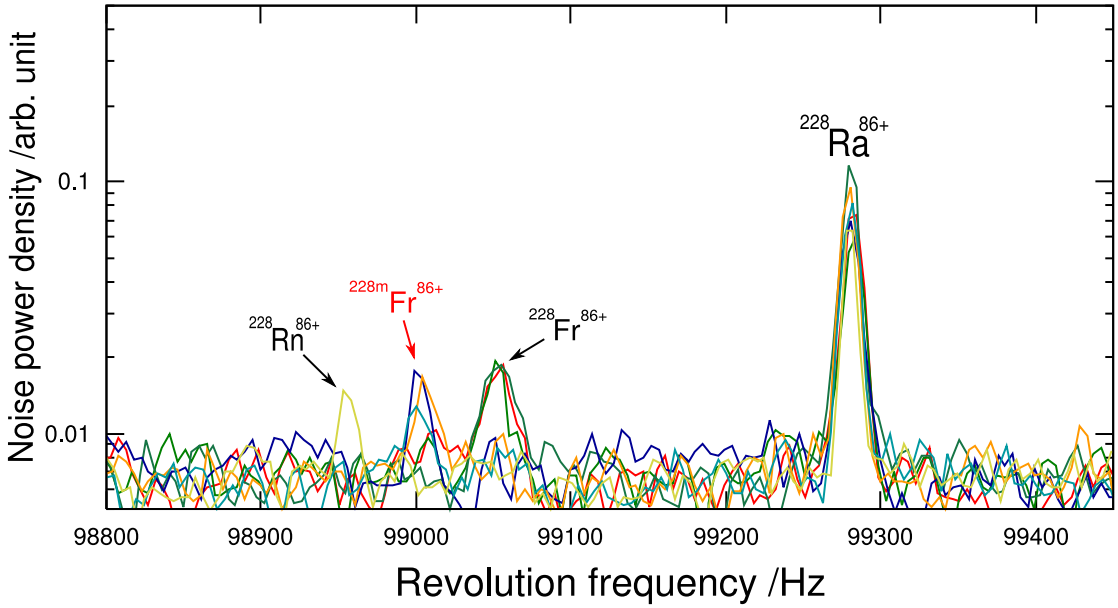

Figure 4.11: The Schottky noise spectrum for the identification of the new isomeric state ^{228m}Fr.

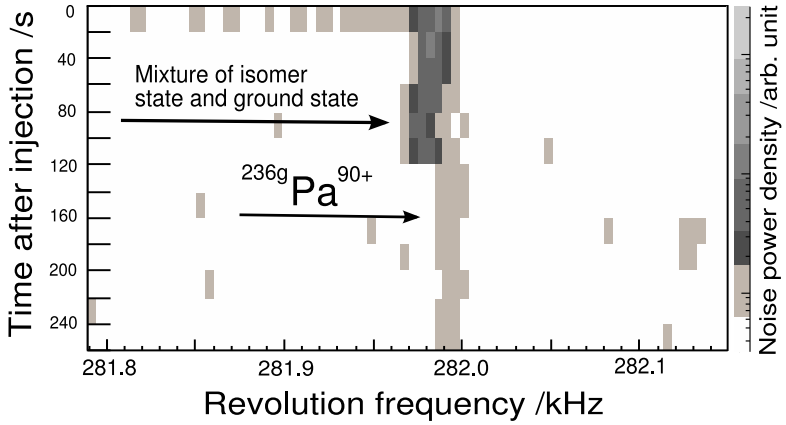

Figure 4.12: Measured Schottky noise spectrum revealing the existence of a long-lived isomeric state of ^{236}Pa.

4.4 New masses in the neutron-rich region of Pt – Pa

Experimental data of masses for neutron-rich isotopes above lead are still rare. For example, the masses of the 6 most neutron-rich isotopes of Rn (^{223}Rn – ^{228}Rn) have been measured for the first time in this experiment.

In the heavy neutron-rich region 41 new masses (including new isotopes and new isomers) were measured for the first time in this work. The measured new masses of known isotopes are listed in table 4.3. The new masses are located in the Pt – Pa region. The knowledge of mass in this region has been significantly improved by this experiment. 16 masses with a large uncertainty from previous experiments are remeasured in this work and are listed in table 4.4.

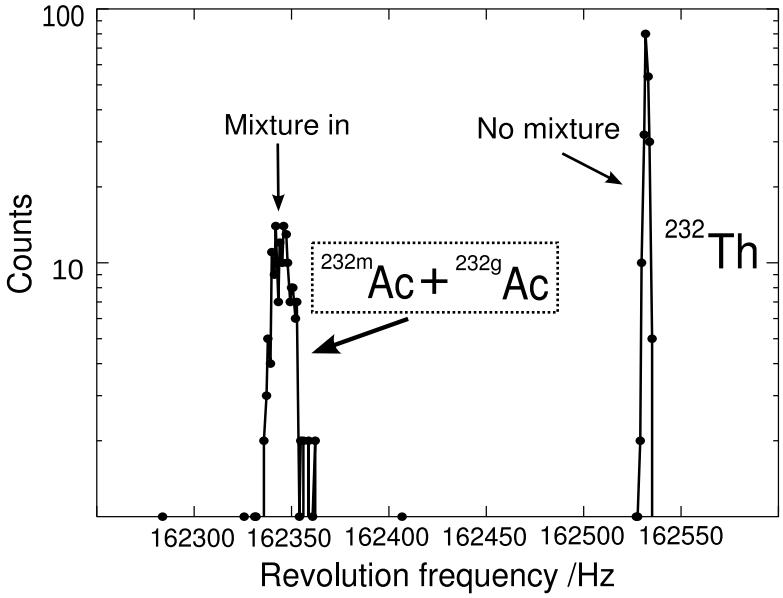

Figure 4.13: Histogram of the measured revolution frequencies of ^{232}Ac and ^{232}Th recorded in one setting. The mixture is a hint for the existence of a long-lived isomeric state of ^{232}Ac.

4.5 The one- and two-nucleon separation energies

The systematic measurement of one- and two-nucleon separation energy allows to study the fine structure of the mass surface and extract nuclear structure information such as shell closures or deformations. The position of drip-lines and the probability for a certain decay mode can be determined by the nucleon separation energies. The one-neutron and one-proton separation energy is defined by:

$$S_n(N,Z) = B(N,Z) - B(N-1,Z), \tag{4.1}$$

$$S_p(N,Z) = B(N,Z) - B(N,Z-1), \tag{4.2}$$

where $B(N,Z)$ is the total binding energy of a nuclide with N neutrons and Z protons. Fig.4.14 shows the one-neutron separation energy of elements in the range Bi – Pa. The pairing effects are shown in Fig.4.14. The S_n values are still quite large which means the neutron drip-line in this region is located far away from the present experimental data. The one-proton separation energy is shown in Fig.4.15. The data measured for the first time are shown in red color in Fig.4.14 and Fig.4.15.

Due to the pairing effects the single-nucleon separation energy can not easily illustrate nuclear structure effects. Shell closure and deformation can be directly detected by studying the systematic trend of the two-nucleon separation energy. The two nucleon separation energies are defined by:

$$S_{2n}(N,Z) = B(N,Z) - B(N-2,Z), \tag{4.3}$$

$$S_{2p}(N,Z) = B(N,Z) - B(N,Z-2). \tag{4.4}$$

The two-neutron separation energies in the element range from Os to Pa are shown in Fig.4.16. The N=126 shell closure is represented by a sharp drop of the S_{2n} energies.

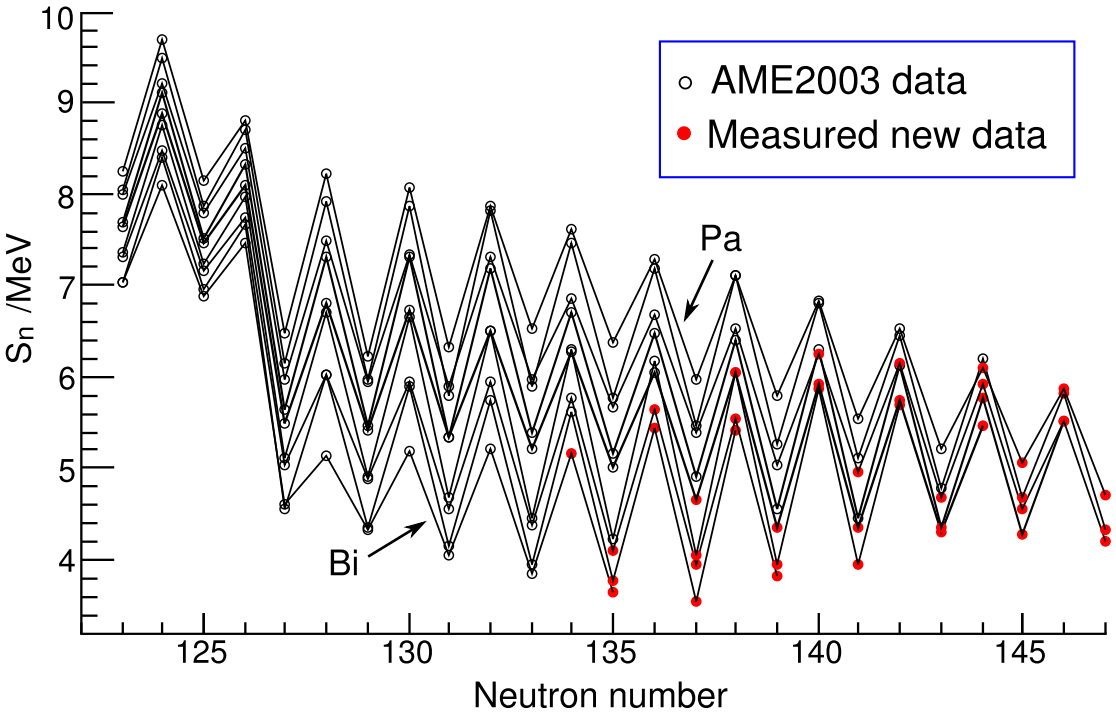

Figure 4.14: Experimental one-neutron separation energies in the element range of Bi–Pa.

There is no further obvious deviation from the smooth trends observed which means no shape changes or subshell effects are indicated after the N=126 neutron shell closure in the present data. The S_{2p} values in the range of N=134 and N=147 are also shown in Fig.4.18. The comparison of experimental S_{2n} and predicted S_{2n} values are shown in Fig.4.19.

4.6 Neutron and proton shell gaps

An interesting question concerning the magic numbers is if they still exist far from the stability line. The indication of the influence of magic numbers can be obtained by the so-called shell gaps. The neutron and proton shell gaps are defined as:

$$\Delta_n(N_0,Z) = S_{2n}(N_0,Z) - S_{2n}(N_0+2,Z), \tag{4.5}$$

$$\Delta_p(N,Z_0) = S_{2p}(N,Z_0) - S_{2p}(N,Z_0+2), \tag{4.6}$$

where S_{2n} and S_{2p} are the two-neutron and two-proton separation energies, respectively. The experimental neutron shell gap around N=126 is plotted in Fig.4.20. The weakening of shell gaps are obvious. The experimental proton shell gap around Z=82 is plotted in Fig.4.21.

4.7 Experimental pairing energies

The nuclei with odd numbers of neutrons or protons are systematically heavier than nuclei with even numbers of neutrons and protons which manifests the existence of

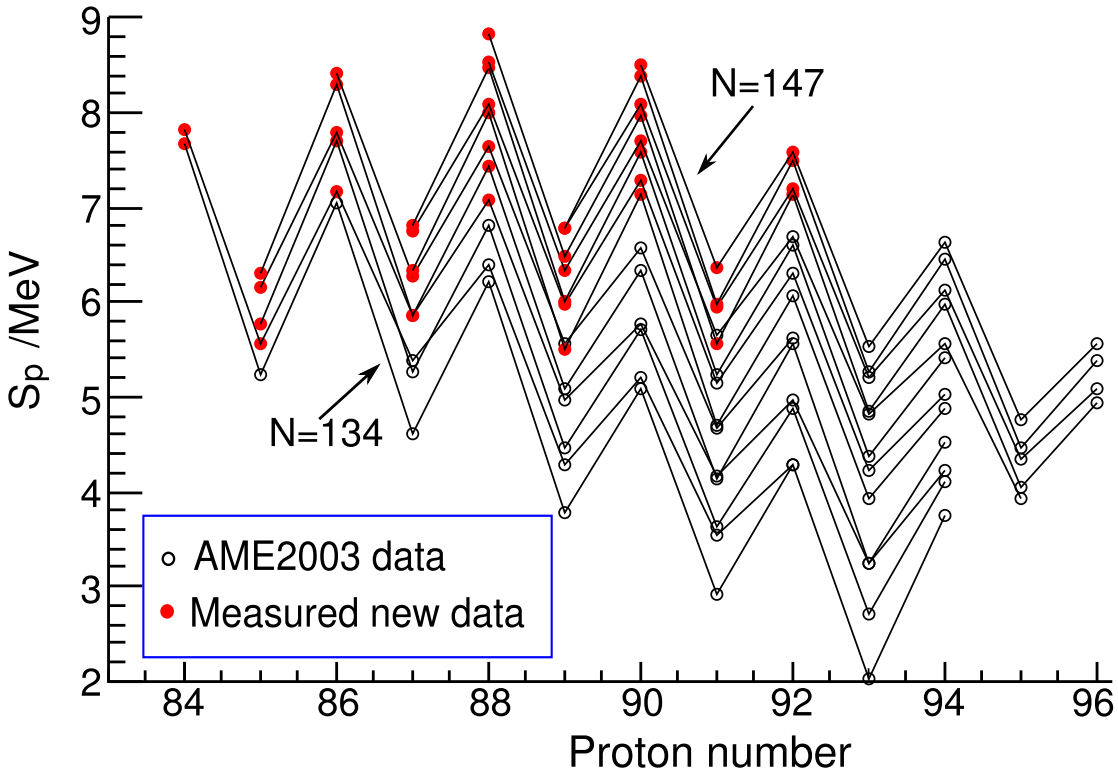

Figure 4.15: Experimental one-proton separation energies in the range of $134 \leq N \leq 147$.

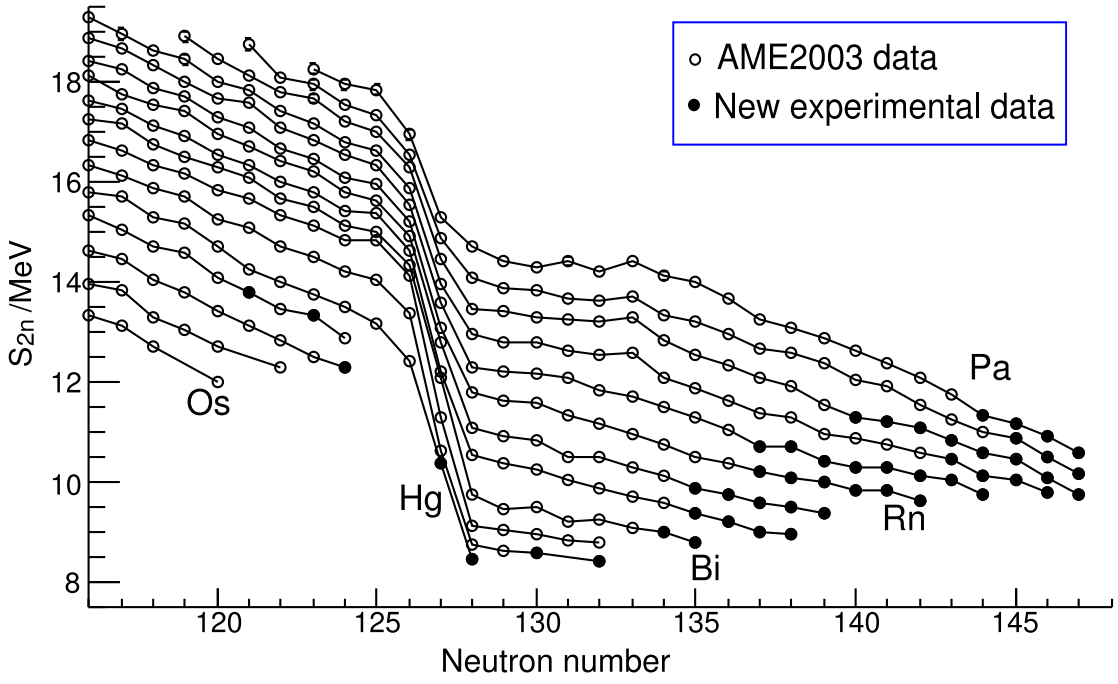

Figure 4.16: Experimental two-neutron separation energies in the element range of Os–Pa.

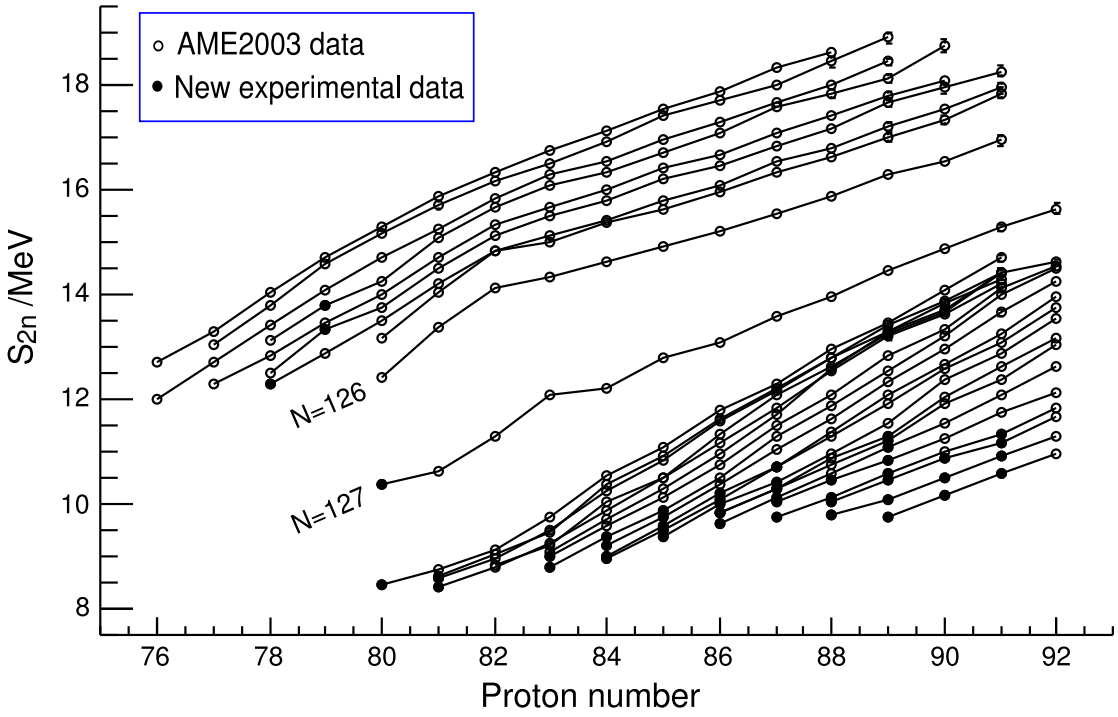

Figure 4.17: Determined experimental two-neutron separation energies as a function of proton number in the element range of Os–Pa.

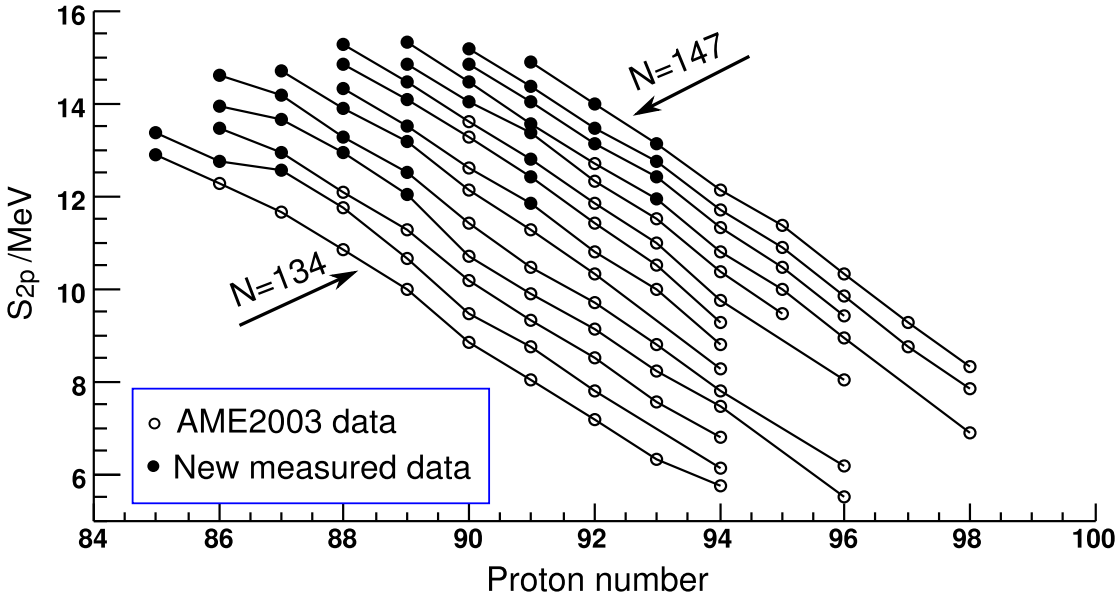

Figure 4.18: Experimental two-proton separation energies determined in the range of $134 \leq N \leq 147$.

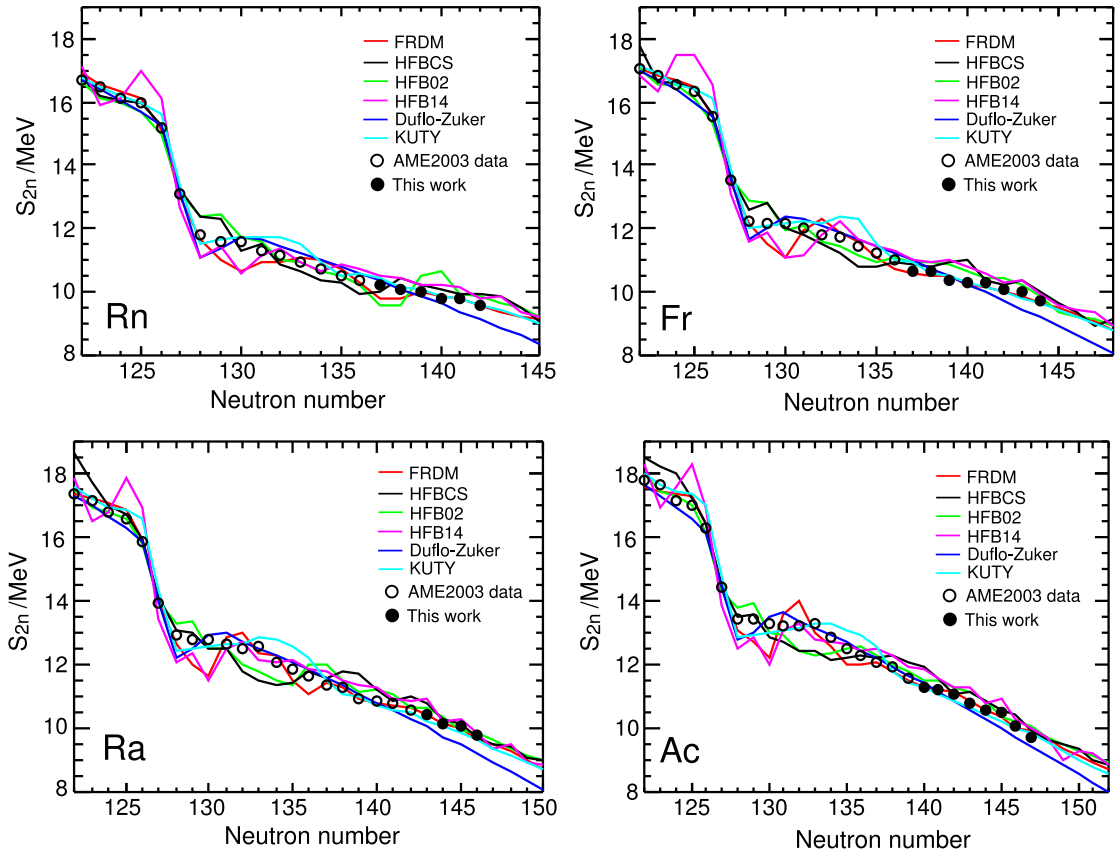

Figure 4.19: Comparison of experimental two-neutron separation energies with model predictions for Rn, Fr, Ra and Ac isotope chains.

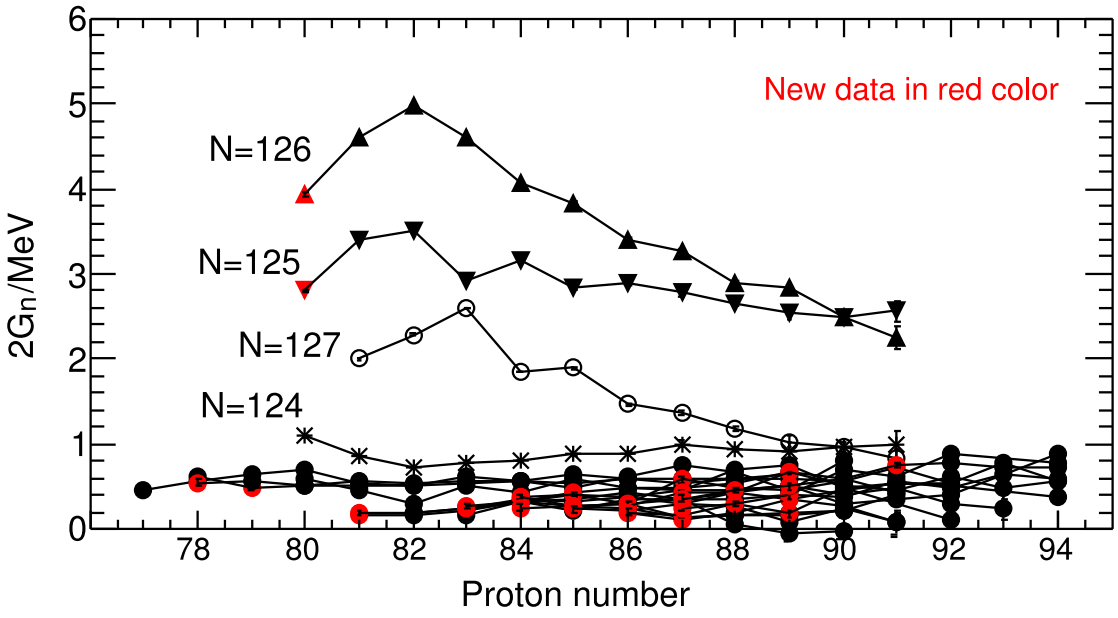

Figure 4.20: Experimental neutron shell gaps in the range of $120 \leq N \leq 142$ as a function of the proton number.

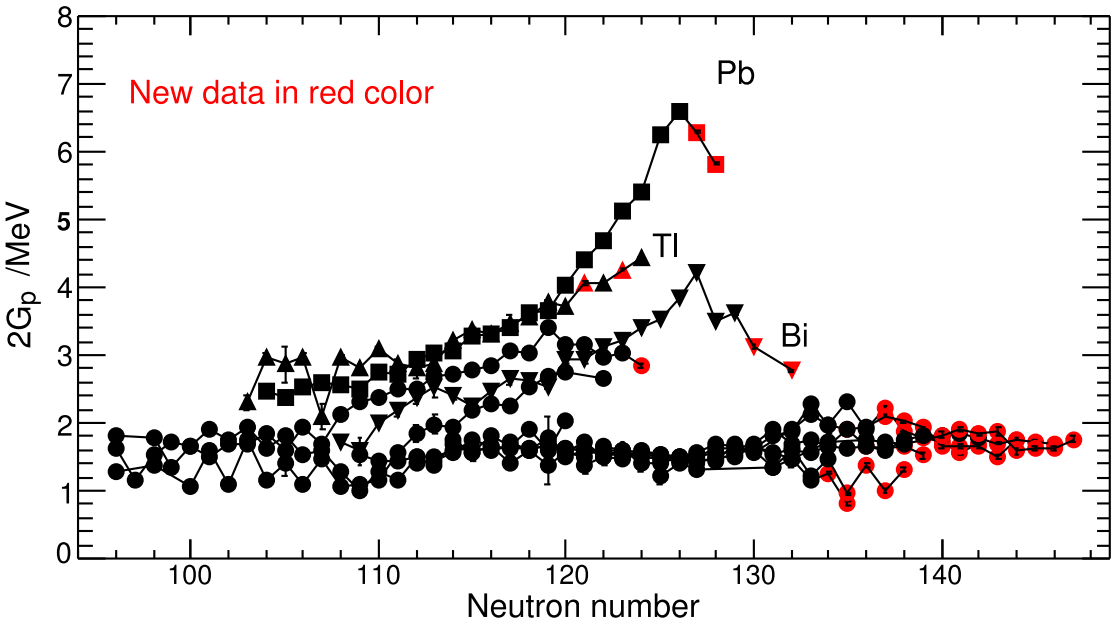

Figure 4.21: Experimental proton shell gaps in the range of $78 \leq Z \leq 91$ as a function of the neutron number.

neutron(proton) pairing gaps $\Delta_n(\Delta_p)$. The value of Δ_n and Δ_p for a specific nucleus depends on both the residual pairing interaction and the distribution of single-particle levels. Though Δ_n is slightly smaller than Δ_p for heavy nuclei a simple approximation was widely used to represent the dependence of average pairing gap on the mass number:

$$\overline{\Delta}_n = \overline{\Delta}_p = 12MeV/A^{1/2}. \tag{4.7}$$

However, equation 4.7 is limited to nuclei near the valley of the β-stability line. A dependence of the pairing gap on the relative neutron excess was introduced[70]:

$$\overline{\Delta}_n = \overline{\Delta}_p = 7.2 - 44 \cdot \left(\frac{N-Z}{A}\right)^2 MeV/A^{1/3}. \tag{4.8}$$

For odd-odd nuclei there is an additional energy δ which represent the attractive residual interaction between unpaired neutrons and unpaired protons. The average residual neutron-proton interaction energy $\overline{\delta}$ was found to be inversely proportional to the mass number and can be approximately written as:

$$\overline{\delta} = 20MeV/A. \tag{4.9}$$

The experimental values of Δ_n, Δ_p and δ can be derived directly from experimental masses. In reference [71] the following formulas were introduced to calculate the experimental values of Δ_n, Δ_p and δ using fourth-order finite-difference equations:

$$\Delta_n^{even-even} = -\frac{1}{8}[m(Z,N+2) - 4m(Z,N+1) + 6m(Z,N) - 4m(Z,N-1) + m(Z,N-2)], \tag{4.10}$$

$$\Delta_n^{odd-neutron} = \frac{1}{8}[m(Z,N+2) - 4m(Z,N+1) + 6m(Z,N) - 4m(Z,N-1) + m(Z,N-2)], \tag{4.11}$$

$$\Delta_p^{odd-even} = -\frac{1}{8}[m(Z+2,N) - 4m(Z+1,N) + 6m(Z,N) - 4m(Z-1,N) + m(Z-2,N)], \tag{4.12}$$

$$\Delta_p^{odd-proton} = \frac{1}{8}[m(Z+2,N) - 4m(Z+1,N) + m(Z,N) - 4m(Z-1,N) + m(Z-2,N)], \quad (4.13)$$

$$\delta^{even-even} = \frac{1}{4}\{2[m(Z,N+1) + m(Z,N-1) + m(Z-1,N) + m(Z+1,N)] - [m(Z+1,N+1), + m(Z-1,N+1) + m(Z-1,N-1) + m(Z+1,N-1)] - 4m(Z,N)\} \quad (4.14)$$

$$\delta^{odd-neutron} = -\frac{1}{4}\{2[m(Z,N+1) + m(Z,N-1) + m(Z-1,N) + m(Z+1,N)] - [m(Z+1,N+1) + m(Z-1,N+1) + m(Z-1,N-1) + m(Z+1,N-1)] - 4m(Z,N)\}, \quad (4.15)$$

$$\delta^{odd-proton} = \delta^{odd-neutron}, \quad (4.16)$$

$$\delta^{odd-odd} = \delta^{even-even}, \quad (4.17)$$

where $m(Z,N)$ is the experimental mass of the nucleus with Z protons and N neutrons. Those equations are used to determine the values of Δ_n, Δ_p and δ independently. The following additional formulas can be used to verify the self-consistency of this method:

$$\Delta_n^{odd-proton} - \delta = -\frac{1}{8}[m(Z,N+2) - 4m(Z,N+1) + 6m(Z,N) - 4m(Z,N-1) + m(Z,N-2)], \quad (4.18)$$

$$\Delta_n^{odd-odd} - \delta = \frac{1}{8}[m(Z,N+2) - 4m(Z,N+1) + 6m(Z,N) - 4m(Z,N-1) + m(Z,N-2)], \quad (4.19)$$

$$\Delta_p^{odd-neutron} - \delta = -\frac{1}{8}[m(Z+2,N) - 4m(Z+1,N) + 6m(Z,N) - 4m(Z-1,N) + m(Z-2,N)], \quad (4.20)$$

$$\Delta_p^{odd-odd} - \delta = \frac{1}{8}[m(Z+2,N) - 4m(Z+1,N) + 6m(Z,N) - 4m(Z-1,N) + m(Z-2,N)], \quad (4.21)$$

Fig.4.22 shows the experimental residual neutron-proton interaction energies for Rn, Fr, Ra and Ac isotopes. The experimental pairing gaps for Rn, Fr, Ra and Ac isotopes are shown in Fig.4.23.

4.8 Proton-neutron interactions

The average empirical proton-neutron $(p-n)$ interaction energy, δV_{pn}, can be deduced from the double differences of masses. δV_{pn} refers to the interaction between the last proton(s) and the last neutron(s) and thus is sensitive to the microscopic energy levels of the valence protons and neutrons. δV_{pn} is important for nuclear structure studies[72, 73]. The δV_{pn} value can be directly obtained from experimental masses. For even-even nuclei, δV_{pn} can be calculated by:

$$\delta V_{pn}(Z,N) = \frac{1}{4}[\{B(Z,N) - B(Z,N-2)\} - \{B(Z-2,N) - B(Z-2,N-2)\}]. \quad (4.22)$$

The core of involved four nuclei remain nearly the same and δV_{pn} largely cancels the interactions of the last nucleons with the cores. A given δV_{pn} value for an even-even nuclei refers to the interaction of the last two protons and last two neutrons. The experimental δV_{pn} for even-even nuclei in the range from Z=74 to Z=94 is plotted in

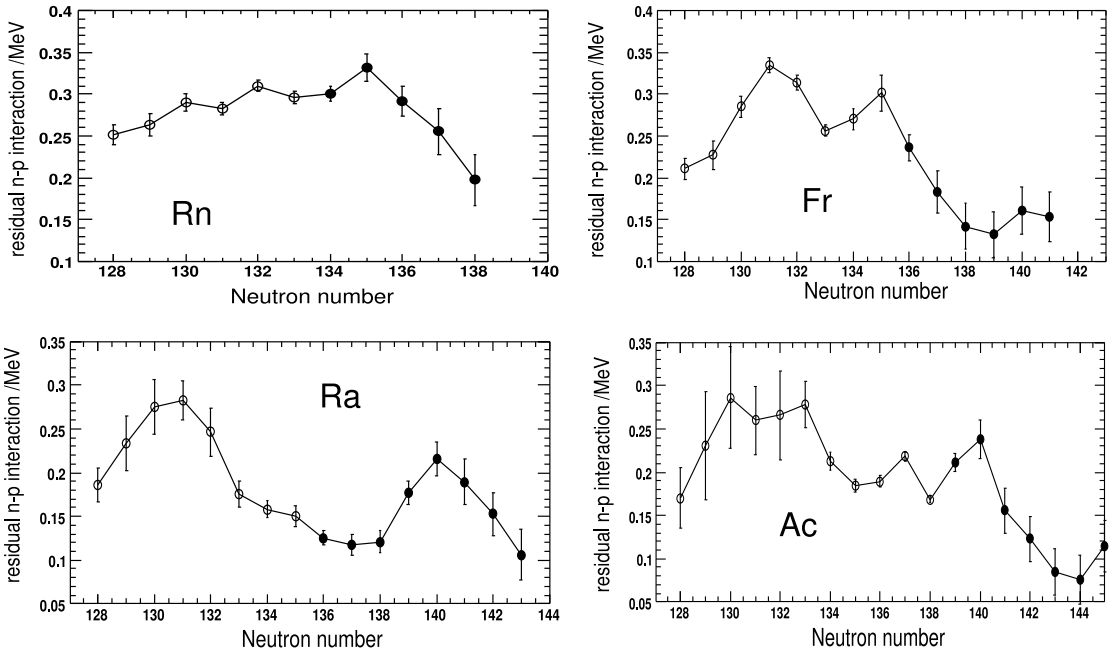

Figure 4.22: Experimental residual neutron-proton interaction energies. The data include the measured masses of this experiment presented as filled circles.

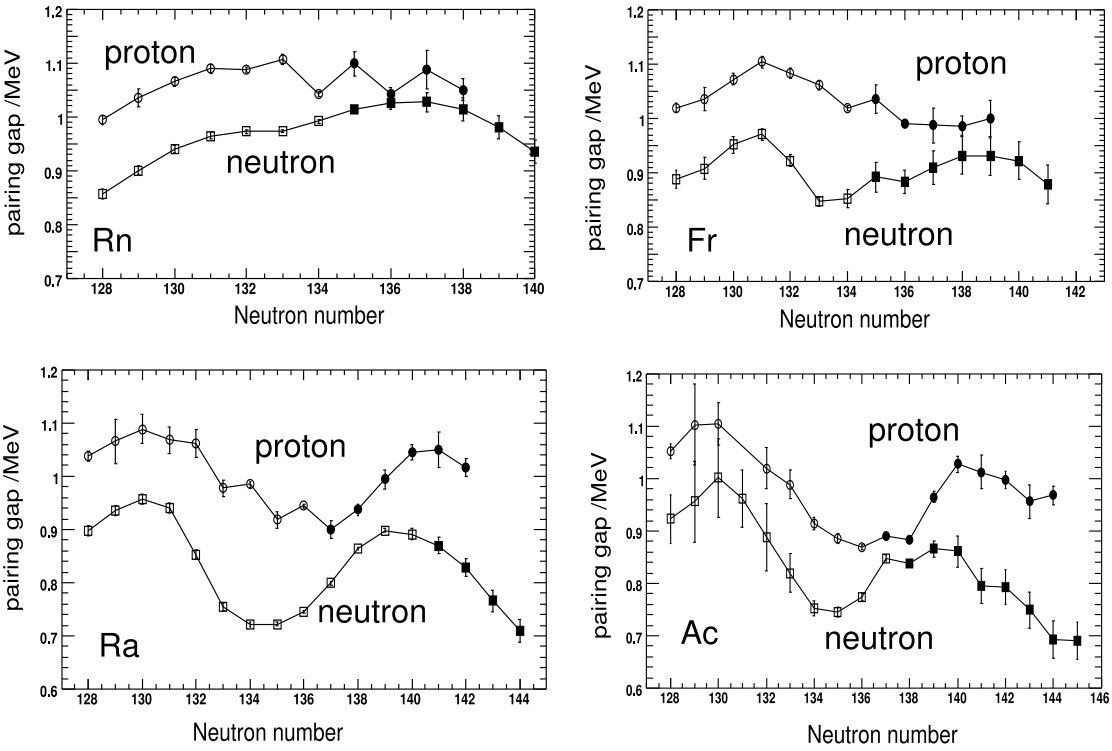

Figure 4.23: Experimental neutron and proton pairing gaps. The data include the measured masses of this experiment presented as filled circles.

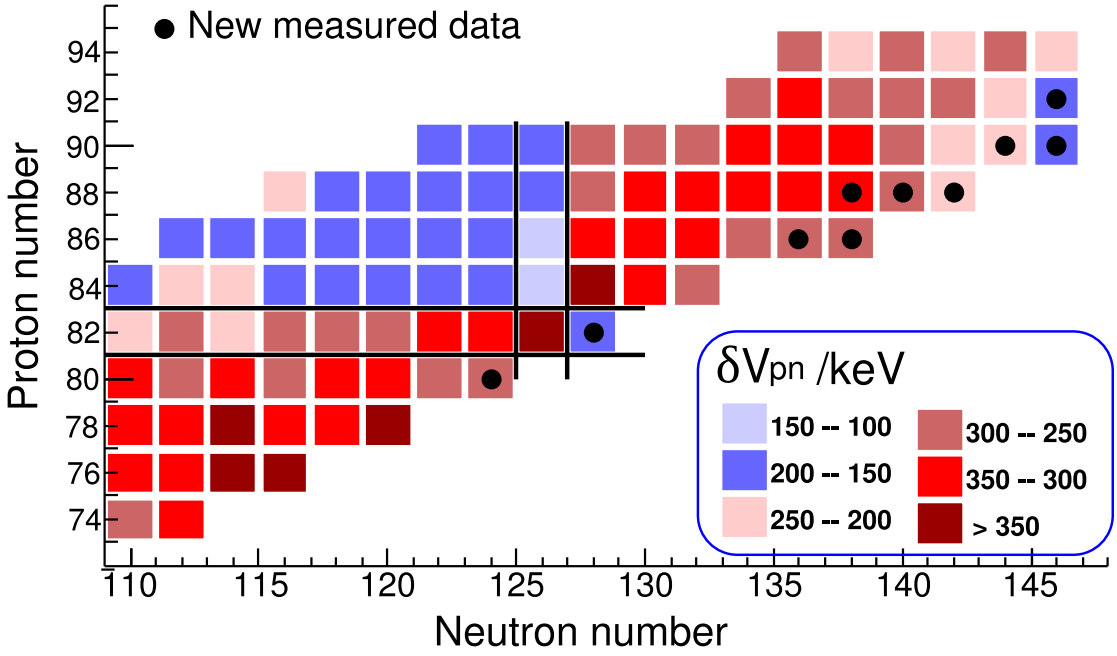

Figure 4.24: Experimental proton-neutron interactions.

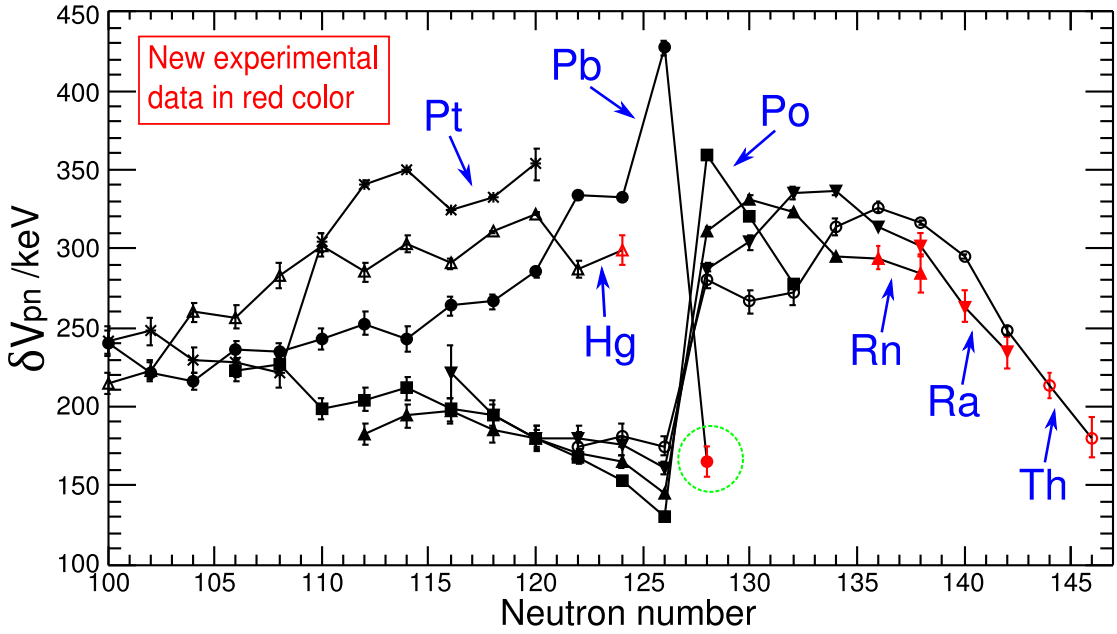

Figure 4.25: Experimental proton-neutron interactions.

Fig.4.24 with 2-dimensional presentation. In Fig.4.25 the experimental δV_{pn} values are plotted in the element range from Hg to Th.

With our new experimental mass for ^{208}Hg a δV_{pn} value for lead beyond the N=126 shell closure is available. The δV_{pn} values in Fig.4.25 before N=126 split into two groups. One is upsloping for Z$\leq$82 and one is downsloping for Z$>$82. For Z$>$82 elements, the δV_{pn} have a sharp jump at N=126 to a higher level which roughly equal to δV_{pn} value of Z$>$82 elements before N=126 shell closure. The general decreasing trend of δV_{pn} for elements Z$>$82 after N=126 shell closure is obvious with the new experimental data from this work. How the experimental δV_{pn} values change after N=126 for the Z$\leq$82 elements was not known before ^{208}Hg was measured. As shown in Fig.4.25 the δV_{pn} value for ^{210}Pb is dramatically reduced compared to the precedent isotope and matches almost the level of the lower slope.

4.9 Experimental results on nuclear half-lives

The half-life of ^{235}Ac was measured in this work for the first time. As explained in section 2.7 the half-life of stored ions can be extracted from the time-resolved Schottky noise power spectrum. Fig.4.26 shows a picture of the Schottky noise spectrum with ^{235}Ac.

The half-life of ^{234}Ac is 40$\pm$7 s according to the latest NUBASE evaluation[39] and the half-life of ^{235}Ac was unknown before. Our experimental values for the half-life of ^{234}Ac is 45$\pm$2 s and for ^{235}Ac is 62$\pm$4 s (see Fig.4.27).

The half-lives determined in this experiment are summarized in table4.5.

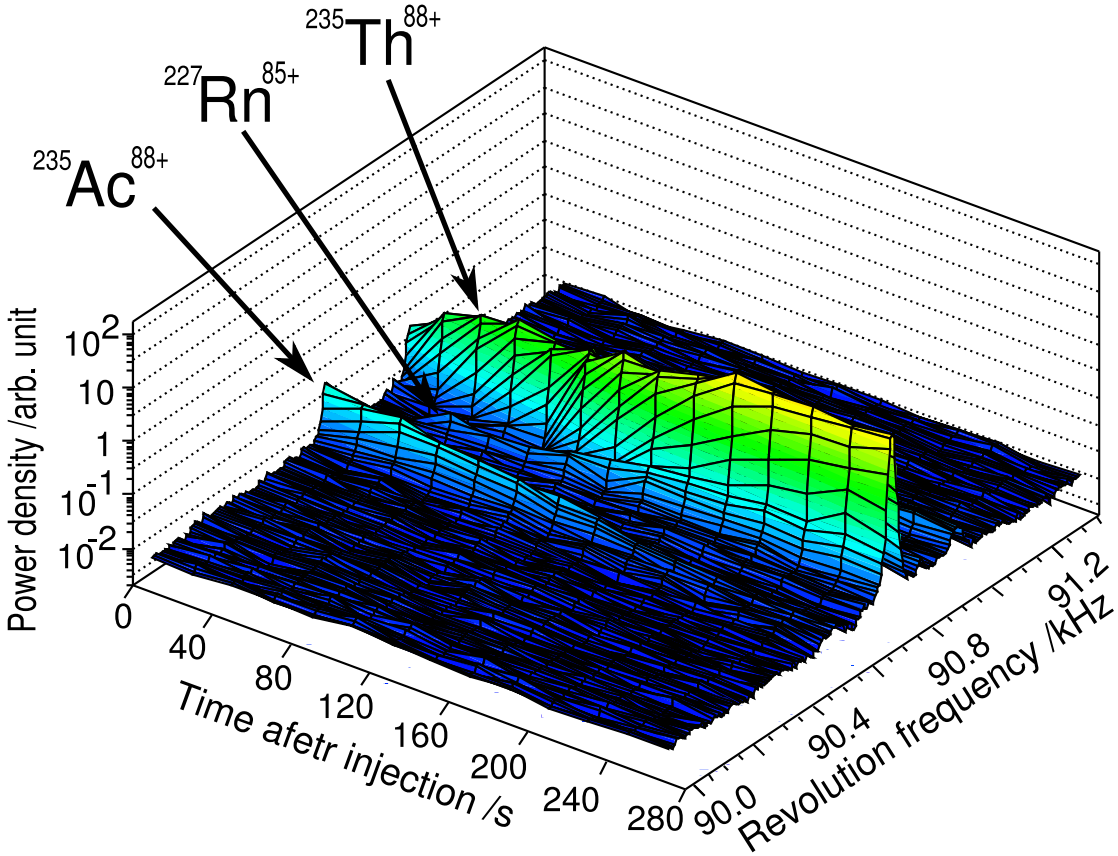

Figure 4.26: Measured Schottky noise spectrum for ^{235}Ac as a function of time. ^{227}Rn^{85+} and ^{235}Th^{88+} are mixed due to the small frequency difference (about 45 Hz).

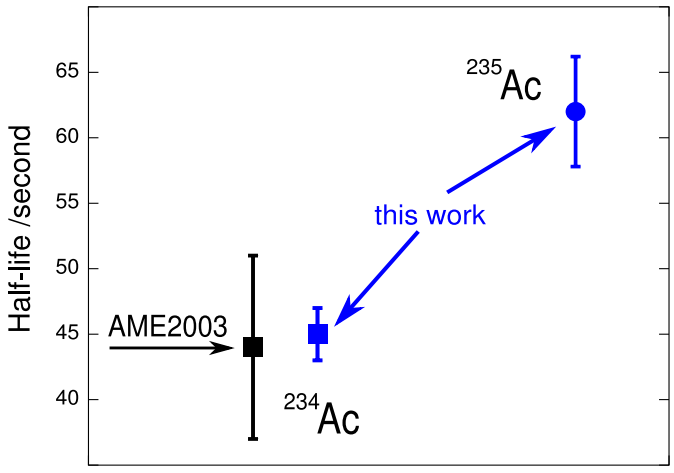

Figure 4.27: Measured half-lives of ^{234}Ac and ^{235}Ac. The value from AME2003 is given for comparison.

Table 4.3: List of measured new masses for known isotopes/isomers. M_{SMS} and δM_{SMS} are the mass excess and its uncertainty determined in this experiment using the local-mass-evaluation method. In our forthcoming publication we will present the final values of the matrix method in accordance with the previously published values from SMS. $M_{AME2003}$ and $\delta M_{AME2003}$ are mass excess and its uncertainty estimated in AME2003.

Nuclide	M_{SMS} (keV)	δM_{SMS} (keV)	$M_{AME2003}$ (keV)	$\delta M_{AME2003}$ (keV)	M_{SMS}-$M_{AME2003}$ (keV)
^{236}Th	46263	30	46450	200	-187
^{237}Th	50012	30	50200	360	-188
^{230}Ac	33839	30	33810	300	29
^{233}Ac	41324	30	41500	300	-176
^{234}Ac	44839	30	45100	400	-261
^{235}Ac	47387	30	47720	360	-333
^{231}Ra	38240	30	38400	300	-160
^{232}Ra	40537	30	40650	280	-113
^{233}Ra	44341	30	44770	470	-429
^{234}Ra	46908	31	47230	490	-322
^{228}Fr	33396	30	33280	200	116
^{230}Fr	39496	32	39600	450	-104
^{231}Fr	42095	36	42330	470	-235
^{223}Rn	20399	30	20300	300	99
^{224}Rn	22424	30	22440	300	-16
^{225}Rn	26546	30	26490	300	56
^{226}Rn	28750	30	28770	400	-20
^{227}Rn	32871	31	32980	420	-109
^{228}Rn	35263	31	35380	410	-117
^{221}At	16793	30	16810	200	-17
^{222}At	20920	30	20800	300	120
^{223}At	23448	30	23460	400	-12
^{219}Po	12669	30	12800	360	-131
^{220}Po	15295	30	15470	360	-175
^{212n}Bi	-6639	30	-5920	200	-719
^{217}Bi	8775	30	8820	200	-45
^{218}Bi	13207	32	13340	360	-133
^{211}Tl	-6078	42	-6080	200	2
^{208}Hg	-13265	31	-13100	300	-165
^{202}Pt	-22752	32	-22600	300	-152

Table 4.4: Mass values which are improved by this experiment. M_{SMS} and δM_{SMS} are the mass excess and its uncertainty from this work and $M_{AME2003}$ and $\delta M_{AME2003}$ are the mass excess and its uncertainty from AME2003.

Nuclide	M_{SMS} (keV)	δM_{SMS} (keV)	$M_{AME2003}$ (keV)	$\delta M_{AME2003}$ (keV)	M_{SMS}-$M_{AME2003}$ (keV)
^{236}Pa	45332	30	45350	200	-18
^{237}Pa	47542	30	47640	100	-98
^{238}Pa	50904	30	50770	60	134
^{235}Pa	42309	30	42330	50	-21
^{235}Th	44015	30	44260	50	-245
^{231}Ac	35773	30	35920	100	-147
^{232}Ac	39171	30	39150	100	21
^{224}Fr	21796	30	21660	50	136
^{226}Fr	27540	30	27370	100	170
^{227}Fr	29685	30	29650	100	35
^{229}Fr	35716	30	35820	40	-104
^{220}At	14370	30	14350	50	20
^{207}Hg	-16507	31	-16220	150	-287
^{202}Au	-24407	32	-24400	170	-7
^{200}Au	-27234	32	-27270	50	36
^{200m}Au	-26208	31	-26300	50	92

Isotope	Half-life evaluation method	Half-life (s)
^{234}Ac	peak area fitting	45±2
^{235}Ac	peak area fitting	62±4
^{232}Ra	peak area fitting	240±20
^{236}Ac	single-ion tracing	72^{+345}_{-33}
^{224}At	single-ion tracing	76^{+138}_{-23}
^{222}Po	single-ion tracing	145^{+694}_{-66}
^{221}Po	single-ion tracing	112^{+58}_{-28}
^{213}Tl	single-ion tracing	101^{+484}_{-46}
^{234m}Ac	single-ion tracing	> 93
^{234n}Ac	single-ion tracing	149^{+95}_{-42}
^{228m}Ac	single-ion tracing	119^{+61}_{-30}
^{228m}Fr	single-ion tracing	94^{+170}_{-29}
^{214m}Bi	single-ion tracing	> 93
^{213m}Bi	single-ion tracing	> 168

Table 4.5: Measured half-lives in this experiment.

Chapter 5

Comparison with experimental data and theoretical predictions

5.1 Comparison with previous experimental masses

A comparison of present measured mass values with previous experimental data is shown in Fig.5.1. Most of the mass values from this experiment agree well with the AME2003 data. However, four isotopes namely ^{238}Pa, ^{235}Th, ^{229}Fr, ^{224}Fr show a strong disagreement with previous data. The masses of those four isotopes are has been previously deduced by Q_β values which are prone to systematic errors in case excitation is unknown and not resolved.

5.2 Test of mass models

New developments of the theoretical models to predict the atomic mass is of great importance for nuclear structure physics and astrophysics. As shown in Fig.1.3 mass models have a large difference in their predictive power for exotic nuclides. The measured new masses for neutron-rich nuclides represent a valuable test for the models.

There are many mass models developed for the prediction of unknown masses. The mass models have normally a number of free parameters fitted to experimental data. The goal is to calculate mass values where no experimental data are available. Different theories are used to develop mass models. Here, six widely known mass models including the microscopic approach(HFBCS[12], HFB02[13], HFB14[14]), the macroscopic-microscopic approaches (FRDM[11]) and the global mass formulas (Duflo-Zuker[15] and KUTY[18]) were selected for comparison to our new data.

5.2.1 Microscopic approaches

The microscopic approach tries to reproduce the nuclear properties with self-consistent theory based on the basic nucleon-nucleon interactions. For this purpose one solves the Schrödinger equation:

$$H\Psi = E\Psi, \tag{5.1}$$

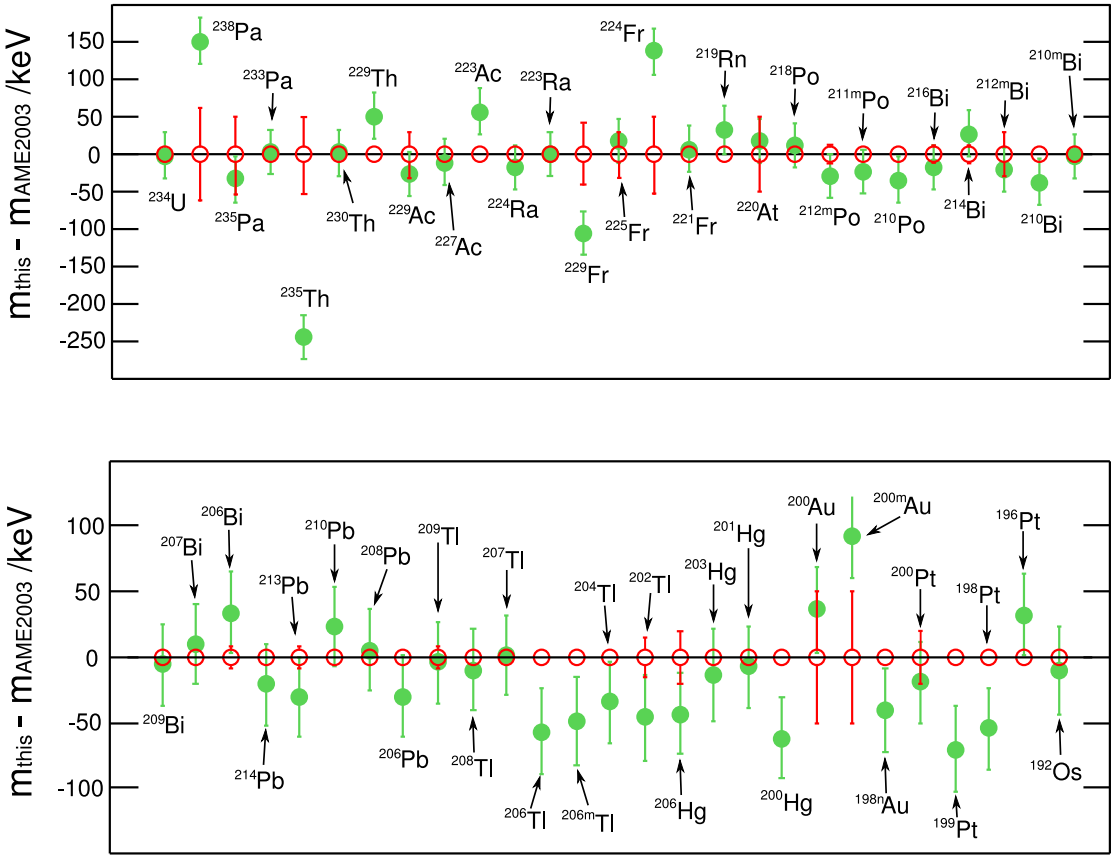

Figure 5.1: Comparison of our experimental data with the known mass values from AME2003 compilation. The error bars shown in figure are not for the difference but for each data set separately. The errorbar of some AME data are within the size of the symbols.

where

$$H = -\frac{\hbar^2}{2M}\sum_i \Delta_i^2 + \sum_{i>j} V_{ij} + \sum_{i>j>k} V_{ijk}, \tag{5.2}$$

V_{ij} and V_{ijk} represents the real two-nucleon and three-nucleon interaction potentials, respectively. This fundamental approach can be regarded as the final objective of nuclear theory but at present the solution of equation 5.1 for the nuclear many-body system is rather complicated. Only in the recent years it has become possible to calculate nuclear masses from the fundamental nucleon-nucleon interactions (ab initio calculations) with an accuracy as required for astrophysical network calculations for the light nuclides (A$\leq$16) only[74, 75, 76]. The nuclear masses for r-process applications have to be calculated with free parameters fitted to the experimental masses.

The Hartree-Fock method uses an effective force to represent the nucleon-nucleon interaction and free parameters fitted to the experimental masses. A widely used effective force is the 10-parameter Skyrme force. Using such effective forces not only the masses but also some other quantities like spin, parity and individual energy levels can be derived.

A complete mass table from non-relativistic Hartree-Fock method using the 10-parameters Skyrme force was first published in 2001 – the HFBCS-1 mass table[77]. Two new formulas, HFB-1[78] and HFB-2[79], were developed in 2002 with improved predictive power. The pairing in HFBCS-1 was treated in the BCS approximation. The Hartree-Fock-Bogoliubov method was used in HFB-1, HFB-2 and the following versions. Both HFBCS-1 and HFB-1 were fitted to the experimental data in AME95[80] and the parameters of HFB-2 formula were fitted to more experimental data (preliminary version of AME2003 in 2001) and the parameters in HFB-2 were optimized on the base of HFB-1. HFBCS-1, HFB-2 and the latest version HFB-14[14] mass formula are used for comparison with our new experimental masses.

5.2.2 Macroscopic-microscopic approaches

Macroscopic-microscopic nuclear models describe nuclear properties as a function of macro quantities (neutron number N, proton number Z and nuclear shape) and microscopic corrections. The macroscopic-microscopic methods have the advantage that much less computing time is required. To calculate the total nuclear binding energy as a sum of macroscopic terms and microscopic terms:

$$E_{total}(Z,N,shape) = E_{macro} + E_{micro}, \tag{5.3}$$

where the E_{macro} is a smooth function of Z and N. E_{macro} contains the macroscopic effects like volume energy, surface energy, Coulomb energy, etc.. The E_{micro} contains the microscopic corrections from the proton and neutron shell effects and pairing energy. The shell corrections are made by calculating the non-uniform distribution of the single-particle levels in nuclei. The pairing energy results from the short-range attractive force between nucleons. The introduced parameters in the model are determined by least-square adjustment to the experimental ground masses.

The finite-range droplet model (FRDM)[11] is the most sophisticated model among the macroscopic-microscopic approaches. There are in total 31 parameters in the FRDM model but only 19 of them were determined by mass fitting and 12 parameters were predetermined by other measurements like scattering data. The final parameters of FRDM were determined by a fit to 1654 masses with N and Z$\geq$8 from AME95[80].

5.2.3 The Duflo-Zuker and KUTY mass formulas

Besides the microscopic and macroscopic-microscopic approaches there are some global mass formulas which can also provided mas values in the unknown mass region. The Duflo-Zuker mass formula also starts with an effective interaction. The Duflo-Zuker mass formula[15] has 28 parameters and all are determined by a fit to experimental masses. A rms error of 346 keV was achieved by fitting to 1768 experimental masses in AME95.

The main feature of the KTUY mass formula is to calculate the microscopic effects including nuclear deformations. The KTUY mass formula has 34 parameters determined directly by a fit to the experimental masses in [80] and the rms deviation to known masses is 0.678 MeV[81].

5.2.4 Comparison of experimental and theoretical data

The determined new experimental masses from this work in the element range of Bi–Th were compared with the above mass formulas and the results are shown in Fig.5.3. The systematical trends of the model prediction can be clearly seen in Fig.5.3.

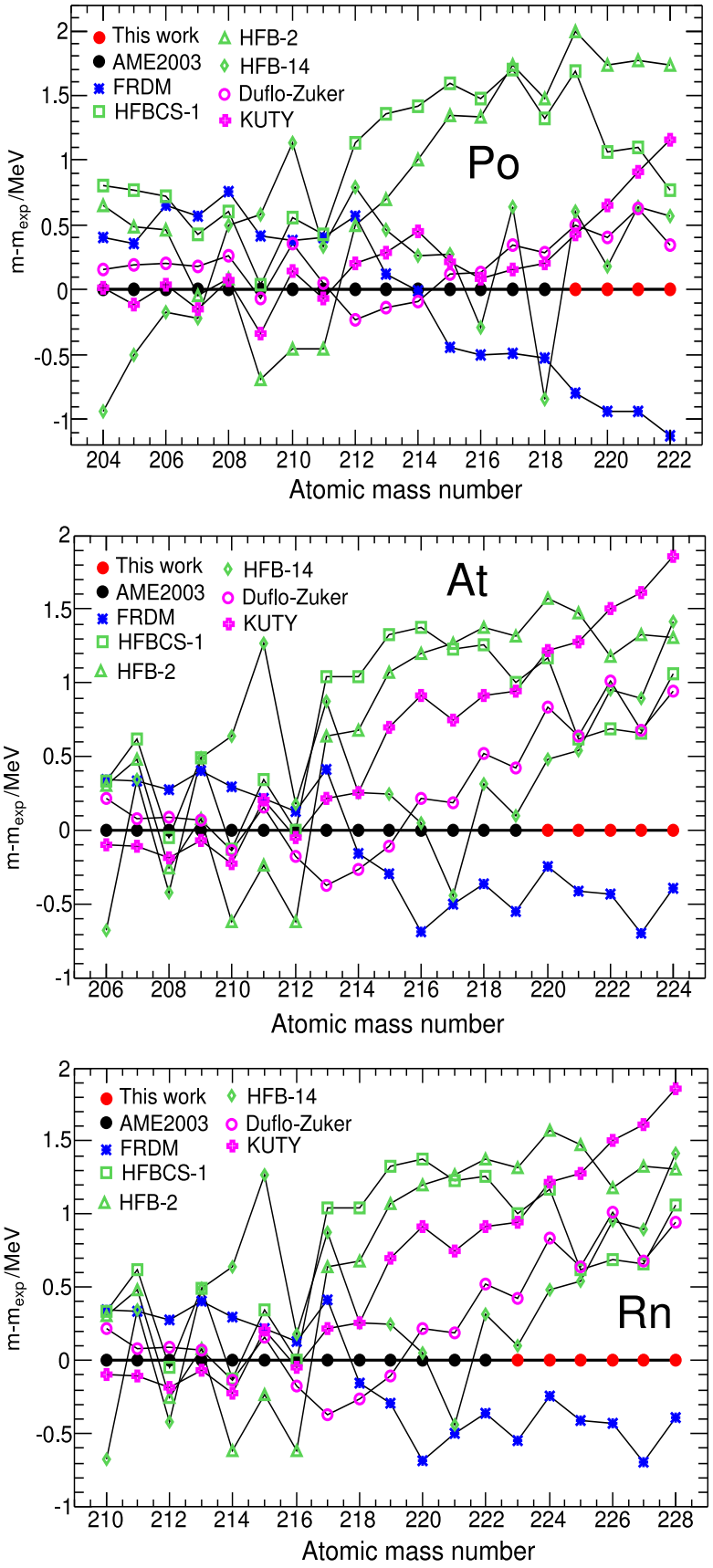

Figure 5.2: Comparison of our experimental data with mass model predictions for Po, At and Rn isotopes.

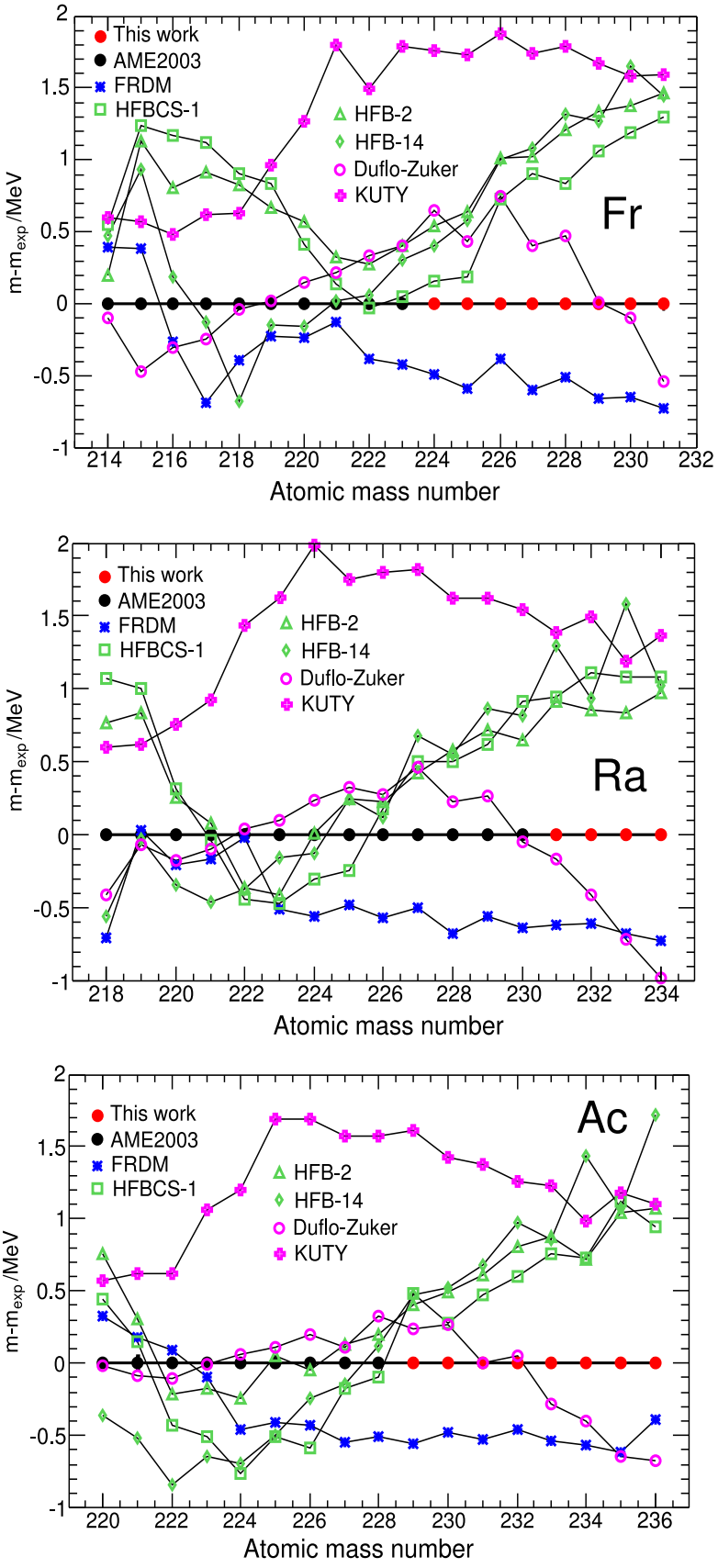

Figure 5.3: Comparison of our experimental data with the mass model predictions for Fr, Ra and Ac isotopes.

Chapter 6

Outlook

6.1 What are the most interesting unknown mass regions?

The number of nuclides predicted are more than 5000. The mass has been measured only for less than two thousand nuclides. Of course the mapping of the large unknown mass region is always interesting to discover new nuclear structure physics.

The most interesting region for further atomic mass measurements are:

- Masses near and at the drip-lines. The positions of drip-lines can be directly determined from the experimental masses. The proton drip-line is reached for most of elements, however the neutron drip-line is experimentally confirmed up to Z=8. New opportunities will be opened up in this field with the next-generation facilities in different countries, FAIR[82] in Germany, RIA/FRIB[83] in USA, HIRFL-CSR[84] in China, RIB Factory[85] in Japan, for example.
- Masses of N$\simeq$Z nuclei. Here, the role of the neutron-proton interaction can be studied and also the CVC hypothesis can be verified for the $0^+ \rightarrow 0^+$ decay[86] with those nuclei.
- In the region of shell closures especially around the doubly magic nuclides ^{48}Ni, ^{78}Ni, ^{100}Sn and ^{132}Sn. Shell quenching and new shell effects can be observed far from stability with new experiment data.
- Close and at the nucleosynthesis paths. Of particular interest are the pathways of nucleosynthesis in stars called rp- and r-process.

6.2 New facilities and techniques for mass measurements

The production and study of exotic nuclei with short half-lives and small production cross sections are a great challenge. For example, the very neutron-rich nuclei have tiny production cross sections as shown in Fig.6.1 for uranium projectile fragmentation. In this calculation the N=126 and Z=82 nuclides are considered.

The isotopes with production cross sections below 10^{-5}mb represents the limits of the present FRS-ESR facility.

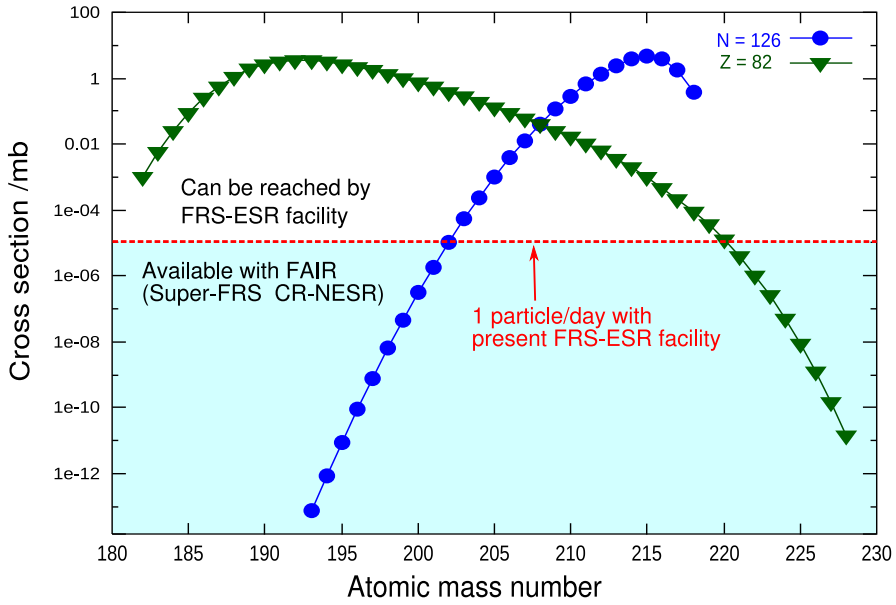

Figure 6.1: Production cross section of nuclides with N=126 and nuclides with Z=82 are calculated[87] for ^{238}U projectile fragmentation. Horizontal line indicates the limits of the present FRS-ESR facility assuming that one exotic species is recorded per day.

The planned project FAIR – Facility for Antiproton and Ion Research at GSI will be the next generation international facility in Europe with high discovery potential for new mass and lifetime measurements of very exotic nuclei. The primary beam intensities of the new double synchrotron SIS100/SIS300 will exceed by a factor of up to 1000 the present primary beam intensities. Combined with the new in-flight separator Super-FRS very exotic nuclei can be measured with the new storage ring complex, CR and NESR at FAIR. The layout of Super-FRS is shown in Fig.6.2. The transmission efficiency of Super-FRS is dramatically improved compared to the present in-flight separator FRS. The comparison of the transmission efficiencies of Super-FRS and FRS are shown in Fig.6.2.

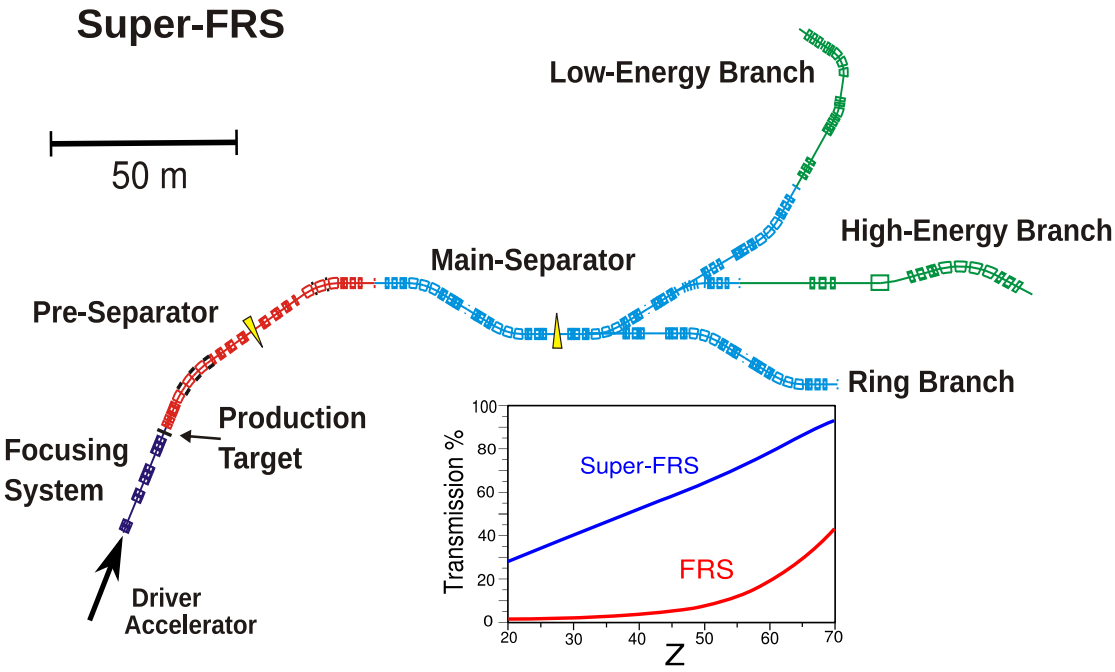

Figure 6.2: The layout of Super-FRS[88, 89] with its three experimental branches. Comparison of the transmission efficieny of Super-FRS and FRS for uranium fission fragments is shown by the insert. The transmission is calculated with 1000 MeV/u uranium projectiles for the FRS and 1500 MeV/u for the Super-FRS.

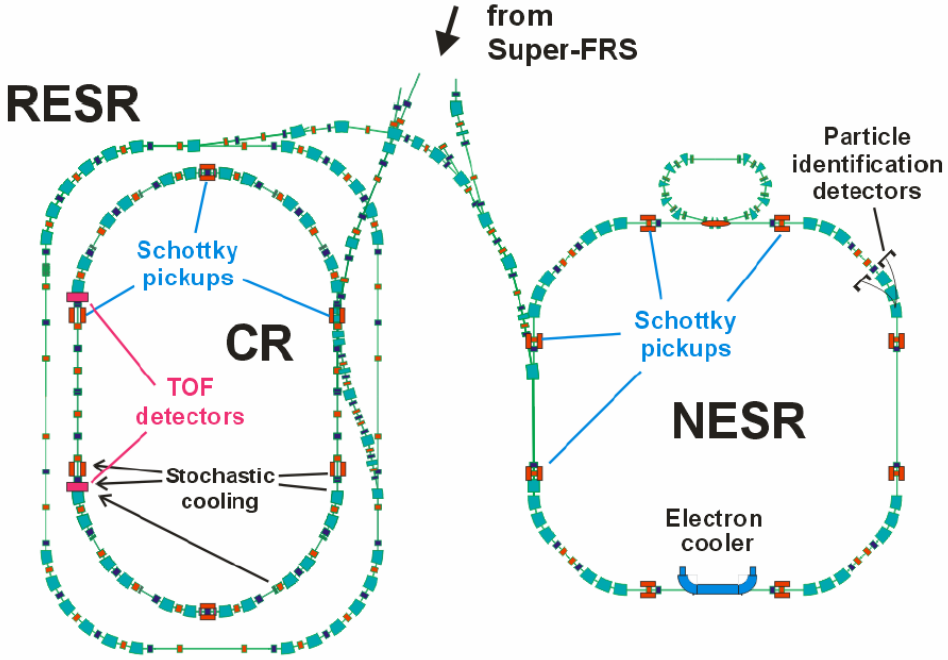

Figure 6.3: Layout of the new facilities for direct mass and half-life measurements in the FAIR project (ILIMA[90]). Exotic nuclei from the new in-flight separator Super-FRS will be injected into the Collector Ring (CR). Mass and half-life measurements of very short-lived nuclides (down to few tens μs) will be performed in the CR operated in isochronous mode. Longer-lived nuclides (longer than 1 s) will be stochastically pre-cooled in the CR and will be transferred via the RESR to the NESR. Here, they will be further cooled by electron cooling and Schottky Mass Spectrometry will be applied. Movable particle-identification detectors for independent half-life measurements will be installed behind one of the dipole magnets in the CR and the NESR.

Bibliography

[1] G. C. Rodrigues, P. Indelicato, J. P. Santos, P. Patte and F. Parente, *Systematic calculation of total atomic energies of ground state configurations*, Atomic Data Nucl. Data Tables 86 (2004) 117.

[2] D. Lunney, J.M. Pearson and C. Thibault, *Recent trends in the determination of nuclear masses*, Rev. Mod. Phys. 75 (2003) 1021.

[3] M. G. Mayer, *On closed shells in nuclei*, Phys. Rev. 74 (1948) 235
M. G. Mayer, *On closed shells in nuclei. II*, Phys. Rev. 75 (1949) 1969.

[4] C. Scheidenberger, *The contribution of precision mass measurements to nuclear physics*, Nucl. Phys. A 751 (2005) 209c-225c.

[5] J. C. Hardy, *CVC tests and CKM unitarity*, Nucl. Phys. A 752 (2005) 101.

[6] H. Schatz, A. Aprahamian, J. Görres, et al., *rp-process nucleosysthesis at extreme temperature and density conditions*, Phys. Rep. 294 (1998) 167.

[7] F. Bosch, *Measurement of mass and beta-lifetime of stored exotic nuclei*, The Euroschool lectures on physics with exotic beams, Vol.I (2004) 137.

[8] M. Jung, F. Bosch, K. Beckert, et al., *First observation of bound-state β^- decay*, Phys. Rev Lett. 69 (1992) 2164.

[9] F. Bosch, T. Faestermann, J. Friese, et al., *Observation of bound-state β^- decay of fully ionized ^{187}Re-^{187}Os cosmochronometry*, Phys. Rev Lett. 77 (1996) 5190.

[10] A. H. Wapstra, G. Audi and C. Thibault, *The AME2003 atomic mass evaluation*, Nucl. Phy. A 729 (2003) 129-676.

[11] P. Möller, J. R. Nix, W. D. Myers and W. J. Swiatecki, *Nuclear Ground-State Masses and Deformations*, Atomic Data Nucl. Data Tables 59 (1995) 185.

[12] S. Goriely, F. Tondeur and J. M. Pearson, *A Hartree-Fock nuclear mass table*, Atomic Data Nucl. Data Tables Vol. 77, Issue 2, (2001) 311-381.

[13] S. Goriely1, M. Samyn1, P.-H. Heenen2, J. M. Pearson3, and F. Tondeur4, *Hartree-Fock mass formulas and extrapolation to new mass data*, Phys. Rev. C 66 (2002) 024326.

[14] S. Goriely, M. Samyn and J. M. Pearson, *Further explorations of Skyrme-Hartree-Fock-Bogoliubov mass formulas. VII. Simultaneous fits to masses and fission barriers*, Phys. Rev. C 75 (2007) 064312.

[15] J. Duflo and A.P. Zuker, *Microscopic mass formulas*, Phys. Rev. C 52 (1995) R23.

[16] E. Comay, I. Kelson, A. Zidon, *Mass Predictions by Modified Ensemble Averaging*, Atomic Data Nucl. Data Tables, Vol. 39, p.235.

[17] J. Jänecke and P. J. Masson, *Mass Predictions from the Garvey-Kelson Mass Relations*, Atomic Data Nucl. Data Tables, Vol. 39 (1988) 265.

[18] H. Koura, T. Tachibana, M. Uno and M. Yamada, *Nuclidic Mass Formula on a Spherical Basis with an Improved Even-Odd Term*, Prog. Theo. Phys. 113 No. 2 (2005) 305.

[19] W. D. Myers and W. J. Swiatecki, *Nuclear properties according to the Thomas-Fermi model*, Nucl. Phys. A 601 (1996) 141.

[20] P. Möller and J. R. Nix, *Nuclear Masses from a Unified Macroscopic-Microscopic Model*, Atomic Data Nucl. Data Tables, 39 (1988) 213.

[21] L. Spanier and S. A. E. Johansson, *A Modified Bethe-Weizsacker Mass Formula with Deformation and Shell Corrections and Few Free Parameters*, Atomic Data Nucl. Data Tables, 39 (1988) 259.

[22] T. Tachibana, M. Uno, M. Yamada, S. Yamada, *Empirical Mass Formula with Proton-Neutron Interaction*, Atomic Data Nucl. Data Tables, 39 (1988) 251.

[23] P. Moller, W. D. Myers, W. J. Swiatecki, J. Treiner, *Nuclear Mass Formula with a Finite-Range Droplet Model and a Folded-Yukawa Single-Particle Potential*, Atomic Data Nucl. Data Tables 39 (1988) 225.

[24] Yu. E. Penionzhkevich, *Mass Measurements in Nuclear Reactions*, Hyper. Inter. 132 (2001) 265.

[25] G. Bollen, *Modern approaches for direct mass measurements far from stability*, Nucl. Phys. A 626 (1997) 297c.

[26] K. Blaum, *High-accuracy mass spectrometry with stored ions*, Phys. Rep. 425 (2006) 1

[27] M. Froese, C. Champagne, J. R. Crespo Lopez-Urrutia, et al., *A high-current electron beam trap as an on-line charge breeder for the high precision mass measurement TITAN experiment*, Hyper. Inte. 173 (2006) 85.

[28] J. W. McDonald, R. W. Bauer and D. H. Schneider, *Extraction of highly charged ions (up to 90+) from a high-energy electron-beam ion trap*, Rev. Sci. Ins. 73 (2002) 663.

[29] K. Blaum, D. Beck, G. Bollen, et al., *Pushing the relative mass accuracy limit of ISOLTRAP on exotic nuclei below 10 ppb*, Nucl. Inst. Meth. B 204, (2003) 478

[30] K. Blaum, G. Audi, D. Beck, et al., *ISOLTRAP mass measurements of exotic nuclides at* $dm/m = 10^{-8}$, Nucl. Phys. A 752 (2005) 317c

[31] R. Ringle, G. Bollen, P. Schury, S. Schwarz and T. Sun, *Octupolar excitation of ion motion in a Penning trap – A study performed at LEBIT*, International Journal of Mass Spectrometry 262 (2007) 33.

[32] S. Eliseev, M. Block, A. Chaudhuri, et al., *Octupolar excitation of ions stored in a penning trap mass spectrometry – A study performed at SHIPTRAP*, Inte. J. of Mass Spectrometry 262 (2007) 45.

[33] R. Ferrer, K. Blaum, M. Block, et al., *Development of a Fourier-Transform Ion-Cyclotron-Resonance detection for short-lived radionuclides at SHIPTRAP*, Eur. Phys. J. Special Topics 150 (2007) 347.

[34] H. Geissel, P. Armbruster, K. H. Behr, et al., *The GSI projectile fragment separator (FRS): a versatile magnetic system for relativistic heavy ions*, Nucl. Instr. and Meth. B70 (1992) 286.

[35] B. Franzke, *The Heavy ion storage and cooler ring project ESR at GSI*, Nucl. Instr. and Meth. B24-25 (1987) 18.

[36] B. Schlitt, K. Beckert, F. Bosch, et al., *Schottky mass spectrometry at the ESR: a novel tool for precise direct mass measurements of exotic nuclei*, Nucl. Phys. A 626 (1997) 315c.

[37] M. Hausmann, F. Attallah, K. Beckert, et al., *First isochronous mass spectrometry at the experimental storage ring ESR*, Nucl. Inst. Meth. A 446 (2000) 569.

[38] J. W. XIA, W. L. ZHAN, B. W. WEI, et al., *The heavy ion cooler-storage-ring project (HIRFL-CSR) at Lanzhou*, Nucl. Inst. Meth. A 488 (2002) 11.

[39] G. Audi, O. Bersillon, J. Blachot and A.H. Wapstra, *The NUBASE evaluation of nuclear and decay properties*, Nucl.Phy. A 729 (2003) 3.

[40] H. Geissel, K. Beckert, F. Bosch, et al., *First storage and cooling of secondary heavy-ion beams at relativistic energies*, Phys. Rev. Lett. 68 (1992) 3412.

[41] H. Irnich, H. Geissel, F. Nolden, et al., *Half-life measurements of bare, mass-resolved isomers in a storage-cooler ring*, Phys. Rev. Lett. 75 (1995) 4182.

[42] H. Geissel, et al., AIP Conference Proceedings Vol 831 (2006) 108, New York, Edts. S. Harissopulos, P. Demetriou, R. Julin

[43] Ch. Engelmann, F. Ameil, P. Armbruster, et al., *Production and identification of heavy Ni isotopes: evidence for the doubly magic nucleus* ^{78}Ni, Z. Physik A 352 (1995) 351.

[44] M. Bernasa, C. Engelmannb, P. Armbruster, et al., *Discovery and cross-section measurement of 58 new fission products in projectile-fission of 750·A MeV* ^{238}U, Phys. Lett. B 415 (1997) 111.

[45] J. Hüfner, *Heavy fragments produced in proton-nucleus and nucleus-nucleus collisions at relativistic energies*, Phys. Rep. 125 (1985) 129.

[46] J. Benlliure, K. -H. Schmidt, D. Cortina-Gil, et al., *Production of neutron-rich isotopes by cold fragmentation in the reaction ^{197}Au + Be at 950 A MeV*, Nucl. Phys. A 660 (1999) 87.

[47] J. -J. Gaimard and K. -H. Schmidt, *A reexamination of the Abrasion-Ablation model for the description of the nuclear fragmentation reaction*, Nucl. Phys. A 531 (1991) 709.

[48] K. Helariutta, J. Benlliure, M. V. Ricciardi and K. -H. Schmidt, *Model calculations of a two-step reaction scheme for the production of neutron-rich secondary beams*, Eur. Phys. J. A 17 (2003) 181.

[49] K. -H. Schmidt, T. Brohm, H. -G. Clerc, et al., *Distribution of Ir and Pt isotopes produced as fragments of 1A GeV ^{197}Au projectiles: a thermometer for peripheral nuclear collisions*, Phys. Lett. B 300 (1993) 313.

[50] A. J. Westphal, P. B. Price and D. P. Snowden-Ifft, *Upper limit on the cross section for nuclear charge pickup by relativstic uranium ions*, Phys. Rev. C 45 (1992) 2423.

[51] Th. Rubehn, R. Bassini, M. Begemann-Blaich, et al., *Charge pickup of ^{238}U at relativstic energies*, Phys. Rev. C 53 (1996) 993.

[52] P. Walker and G. Dracoulis, *Energy traps in a atomic nuclei*, Nature 399 (1999) 35.

[53] C. Schlegel, P. H. Regan, M. Pfützner, et al., *K-Isomers in very neutron-rich nuclei around mass 180*, Phys. Scrip. T88 (2000) 72.

[54] M. Pfützner, P. Armbruster, T. Baumann, et al., *New isotopes and isomers produced by the fragmentation of ^{238}U at 1000 MeV/nucleon*, Phys. Lett. B 444 (1998) 32.

[55] G. Münzenberg, *The separation techniques for secondary beams*, Nucl. Inst. and Meth. B 70 (1992) 265.

[56] D. J. Morrissey and B. M. Sherrill, *In-Flight separation of projectile fragments*, The Euroschool lectures on physics with exotic beams, Vol.I, (2004) 113.

[57] H. Poth, *Electron cooling: Theory, experiment, application*, Phys. Rep. 196 (1990) 135.

[58] M. Steck, P. Beller, K. Beckert, B. Franzke and F. Nolden, *Electron cooling experiments at the ESR*, Nucl. Instr. and Meth. A 532 (2004) 357,

[59] D. Boussard, *Schottky noise and beam transfer function disgnostics*, CERN Accelerator School, CERN 95-06 v2, p749.

[60] T. Radon, H. Geissel, G. Münzenberg, et al., *Schottky mass measurements of stored and cooled neutron-deficient projectile fragments in the element range of* $57 \leq Z \leq 84$, Nucl. Phys. A 677 (2000) 75.

[61] Yu. A. Litvinov, H. Geissel, Yu. N. Novikov, et al., *Precision experiments with time-resolved Schottky mass spectrometry*, Nucl. Phys. A734 (2004) 473.

[62] Yu. A. Litvinov, et al., *Mass measurement of cooled neutron-deficient bismuth projectile fragments with time-resolved Schottky mass spectrometry at the FRS-ESR facility*, Nucl. Phys. A756 (2005) 3.

[63] M. Steck, K. Beckert, H. Eickhoff, et al., *Suppression of intrabeam scattering in cooled heavy ion beams*, Hyper. Inter. 99 (1996) 245.

[64] M. Steck, K. Beckert, H. Eickhoff, et al., *Anomalous temperature reduction of electron-cooled heavy ion beams in the storage ring ESR*, Phys. Rev. Lett 77 (1996) 3803.

[65] R. W. Hasse, *Multiple Coulomb ordered strings of ions in a storage ring*, Phys. Rev. Lett. 86 (2001) 3028.

[66] K. -H. Schmidt, *Some remarks on the error analysis in the case of poor statistics*, Z. Phys. A 316 (1984) 19.

[67] M. Thoennessen, *Reaching the limits of nuclear stability*, Rep. Prog. Phys. 67 (2004) 1187.

[68] F. R. xu, P. M. Walker, J. A. Sheikh and R. Wyss, *Multi-quasiparticle potential-energy surfaces*, Phys. Lett. B 435 (1998) 257.

[69] F. R. Xu and P.M. Walker, (2008), private communications, (2008).

[70] P. Vogel, B. Jonson and P. G. Hansen, *Is there neutron-proton pairing in medium heavy nuclei?*, Phys. Lett. B 139b (1984) 4.

[71] David G. Madland and J. Rayford Nix, *New model of the average neutron and proton pairing gaps*, Nucl. Phys. A 476 (1988) 1.

[72] R. B. Cakirli, D. S. Brenner, R. F. Casten and E.A. Millman, *Proton-neutron interactions and the new atomic masses*, Phys. Rev. Lett. 94 (2005) 092501.

[73] D. S. Brenner, R. B. Cakirli and R. F. Casten, *Valence proton-neutron interactions throughout the mass surface*, Phys. Rev. C 73 (2006) 034315.

[74] Steven C. Pieper, *Quantum Monte Carlo Calculations of Light Nuclei*, Nucl. Phys. A (2005) 516.

[75] B.R. Barretta, P. Navrátilb, A. Noggac, W.E. Ormandb and J.P. Varyd, *No-core shell-model calculations in light nuclei with three-nucleon forces*, Nucl. Phys. A 746 (2004) 579.

[76] D. J. Dean and M. Hjorth-Jensen, *Coupled-cluster approach to nuclear physics*, Phys. Rev. C 69 (2004) 054320.

[77] S. Goriely, F. Tondeur and J. M. Pearson, *A Hartree-Fock nuclear mass table*, Atomic Data Nucl. Data Tables 77 (2001) 311.

[78] M. Samyn, S. Goriely, P. -H. Heenen, J. M. Pearson and F. Tondeur, *A Hartree-Fock-Bogoliubov mass formula*, Nucl. Phys. A 700 (2002) 142.

[79] S. Goriely, M. Samyn, P. -H. Heenen, J. M. Pearson and F. Tondeur, *Hartree-Fock mass formulas and extrapolation to new mass data*, Phys. Rev. C 66 (2002) 024326.

[80] G. Audi and A. H. Wapstra, *The 1995 update to the atomic mass evaluation*, Nucl. Phys. A 595 (1995) 409.

[81] H. Koura, M. Uno, T. Tachibana and M. Yamada, *Nuclear mass formula with shell energies calculated by a new methodtitle of paper*, Nucl. Phys. A 674 (2000) 47.

[82] FAIR: Facility for Antiproton and Ion Research, webpage: *www.gsi.de/fair*

[83] Webpage: *http://www.orau.org/ria*

[84] W. L. Zhan, J. W. Xia, H. W. Zhao, et al., *HIRFL today*, Nucl. Phys. A 805 (2008) 533c.

[85] H. Sakurai, *RI Beam Factory project at RIKEN*, Nucl. Phys. A 805 (2008) 526c.

[86] J. C. Hardy and I. S. Towner, *Superallowed $0^+ \rightarrow 0^+$ nuclear beta decays: A critical survey with tests of the conserved vector current hypothesis and the standard model*, Phys. Rev. C 71 (2005) 055501.

[87] K. Sümmerer and B. Blank, *Modified empirical parametrization of fragmentation cross sections*, Phys. Rev. C 61 (2000) 034607.

[88] H. Geissel, H. Weick, M. Winkler, et al., *The Super-FRS project at GSI*, Nucl. Ins. Meth. B 204 (2003) 71.

[89] M. Winkler, H. Geissel, H. Weick, et al., *The status of the Super-FRS in-flight facility at FAIR* Nucl. Ins. Meth. B, In press, (2008).

[90] ILIMA: Isomeric Beams, Lifetimes and Masses, Technical proposal: http://www.gsi.de/fair/experiments/NUSTAR/Proposals.htm

Acknowledgment

The direct support of all my colleagues and collaborators from the KPII department at GSI and the IONAS group at II. Physics Institute of the Justus-Liebig-Universität (JLU), Giessen who successfully contributed to this work is greatly acknowledged.

First of all, I would like to thank my supervisor, Prof. Dr. Hans Geissel who invited me to Germany and introduced me to his nice group. Without his scientific guidance and kind help, it would have been more difficult to complete this work. What I have learned from him will help me a lot for my scientific research in the future.

I thank Prof. Dr. Christoph Scheidenberger for his kind help not only for learning of the nuclear physics but also for my stay in Giessen. His was always ready to provide help for life and physics study.

I would like to thank Dr. Yuri A. Litvinov from GSI and Dr. Wolfgang R. Plass from JLU for their kind help and guidance. The fruitful discussions and good suggestions from them made valuable contributions to this work. Dr. Yuri A. Litvinov made a great effort to help me throughout this work.

I would like to give my special thanks to Prof. Dr. Fritz Bosch from GSI and University of Kassel. He is a very active scientist and a nice men who was always ready to help.

I would like to thank all my colleagues in the KPII department at GSI and the INOAS group at JLU Giessen, especially Dr. David Boutin, Martin Petrick, Dr. Martin Winkler, Dr. Helmut Weick and Knöbel Ronja. M. Petrick is a very friendly person and helped a lot to make my life easier in Giessen. I thank all the others in both groups who made the life enjoyable.

Finally I would like to thank my family for all the strong support a basis to complete this work. The love of the family encouraged me to carry out this work in the past years and to continue in scientific research in future.